Fermionic Quantum Systems
Part I: Phase Transitions in Quantum Dots
Part II: Nuclear Matter on a Lattice

Thesis by

Hans-Michael Müller

In Partial Fulfillment of the Requirements

for the Degree of

Doctor of Philosophy

California Institute of Technology

Pasadena, California

1999

(Submitted May 5, 1999)

Acknowledgements

First of all I would like to thank my advisor Steven Koonin for all his help and support. His advice and patience with me were the keystones to a successful endeavor. I always felt safe even when my research seemed to be lost.

Many people in Kellogg have made my stay at Caltech a wonderful time. The theory group and its many enlightening and very enjoyable meetings have helped me find a better and more detailed insight into science. I would like to thank Karlheinz Langanke for his support throughout the years. Chris Adami has proofread the thesis and suggested improvements. Ryoichi Seki and Bira van Kolck have helped with many discussions. Also, thanks to my many officemates, who have come and left, for the daily entertainment I had. I will always remember the many hilarious hours of fun and jokes with Radha P. B. and Ming Chung Chu.

Abstract

In the first part I perform Hartree-Fock calculations to show that quantum dots (i.e., two-dimensional systems of up to twenty interacting electrons in an external parabolic potential) undergo a gradual transition to a spin-polarized Wigner crystal with increasing magnetic field strength. The phase diagram and ground state energies have been determined. I tried to improve the ground state of the Wigner crystal by introducing a Jastrow ansatz for the wave function and performing a variational Monte Carlo calculation. The existence of so called magic numbers was also investigated. Finally, I also calculated the heat capacity associated with the rotational degree of freedom of deformed many-body states and suggest an experimental method to detect Wigner crystals.

The second part of the thesis investigates infinite nuclear matter on a cubic lattice. The exact thermal formalism describes nucleons with a Hamiltonian that accommodates on-site and next-neighbor parts of the central, spin-exchange and isospin-exchange interaction. Using auxiliary field Monte Carlo methods, I show that energy and basic saturation properties of nuclear matter can be reproduced. A first order phase transition from an uncorrelated Fermi gas to a clustered system is observed by computing mechanical and thermodynamical quantities such as compressibility, heat capacity, entropy and grand potential. The structure of the clusters is investigated with the help two-body correlations. I compare symmetry energy and first sound velocities with literature and find reasonable agreement. I also calculate the energy of pure neutron matter and search for a similar phase transition, but the survey is restricted by the infamous Monte Carlo sign problem. Also, a regularization scheme to extract potential parameters from scattering lengths and effective ranges is investigated.

Contents

List of Figures

List of Tables

To My Parents.

Part I

Phase Transitions in Quantum Dots

Chapter 1   Introduction

1.1   Physical Realization of a Quantum Dot

Quantum dots have been the subject of recent intense experimental and theoretical research. The interest in those nanostructures arises not only from possible new technological applications, but also from the desire to understand the fundamental physical problem of a few ($m \leq 300$) interacting electrons in an external potential and a strong magnetic field. The quantum dots are formed through a lateral confinement of a two-dimensional electron gas. The two-dimensional gas itself is realized by an inversion layer that occurs at the interface between a semiconductor and insulator or between two different semiconductors. While in the early days semiconductor-insulator systems were preferred (in form of Mosfets), which yielded an electron mobility of $\mu \sim 10^4$ cm^2/Vs, GaAs-Al$_x$Ga$_{1-x}$As interfaces are now used, with mobilities of $\mu \sim 10^7$ cm^2/Vs or better. Here, the mobility is the proportionality factor between the change of the velocity of an electron that is subject to an acceleration by an electric field in the time interval τ between two scattering processes,

$$m^* \Delta \vec{v} = e\vec{E}\tau \rightarrow \Delta v = \frac{e\tau}{m^*}\vec{E} \equiv \mu\vec{E}, \tag{1.1}$$

with m^* as effective mass. The interfaces, also called heterojunctions, can be grown with high precision and lowest impurity densities through molecular beam epitaxy. This technology uses single Gallium (Ga) atoms and Arsenic (As$_2$) molecules impinging on a heated substrate surface (usually an impure layer of GaAs) of 500ºC. While the sticking coefficient for Gallium is of order 1, Arsenic usually does not stick to the substrate, unless a Gallium atom is present. This way very pure GaAs layers can be produced, since one As atom is accompanied by one Ga atom.

Fig. 1.1 shows the energy levels for the semiconductor-semiconductor case [1].
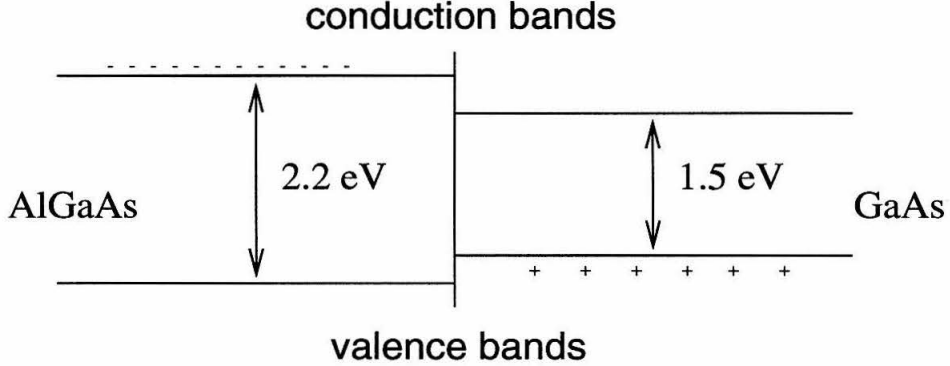
conduction bands

Figure 1.1: Band gaps for the GaAs-$Al_xGa_{1-x}As$ heterojunction. $Al_xGa_{1-x}As$ has the larger energy gap between valence and conduction and acts as insulator. It is n-doped while GaAs is weakly p-type.

$Al_xGa_{1-x}As$ has the wider band gap between valence and conduction band and acts as insulator. It is doped n-type, putting free electrons into its conduction band, while the GaAs is made as pure as possible; nevertheless it remains weakly p-type. The mobile electrons of $Al_xGa_{1-x}As$ move to the GaAs side to fill the few holes on top of its valence band, and many electrons end up in the conduction band of GaAs. The positively charged donors in the $Al_xGa_{1-x}As$ layer, which have been left behind, attract the electrons in the conduction band of the GaAs layer to the interface and bend both its bands because the separation of the charge gives rise to an electric field. This is shown schematically in Fig. 1.2. The relaxation of electrons from $Al_xGa_{1-x}As$ to GaAs continues until the Fermi levels on both sides are equal; the electric field generates a discontinuity in the potential. The density of electrons in the inversion layer is determined by the dopant density, but can be controlled by putting a backgate on the $Al_xGa_{1-x}As$ side.

The free electrons in the inversion layer move parallel to the interface in a two-dimensional sheet. This can be proven by solving the Schrödinger equation for the motion in z-direction, the direction perpendicular to the interface, which is governed by

$$H_z z_n(z) = \left(-\frac{\hbar^2}{2m_z} \partial_z^2 + V_T(z) \right) z_n(z) = \epsilon_n z_n(z). \tag{1.2}$$
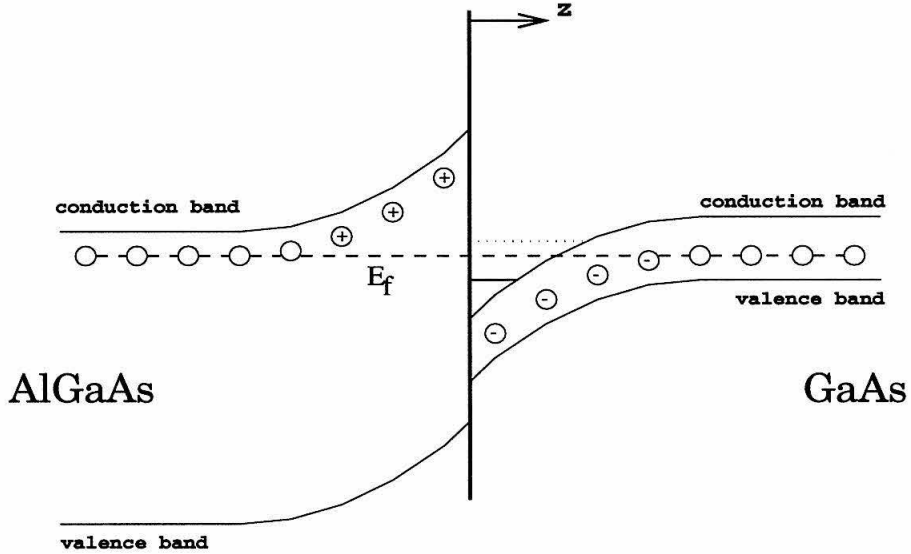
Figure 1.2: Schematic view of the bent valence and conduction band at the GaAs-$Al_xGa_{1-x}As$ junction. If the band is bent strongly enough, electrons from the valence band in GaAs move over to its conduction band and become free. The bending can be enhanced with a backgate at the $Al_xGa_{1-x}As$ layer.

A typical $V_T(z)$ is displayed in Fig. 1.3, and m_z is the effective mass of the electrons for the motion in z-direction. The energy gap between the lowest and the first excited state is with

$$\varepsilon_1 - \varepsilon_0 \approx 20 \text{ meV} \tag{1.3}$$

much higher than energies that are present when describing the motion in (x, y)-plane. The zeroth eigenstate,

$$z_0(z) \sim z \exp\left(-\frac{z}{2b}\right), \tag{1.4}$$

has a width of $b \approx 3 - 5$ nm, while the lateral confinement of the dots are of order 100 nm, or a little smaller. Thus, the picture of a two-dimensional gas holds quite well.

The confinement in (x, y)-direction is accomplished by an array of mesas etched with lithographic methods on top of the $Al_xGa_{1-x}As$. The material the array is etched from consists of SiO_2 and other materials, and the grooves form quadratic mesas as illustrated in Fig. 1.4. On top of the mesas are gates which are charged negatively,
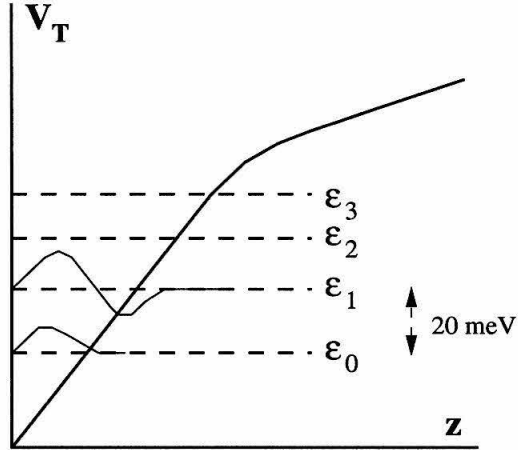
Figure 1.3: Potential V_T governing the motion of the electrons in the inversion layer in perpendicular direction. The energy gap between the lowest and the first excited state is $\varepsilon_1 - \varepsilon_0 \approx 20$ meV.

confining the electrons symmetrically in between them as shown on the right panel of Fig. 1.4. Kumar et al. [2] have performed a simulation of this device to calculate the confining potential. They self-consistently solved in Hartree-approximation the Schrödinger and Poisson equation,

$$\sum_{j=1}^{3} \frac{1}{2m_j} \left\{ \frac{\hbar}{i} \partial_j + eA_j \right\}^2 \zeta_n + [U(x,y,z) - E_n] \zeta_n = 0 \tag{1.5}$$

$$\vec{\nabla} \cdot \left[\epsilon(x,y,z) \vec{\nabla} \phi(x,y,z) \right] = -\rho(x,y,z), \tag{1.6}$$

with

$$A_i = \frac{1}{2} (B_j x_k - B_k x_j)$$

$$\vec{B} = (0, 0, B_0)$$

$$U(x,y,z) = -e\phi(x,y,z) + \Delta E_C(x,y,z) \tag{1.7}$$

on a mesh for this kind of geometry and with appropriate boundary conditions. $\Delta E_C(x,y,z)$ is the offset of the conduction band, and $\rho(x,y,z) = \rho_{out}(x,y,z) + \rho_{qd}(x,y,z)$ is the total charge density outside and inside the Schrödinger domain,
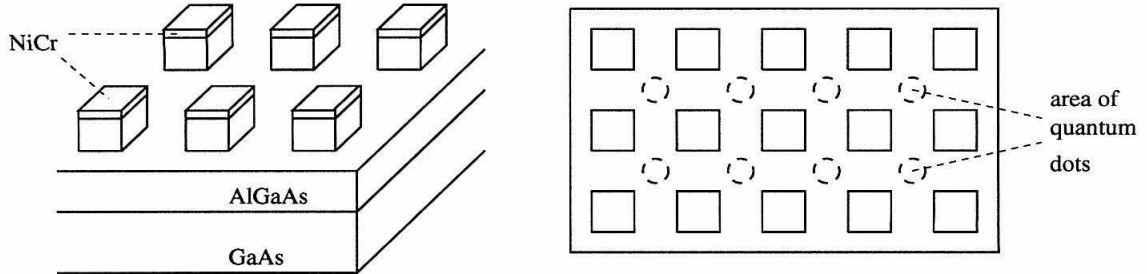
Figure 1.4: Schematic view of the gated mesas that accomplish lateral confinement (left panel). The NiCr gates are negatively charged, forcing the electrons in between the mesas in the inversion layer, as illustrated on the right panel (top view).

while ζ_n describe the electronic states inside the dot (Schrödinger domain), generating its charge

$$\rho_{qd}\left(x,y,z\right) = -2e \sum_n \zeta_n^*\left(x,y,z\right) \zeta_n\left(x,y,z\right) \times f\left(\frac{E_f - E_n}{kT}\right) \tag{1.8}$$

with f as Fermi-Dirac distribution function and E_F as Fermi energy. They were able to show that the confining potential is nearly circular despite the square geometry of the sample. For increasing magnetic fields they proved that the electrons are indeed exposed to a parabolic potential, that this potential is fairly independent of the number of electrons in the dot and that the energy levels look very similar to the Fock-Darwin levels. Fock-Darwin levels are the single-particle levels of a system with a parabolic potential and electrons that are exposed to a magnetic field which is perpendicular to the plane of motion, as explained in Section 1.2.

McEuen et al. [3] were able to perform conductance measurement on a quantum dot by putting leads near the dot. Again, a square geometry of the confining gate was used. Measuring the peak position as function of gate voltage and magnetic field in the range of $B = 2 - 4$ T, they were able to map the conductance peaks to the energy levels of an ideal parabolic quantum dot. For higher B-fields, though, the reproduction of the Fock-Darwin levels failed. This could be due to the facts that electrons do not occupy single Fock-Darwin levels at this field strength.

The electron systems are called dots (or zero-dimensional objects) because their

size is much smaller than the mean free path of electrons in the inversion layer. Electrons in the conduction band have Fermi velocities of

$$v_F \approx 10^8 \frac{\text{cm}}{\text{s}}, \tag{1.9}$$

and the time between two scattering processes of an electron can be calculated from their mobility μ as

$$\tau = \frac{m^*}{e}\mu \approx 10^{-12} \text{ s}. \tag{1.10}$$

Therefore, the mean free path of an electron in the inversion layer

$$l = v_F\tau \approx 10^{-6} \text{ m} \tag{1.11}$$

is much larger than a typical dot size of $10^{-7} - 10^{-8}$ m.

1.2   Basic Theory

In this section I describe the basic properties of electrons in one dot as they emerge from the theory. I consider m electrons of effective mass m^* in a plane (x, y) confined by an external parabolic potential,

$$V(r) = \frac{1}{2}m^*\omega_0^2 r^2 = \frac{1}{2}m^*\omega_0^2 \left(x^2 + y^2\right), \tag{1.12}$$

and subject to a strong magnetic field

$$\vec{B} = B_0\vec{e}_z. \tag{1.13}$$

The effective mass m^* is smaller than the free electron mass m_e. This is due to the fact that the electrons move in a crystal, or more specifically, in the conduction band of GaAs. To motivate this, one can imagine that the electron as a wave packet is subject to a perturbation like an electric field and experiences a change of its group

velocity

$$\dot{v} = \frac{\mathrm{d}}{\mathrm{d}t}\left(\frac{\partial\omega}{\partial k}\right) = \hbar^{-1}\frac{\mathrm{d}}{\mathrm{d}t}\left(\frac{\partial W(k)}{\partial k}\right) = \hbar^{-1}\frac{\partial^2 W(k)}{\partial k^2}\dot{k}, \tag{1.14}$$

where $W(k)$ is the energy of the band as a function of wave vector k. Since the force on the electron is given by

$$F = m^*\dot{v} \equiv \hbar\dot{k}, \tag{1.15}$$

the mass then results in

$$m^* = \hbar^2\left(\frac{\partial^2 W(k)}{\partial k^2}\right)^{-1}. \tag{1.16}$$

Even though this is not a complete quantum mechanical derivation, it already shows the correct dependence of m^* on the second derivative of $W(k)$. For GaAs,

$$m^* \approx 0.067 m_e. \tag{1.17}$$

For similar reasons the effective g-factor of GaAs is

$$g^* = -0.44. \tag{1.18}$$

Since the bands have been evolved from atomic levels of the isolated atom (c.f. tight binding model) with certain quantum numbers of angular momentum, the spin-orbit interaction and the fact that the degeneracy of atomic levels is lifted in a periodic lattice generates a g-value that is caused by many levels, thus the irregular value.

The Hamiltonian for the system is

$$\hat{H} = \sum_{i=1}^{m}\frac{1}{2m^*}\vec{\Pi}_i^2 + \frac{1}{2}\sum_{i=1}^{m}m^*\omega_0^2(x_i^2+y_i^2) + \sum_{i=1}^{m}\frac{g^*\mu_B\vec{B}\cdot\vec{S}_i}{\hbar} + \sum_{i<j}\frac{e^2}{\epsilon|\vec{r}_i-\vec{r}_j|}, \tag{1.19}$$

where $\vec{\Pi}_i = \frac{\hbar}{i}\vec{\nabla}_i + \frac{e}{c}\vec{A}(\vec{r}_i)$ is the kinetic momentum of the ith electron, choosing a symmetric gauge

$$\vec{A}(\vec{r}_i) = \frac{B_0}{2}(-y_i, x_i, 0). \tag{1.20}$$

$\epsilon = 12.9$ is the dielectric constant for GaAs. I include the spin degree of freedom of the electrons $\vec{S}_i = \pm\frac{\hbar}{2}\vec{e}_z$. While the Zeeman energy is added to the Hamiltonian, an

order-of-magnitude estimate shows that the spin-orbit interaction can be neglected: The magnetic field strength induced by the circular motion of an electron with an angular momentum of $\hbar$ at a typical distance of

$$l_0 \sim 1.0 \times 10^{-6} \text{ cm} \tag{1.21}$$

is only

$$B_{\mathcal{L}} = \frac{e\hbar}{m^* c l_0^3} \approx 2.8 \times 10^{-5} \text{ T} \tag{1.22}$$

and therefore much smaller than the external field.

Defining the frequencies

$$\omega_c = \frac{eB_0}{m^* c}, \quad \omega(B_0) = \sqrt{\omega_0^2 + \frac{1}{4}\omega_c^2}, \tag{1.23}$$

the coordinates are rewritten as dimensionless complex variables,

$$z_i = \frac{x_i - iy_i}{l_0\sqrt{2}} \tag{1.24}$$

with

$$l_0 = \sqrt{\frac{\hbar}{m^*\omega(B_0)}} \tag{1.25}$$

as so-called magnetic length, to obtain

$$
\begin{aligned}
\hat{H} &= \sum_{i=1}^{m} -\frac{\hbar^2}{m^*}\left(\frac{1}{l_0^2}\partial_{z_i}\partial_{\bar{z}_i}\right) + m^*\omega^2(B_0)l_0^2|z_i|^2 + \frac{\hbar}{2}\omega_c(\bar{z}_i\partial_{\bar{z}_i} - z_i\partial_{z_i}) \\
&+ \sum_{i=1}^{m} \frac{g^*\mu_B\vec{B}\cdot\vec{S}_i}{\hbar} + \sum_{i<j} \frac{e^2}{\epsilon\sqrt{2}l_0|\bar{z}_i - \bar{z}_j|} \\
&\equiv \sum_{i=1}^{m} \hat{H}_0(z_i, \vec{S}_i) + \frac{e^2}{\epsilon\sqrt{2}l_0}\sum_{i<j}\frac{1}{|\bar{z}_i - \bar{z}_j|}.
\end{aligned}
\tag{1.26}
$$

$\hat{H}_0$ is the single-particle Hamiltonian whose eigenfunctions will form the basis states

for the Hartree-Fock calculation. For the spatial part of $\hat{H}_0$, I define

$$a^\dagger = \frac{1}{\sqrt{2}}(\bar{z} - \partial_z), \ b^\dagger = \frac{1}{\sqrt{2}}(z - \partial_{\bar{z}}), \ a = \frac{1}{\sqrt{2}}(z + \partial_{\bar{z}}), \ b = \frac{1}{\sqrt{2}}(\bar{z} + \partial_z) \quad (1.27)$$

with $[a, a^\dagger] = [b, b^\dagger] = 1$ and write

$$
\begin{aligned}
\hat{H}_0(z) &= \hbar\omega(B_0)(a^\dagger a + b^\dagger b + 1) - \frac{1}{2}\hbar\omega_c(b^\dagger b - a^\dagger a) \\
&= \hbar\omega(B_0)(2a^\dagger a + \mathcal{L} + 1) - \frac{1}{2}\hbar\omega_c\mathcal{L} \\
&= \hbar\omega(B_0)(2b^\dagger b - \mathcal{L} + 1) - \frac{1}{2}\hbar\omega_c\mathcal{L},
\end{aligned}
\quad (1.28)
$$

where $\mathcal{L} := b^\dagger b - a^\dagger a$ is the angular momentum of the particle. The eigenvalues of the single-particle Schrödinger equation

$$\hat{H}_0\Psi_{nk} = \epsilon_{nk}\Psi_{nk} \quad (1.29)$$

are

$$\epsilon_{nk} = \hbar\omega(B_0)\{2n + |k| + 1\} - \frac{1}{2}\hbar\omega_c k. \quad (1.30)$$

These energies are called Fock-Darwin levels [4, 5]. They evolve from the well known Landau levels because the parabolic potential lifts their degeneracy. As shown in Fig. 1.5, n enumerates the levels that are Landau levels when the parabolic potential is switched off, and k differentiates levels within a Landau level. I therefore call the latter one intra-Landau level. Note that a level with a negative k value is grouped together with states of the next higher Landau level $n + 1$. The eigenfunctions of the single-particle Hamiltonian are generated from the ground state

$$\Psi_{00}(z) = \sqrt{\frac{2}{\pi}} \exp\left(-|z|^2\right) \quad (1.31)$$

by the application of a combination of the creation operators $a^\dagger$ and $b^\dagger$. For $k \geq 0$ they are

$$\Psi_{nk}(z) = \left(a^\dagger\right)^n \left(b^\dagger\right)^{n+k} \Psi_{00}(z), \quad (1.32)$$
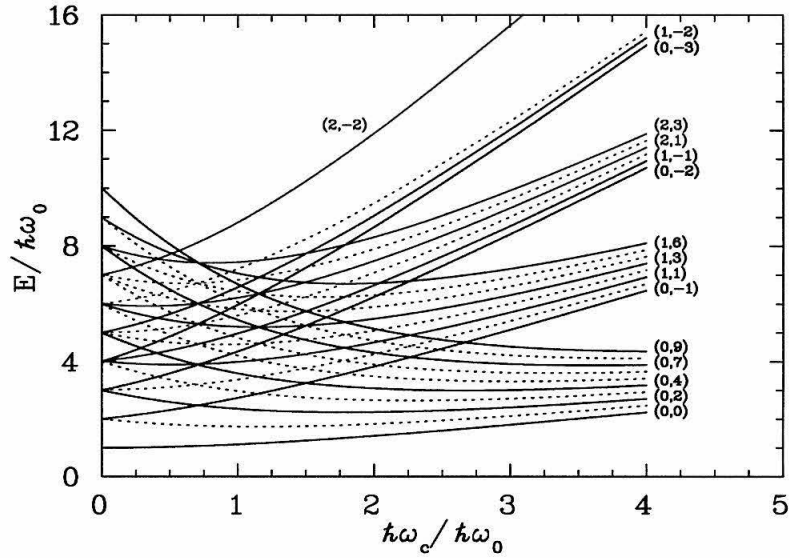
Figure 1.5: Samples of Fock-Darwin levels (n, k) as a function of cyclotron energy. The levels with the same quantum number n (Landau level) have the same color. Levels with negative k-value have energies that are of the same order as states with the next higher Landau level $n + 1$. For clarity some levels (dotted lines) have not been labeled.

while I get for $k < 0$

$$\Psi_{nk}(z) = \left(a^\dagger\right)^{n-k} \left(b^\dagger\right)^n \Psi_{00}(z).$$ (1.33)

Electrons occupying the Fock-Darwin levels are moving in concentric circles of radius

$$R_{nk} \sim l_0 \sqrt{(2n + |k| + 1)}$$ (1.34)

around the origin of the quantum dot and perpendicular to the magnetic field lines.

1.3 Rotationally Symmetric Ground States

Constraining the electrons to occupy the Fock-Darwin levels (the orbital occupation numbers are integers), the many-body state of a quantum dot consists of a single Slater determinant. Many observations can be made and have been described in literature (see as examples of many more references [6, 7, 8, 9]). The behaviour is mostly driven by two competing parts of the potential, the confining potential and the Coulomb interaction. The confining parabolic potential can effectively be controlled by the magnetic field because of Eq. (1.23). It is somewhat equivalent to talk about the confinement obtained by the parabolic potential or by the magnetic field strength. Other components that come into play are the Zeeman energy (eventually resulting in the spin flip of the electrons) and the Pauli principle which makes certain configuration more favorable than others.

At zero magnetic field strength all Fock-Darwin levels are twofold degenerated because they can be occupied by a spin-up ($\uparrow$) and a spin-down ($\downarrow$) electron. The dot is unpolarized, or its total spin is just $S = \pm\frac{1}{2}\hbar$, the spin of the one electron in the half-filled Fock-Darwin level. Furthermore, some of the higher Landau levels are energetically favored over intra-Landau levels of the lowest Landau level ($n = 0$) when the dot is filled with electrons. At higher B-fields only the lowest Landau level ($n = 0$) is occupied: For $B_0 \approx 10$ T, for example, one has $\hbar\omega_c \approx 17$ meV and

$\hbar\omega(B_0) \approx 9$ meV, and all particles occupy the Fock-Darwin states with $n = 0$:

$$\Delta\epsilon = \epsilon_{n=0L} - \epsilon_{n=0L-1} \approx 0.5 \text{ meV} \ll \epsilon_{n=0L} - \epsilon_{n=1L} \approx 18 \text{ meV}. \qquad (1.35)$$

The interplay of the three basic mechanism is very subtle as it has been shown in the articles cited above [6, 7, 8, 9]: The Coulomb interaction always favors a larger area; if there were no parabolic confinement, charge would be distributed over infinite space. The Coulomb interaction also makes spin polarization of the dot set in earlier than a naive back-of-the-envelope calculation would suggest. For again $B_0 \approx 10$ T the split in the Zeeman energy,

$$\Delta E_S = g^*\mu_B B_0 = \frac{g^* m^*}{2m_e}\hbar\omega_c \approx 0.25 \text{ meV}, \qquad (1.36)$$

is smaller than the intra-Landau level separation, but the Coulomb repulsion of an electron with the one in the same Fock-Darwin level together with the one of the neighboring level makes it energetically not advantageous to have two electrons stay in the same orbit; in addition, the radius of the electrons decreases with increasing magnetic-field strength,

$$R \sim l_0 \sim \frac{1}{\sqrt{B_0}}, \qquad (1.37)$$

making the Coulomb repulsion stronger. If the spins align, the spin part of the many-body wave function becomes symmetric, forcing the spatial part to be antisymmetric to obey the Pauli principle. This makes the electrons occupy different Fock-Darwin levels thereby reducing the Coulomb energy. This is a manifestation of Hund's rule as it is known in atomic Physics. The existence of this rule for quantum dots has been shown experimentally for small B-fields [10].

The Pauli principle, on the other hand, guarantees that the dot forms a compact disk rather than a system of separated orbits. (One could imagine that, if the confinement is not too strong, placing electrons in orbits that are sufficiently apart from each other would minimize Coulomb repulsion and make the energy disadvantage caused by the confinement not unfavorably large. The Pauli principle disallows that.)
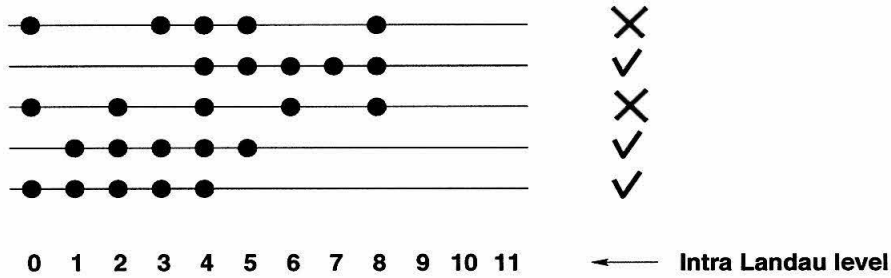
Figure 1.6: Scheme on allowed (green check mark) and disallowed (red cross) configurations for five electrons in a dot. The electron are constrained to occupy Fock-Darwin level of with $n = 0$. Occupied states are marked with a blue dot. Because of the Pauli principle the electrons form one compact disk or ring. Only for a larger number of electrons there can occur a ring *and* a disk in a dot.

The exchange potential is most attractive for two electrons in adjacent Fock-Darwin levels. If there are m electrons in a spin-polarized dot, the most stable configurations are those that form one disk or one ring as demonstrated in Fig. 1.6 or Fig. 1 of Ref. [7]. Taking into account that the level $(0, k)$ carries angular momentum $\hbar k$, the energy as a function of the total angular momentum,

$$J = \hbar \sum_{\substack{\text{occupied} \\ \text{level } j}} j, \tag{1.38}$$

has downward cusps at

$$J = \frac{m(m-1)}{2} + pm , \ p \text{ integer}. \tag{1.39}$$

These numbers of angular momentum are called magic. There will be a range of magnetic-field strengths for which a so-called maximal density droplet exists: Fock-Darwin levels are occupied, starting from $(0, 0)$ until $(0, m)$; all levels are occupied once, yielding in a spin-polarized system. The next most stable configuration is then accomplished by taking out the most inner electron and putting it next to the outmost electron, and so on.

Nevertheless, it is not clear whether a dot filled with an arbitrarily large number

of electrons is a compact disk or ring for all values of B_0. In fact, A.H. MacDonald [8] and C. de C. Chamon [9] showed that bulk instabilities occur somewhere in the middle of the maximum density droplet and not at the center or at the edge when the confining potential is made weaker or the Coulomb interaction stronger. Electrons in the bulk are taken out and put next to the outmost electron at some critical value of B_0, forming a disk *and* a ring (cf. Fig. 11 of Ref. [9]). The quasiparticle energy, which is the cost or gain in energy of adding or removing an electron in a particular Fock-Darwin level, is higher for the occupied states within the bulk, not at the center, than those unoccupied at the edge, making it energetically possible to break up the maximum density droplet. Even though an investigation of rotationally symmetric many-body states is not the subject of this project, I made similar observations and will mention them in Section 4.1. However, this summary already shows a very richness of phenomena and observations that can be identified in quantum dots and is caused by quite elementary effects.

Chapter 2   Aim of the Calculation

The scenarios discussed in the last chapter assume an unbroken rotational symmetry. But it is not obvious that the real ground state has to be rotationally symmetric. The bulk instabilities that develop for high fields indicate that the system might be frustrated because the electrons are forced to occupy Fock-Darwin levels. The Coulomb repulsion becomes the strongest part in the Hamiltonian for high fields and cannot be viewed as a perturbation anymore. One can imagine a situation in which adding an electron to an existing rotationally symmetric system perturbs the electrons so much that they are being "thrown out" of their orbits (or better said: the dot is polarized) by that valence electron. This is very similar to the Physics of deformed nuclei: A spherical (closed shell) nucleus has deformed neighbors in the table of nuclei because the additional valence nucleons polarize the remaining core nucleons and induces higher moments. Many investigations on quantum dots, among them some of those mentioned in the last chapter, simply do not allow for these considerations because of the restriction of electrons having to occupy Fock-Darwin levels.

Other authors have considered the possible existence of not rotationally symmetric ground states. Maksym [7] considers a "large angular momentum limit" of systems up to five electrons and describes only excited states of integer angular momentum. He speculates on the existence of ground state Wigner molecules in the large-field limit. Bolton and Rössler [11] simulated up to forty *classical* interacting point charges in an external parabolic potential, neglecting kinetic terms. Their model is aimed at understanding which charge distribution in a Wigner state is caused by the interaction. Their simulation is Monte Carlo like, agitating particles according to a Maxwell-Boltzmann distribution $\exp\left(-\Delta E/k_B T\right)$, ΔE being the energy difference between two configurations of electrons. They observe a distinct spatial structure of minimum energy clusters with up to four ring-like shells. They also give an illustration how

some configurations for a fixed number of electrons are very close to degeneracy by calculating the energies of a transition between two configurations. They find that, especially for 6, 10, 12, 14 and 17 electrons, alternative clusters with almost identical energies occur which will turn out to be an important finding in my calculation too. Nevertheless, their investigation can only be considered qualitative because the full Hamiltonian is not considered, the electrons are treated as point charges and a quantum mechanical treatment is not attempted.

In this project I solve the full quantal problem of up to twenty electrons in a quantum dot. I consider ground state properties of these systems in the limit of a strong magnetic field. I treat the problem by solving the Hartree-Fock equations, but emphasizing on the search of not rotationally symmetric ground states. This can be accomplished by two approaches: First performing a constrained Hartree-Fock calculation, forcing the electrons to shape like a dipole, quadrupole or a higher moment; secondly, by starting an ordinary Hartree-Fock calculation with arbitrary, but not rotationally symmetric initial conditions (Hartree-Fock is a self-consistent method). The latter one will turn out to be successful. After a brief description of the well known phases of the rotationally symmetric case as they appear in the Hartree-Fock approximation, I present the gradual transition towards a Wigner molecule and crystal; the various spatial configurations are shown and the shell structure is compared to that of the classical calculation [11]. I further describe a variational Monte Carlo calculation which I performed to improve the wave function by a Jastrow ansatz. Finally, I investigate the rotational spectra associated with the breaking of the continuous rotational symmetry; the heat capacity associated with this new rotational degree of freedom is calculated and a method to detect Wigner molecule experimentally is suggested. The results presented here have been published [15].

Chapter 3   Hartree-Fock Approximation for Quantum Dots

3.1   Theory

I restrict my calculation to the $n = 0$ level because for a high magnetic-field strength only the lowest Landau level is involved, as pointed out in Section 1.3. The eigenfunctions are

$$\Psi_k \sim z^k \exp(-|z|^2) \tag{3.1}$$

and are identical to the usual form

$$\phi_k \sim e^{-ik\varphi} r^k L_0^{|k|}(r) \exp(-\frac{r^2}{2l_0^2}), \tag{3.2}$$

$L_0^{|k|}(r)$ being the Laguerre polynomial of degree zero.

In the Hartree-Fock calculation, the Hartree-Fock energy

$$
\begin{aligned}
E^{HF} &= \langle \Phi | \hat{H} | \Phi \rangle = \sum_{l_1 l_2} t_{l_1 l_2} \langle \Phi | c_{l_1}^\dagger c_{l_2} | \Phi \rangle + \frac{1}{4} \sum_{\substack{l_1 l_2 \\ l_3 l_4}} \bar{v}_{l_1 l_2 l_3 l_4} \langle \Phi | c_{l_1}^\dagger c_{l_2}^\dagger c_{l_4} c_{l_3} | \Phi \rangle \\
&= \sum_{l_1 l_2} t_{l_1 l_2} \rho_{l_2 l_1} + \frac{1}{2} \sum_{\substack{l_1 l_2 \\ l_3 l_4}} \rho_{l_3 l_1} \bar{v}_{l_1 l_2 l_3 l_4} \rho_{l_4 l_2}
\end{aligned}
\tag{3.3}
$$

is minimized with

$$\rho_{l_1 l_2} = \langle \Phi | c_{l_2}^\dagger c_{l_1} | \Phi \rangle \tag{3.4}$$

being the density matrix and $|\Phi\rangle$ a Slater determinant. $c_l^\dagger$ creates a fermion in the state Ψ_l, while its Hermitian conjugate c_l destroys it. The second part of Eq. (3.3) can be derived using Wick's theorem [12]. The indices $l_i = (k_i, s_i)$ run over all orbital states k, as well as the spin degree of freedom $s = \{+\frac{1}{2}, -\frac{1}{2}\}$. In this notation, the

single-particle matrix element is given by

$$t_{l_1 l_2} = \langle \Psi_{l_1} | \hat{H}_0 | \Psi_{l_2} \rangle = \epsilon_{k_1} \delta_{k_1 k_2} + (-1)^{s_1 + \frac{1}{2}} \frac{g^* \mu_B B_0}{2} \delta_{s_1 s_2} \qquad (3.5)$$

with

$$\epsilon_{k_1} = \hbar \omega (B) (k_1 + 1) - \frac{1}{2} \hbar \omega_c k_1, \qquad (3.6)$$

and $\bar{v}$ is the antisymmetrized Coulomb matrix element,

$$\bar{v}_{l_1 l_2 l_3 l_4} = \frac{e^2}{\epsilon \sqrt{2} l_0} \begin{cases} \langle k_1 k_2 | \frac{1}{|z_i - z_j|} | k_3 k_4 \rangle - \langle k_1 k_2 | \frac{1}{|z_i - z_j|} | k_4 k_3 \rangle & \text{if } s_3 = s_4, \\ \langle k_1 k_2 | \frac{1}{|z_i - z_j|} | k_3 k_4 \rangle & \text{if } s_3 \neq s_4. \end{cases} \qquad (3.7)$$

To evaluate these two-body matrix elements in the two-electron Fock-Darwin representation (z_i, z_j),

$$|k_3 k_4\rangle = \frac{2^{(k_3 + k_4 + 2)/2}}{\pi \sqrt{k_3! k_4!}} (z_i)^{k_3} (z_j)^{k_4} \exp \left(-|z_i|^2 - |z_j|^2 \right), \qquad (3.8)$$

I switch to the variables

$$z_+ = \frac{1}{\sqrt{2}} (z_i + z_j), \quad z_- = \frac{1}{\sqrt{2}} (z_i - z_j) \qquad (3.9)$$

and yield

$$|k_3 k_4\rangle = \frac{2 \exp \left(-|z_-|^2 - |z_+|^2 \right)}{\pi \sqrt{k_3! k_4!}} \sum_{p=0}^{k_3 + k_4} \sum_i (-1)^i \binom{k_3}{p-i} \binom{k_4}{i} (z_+)^{k_3 + k_4 - p} (z_-)^p . \qquad (3.10)$$

The overlap with the new representation (z_+, z_-), indicated by the letters n and l,

$$|nl\rangle = \frac{2^{(n+l+2)/2}}{\pi \sqrt{n! l!}} (z_+)^n (z_-)^l \exp \left(-|z_+|^2 - |z_-|^2 \right), \qquad (3.11)$$

is then given by

$$\langle nl | k_3 k_4 \rangle = \delta_{n+l, k_3+k_4} \sqrt{\frac{n! l!}{k_3! k_4!}} \frac{1}{\sqrt{2^{n+l}}} \sum_i (-1)^i \binom{k_3}{l-i} \binom{k_4}{i}. \qquad (3.12)$$

The matrix elements for the Coulomb interaction in (z_+, z_-) coordinates are then easily calculated as

$$\langle nl | \frac{1}{|z_-|} | n'l' \rangle = \sqrt{2} \frac{\Gamma\left(l + \frac{1}{2}\right)}{\Gamma\left(l + 1\right)} \delta_{nn'} \delta_{ll'} \equiv \mathcal{V}\left(l\right) \delta_{nn'} \delta_{ll'}, \tag{3.13}$$

and in the (z_i, z_j) representation

$$\langle k_1 k_2 | \frac{1}{|z_-|} | k_3 k_4 \rangle = \sum_{nl} \mathcal{V}\left(l\right) \langle k_1 k_2 | nl \rangle \langle nl | k_3 k_4 \rangle. \tag{3.14}$$

Γ is the Gamma function. Note that because of the overlap functions (3.12), the k_i's have to fulfill $k_1 + k_2 = k_3 + k_4$, which means that angular momentum is conserved as required from the Coulomb interaction.

To obtain the ground state within the space of Slater determinants, I minimize the Hartree-Fock energy (3.3) by varying with respect to ρ,

$$\frac{\delta E^{HF}}{\delta \rho} = 0. \tag{3.15}$$

It has to be ensured that the solution stays within the set of Slater determinants and that the number of particles is conserved:

$$\rho^2 = \rho \, , \ \mathrm{tr}\rho = m. \tag{3.16}$$

This results in a matrix diagonalization problem

$$\sum_j h_{ij} D_{jk} = \sum_j \left(t_{ij} + \sum_{ll'} \bar{v}_{il'jl} \rho_{ll'} \right) D_{jk} = \sum_j \left(t_{ij} + \Theta_{ij} \right) D_{jk} = \varepsilon_k D_{ik}, \tag{3.17}$$

where Θ is the so-called mean field. The eigenvectors $\vec{D}_k$ of h represent the new single-particle states $\{k\}$, that are to be occupied according to the energies ε_k. They are the new Hartree-Fock basis. Eq. (3.17) has to be solved self-consistently, since

$$\rho_{ll'} = \sum_{i=1}^{m} D_{li} D_{l'i}^*, \tag{3.18}$$

which means that the matrix depends on its eigenvectors. ρ is diagonal because of (3.16). This suggests the following procedure (unconstraint Hartree-Fock):

1. Calculate the single-body part t of the Hamiltonian.

2. Set the initial condition in $\vec{D}_k$ according to the aim of the calculation, in this case a not rotationally symmetric condition. From that, calculate ρ.

3. Calculate the mean field Θ.

4. Diagonalize $h = t + \Theta$ and obtain the new single-particle wave functions $\vec{D}_k$ and energies ε_k.

5. Calculate ρ from the new functions.

6. Calculate the Hartree-Fock energy

$$E^{HF} = \sum_{k=1}^{m} \varepsilon_k - \frac{1}{2} \sum_{\substack{l_1 l_2 \\ l_3 l_4}} \rho_{l_3 l_1} \bar{v}_{l_1 l_2 l_3 l_4} \rho_{l_4 l_2}. \tag{3.19}$$

7. Repeat 3 to 6 until E^{HF} has converged.

The Hartree-Fock approximation is known to conserve symmetries present in the initial trial wave function. To generate deformed solutions, I started with a quite arbitrary, but not rotationally invariant, initial Slater determinant, which produces a deformed initial mean field. Self consistent iteration of the Hartree-Fock scheme guarantees amplification of solutions with the symmetry of the Wigner molecule. Of course, the same converged solution must be reached for several different initial states to give confidence that it is the true minimum.

The other way of investigating deformed ground states is by introducing a constraint on the dot in form of an external field, as mentioned earlier. I used the method of Lagrange multiplier to impose the condition. This is known as constraint Hartree-Fock. I searched for new ground states by applying dipole and quadrupole fields, but was not able to find a minimum with a lower energy than those presented in Chapter 4.1.

3.2   Test Cases

I take into account up to 200 single-particle states (including spin). I tested my code by comparison with the results of Pfannkuche et al. [13] and Bolton [14]. Pfannkuche et al. perform Hartree, Hartree-Fock and an exact calculation of quantum dot Helium, which is a dot filled with two electrons. They consider states with integer total angular momentum, remain mostly in a region of the magnetic field strength B_0 where crystallization does not play a role, and their basis states include two Landau-levels and their intra Landau-levels.

Although their model space is different from mine, my ground state energies of total angular momentum $J = 1$ for 0 T $\leq B_0 \leq$ 5 T coincide with their Hartree-Fock calculation within less then 2%, and the $J = 0$ ground state energies agree with less than 5%. As one can see in Table I of reference [13], the $n \neq 0$ coefficients in their $J = 0$ ground state are larger than in their $J = 1$ ground state, so that the $n \neq 0$ space is more significant for those magnetic-field strengths. Their exact result for $J = 0$ is also quite different from their Hartree-Fock result, and they go on investigating the correlation energy responsible for this deviation, which is ignored in a Hartree-Fock calculation. In general, the accuracy of a mean field calculation increases with increasing number of electrons, but an exact calculation which relies on a direct diagonalization is out of range for a higher number of electrons.

Similar results are obtained if I compare my results to the fixed node Monte Carlo calculation of reference [14]. A fixed node Monte Carlo calculation evolves the probability density of the electrons in imaginary time from a trial wave function with a given fixed nodal structure. The nodal structure is imposed to avoid dealing with the fermion sign problem. This makes the method approximate. The purpose of this evolution is to filter out the ground state of the system. At its core is the imaginary time Schrödinger equation which is almost equivalent to a diffusion equation. They are investigating a system with one to ten electrons. Their trial wave function is a Laughlin-like state which is usually used to describe fractional quantum hall effects. In the spin polarized case my ground state energies agree within a few percent, while

I overestimate the energy of the depolarized system by up to 15%. This is due to the larger correlation energies when two electrons can occupy the same orbital. Since the questions addressed in this thesis concern the spin polarized regime, this deviation from the results of [14] is of little concern.

Chapter 4   Numerical Results

4.1   Phase Transition Towards a Wigner Molecule

As mentioned earlier, I have used the material constants of GaAs (i.e., $m^* = 0.067\,m_e$ and $\epsilon = 12.9$), as well as an external potential strength of

$$\hbar\omega_0 = 3\;\text{meV} \tag{4.1}$$

for my calculation. To observe the expected phase transition, I first consider a system of $m = 10$ electrons. Fig. 4.1 shows the ground state energy as a function of the magnetic field strength B_0 and, for comparison, the lowest energy of the rotationally symmetric system. The Wigner molecule becomes the ground state for $B_0 \geq 5.2$ T, while at smaller strengths the rotationally symmetric state is favored. The system undergoes spin polarization from $B_0 = 0$ T to 1.5 T, where the spin polarized so-called maximum density droplet [8] prevails. At $B_0 = 4.5$ T bulk instabilities result in unoccupied inner Fock-Darwin states. The transition to a Wigner molecule, and later to a crystal, happens very gradually. I refer to the case where the probability density is deformed, but still very smeared out as a "molecule," while a "crystal" signifies well localized and distinguishable electrons, as illustrated in Fig. 4.2. The molecule at $B_0 = 6$ T is lower in energy by only 0.2% (0.542 meV) relative to the rotationally symmetric solution, while the crystal at $B_0 = 10$ T gains about ~ 3 meV, which is of order of the strength of the confining potential. Note that the deformed ground states are not eigenstates of the total angular momentum operator $J = \sum_i \mathcal{L}^{(i)}$.

The breaking of symmetry this phase transition relies on is the change of the *continuous* symmetry, which is an invariance under the rotation about an infinitesimal angle, towards a *discrete* one. Most molecules are still invariant under a rotation by 180°, but whether there exist additional discrete and finite angles of invariance
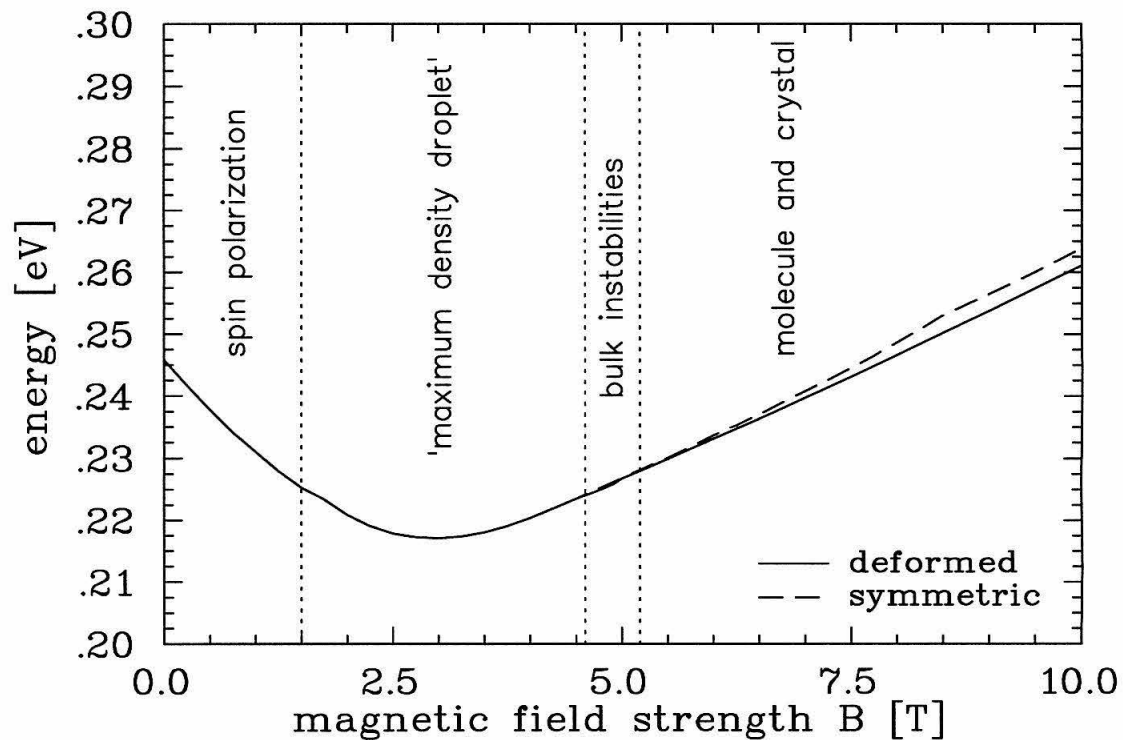
Figure 4.1: Ground state energies of the Wigner molecule (solid line) and lowest rotationally symmetric state (dashed line) as a function of magnetic field strength for ten electrons.
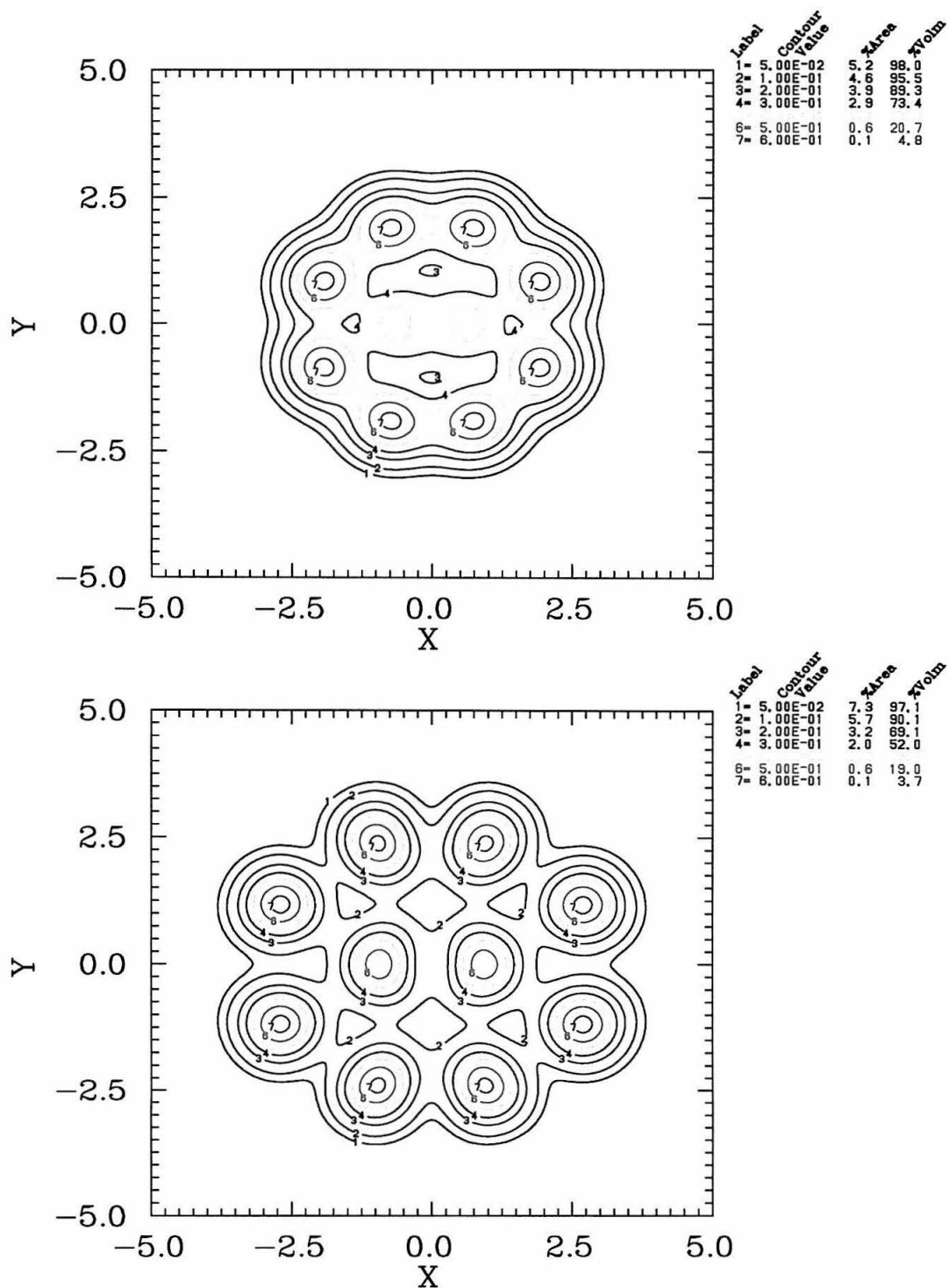
Figure 4.2: The electron density distribution for $m = 10$ electrons. The upper panel shows the solution at $B_0 = 6$ T, the lower at $B_0 = 10$ T.
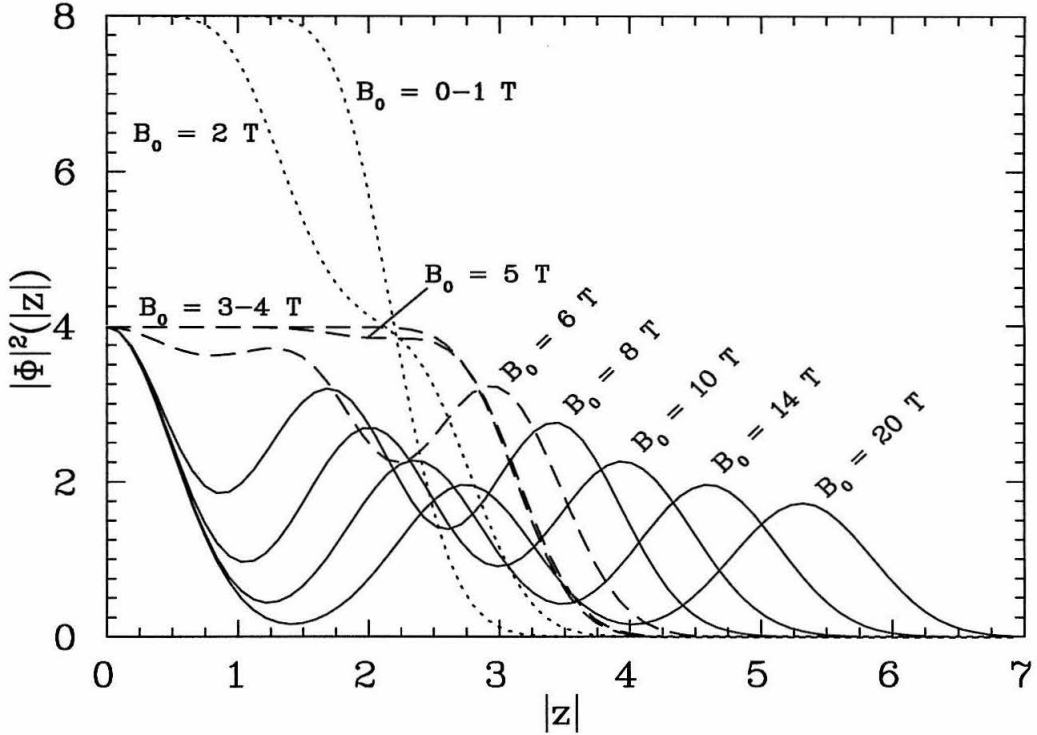
Figure 4.3: Radial electron density of $m = 20$ electrons for different values of B_0. The green solid curves represent Wigner crystals, while the red dashed curves show the slow transition to a maximum density droplet, which is reached at $B_0 = 4$ T. Depolarization sets in for the cases of the black dotted curves.

depends on the explicit spatial structure of the molecule.

The rotationally symmetric case suffers further complication with increasing magnetic-field strength: While at first ($B_0 \approx 6$ T) the hole in the bulk widens (the $l = 1, 2, 3$ Fock-Darwin levels empty), later at $B_0 = 6.75$ T a fourth state empties, resulting in an electron in the center and a ring outside. The solution eventually transforms into two separate rings at $B_0 \geq 9$ T.

For further insight into the various transitions, the radial (angle-averaged) particle distribution for various magnetic fields is shown in Fig. 4.3 for $m = 20$ electrons. The crystalline state has 1 electron in the center of the dot, 7 in a middle ring and 12 electrons in the outmost region. Correspondingly, the $B_0 = 20$ T curve shows three maxima. For $B_0 = 6$ T the center electron and the seven in the middle ring have
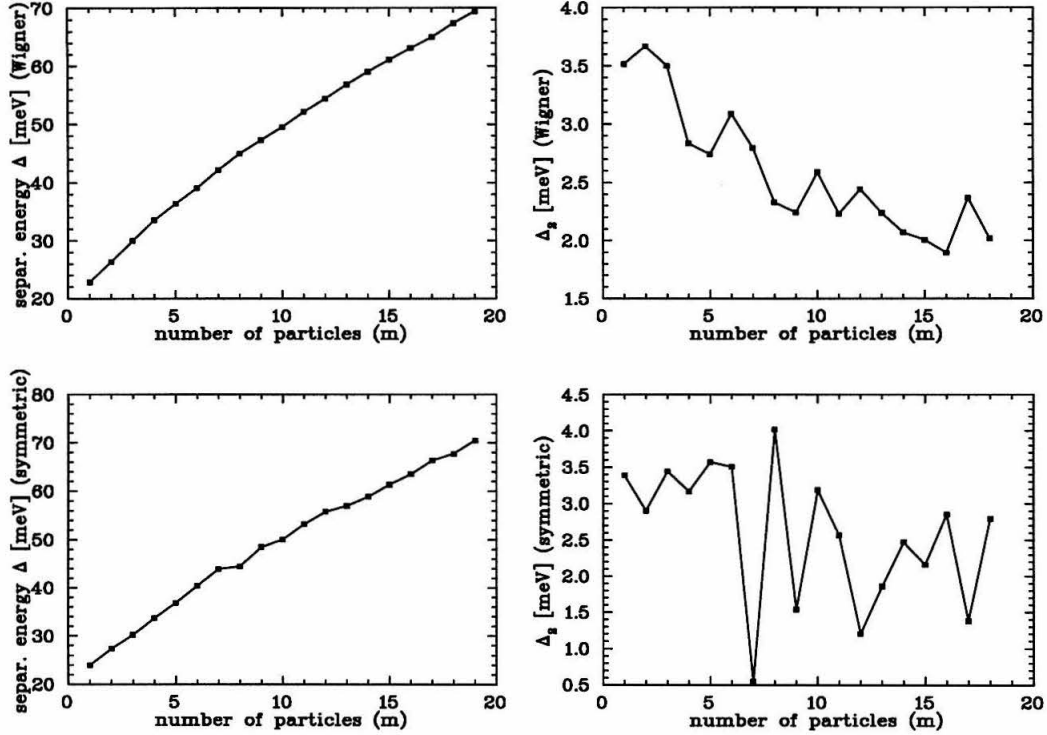
Figure 4.4: Separation energy $\Delta(m)$ and the differences in the separation energy $\Delta_2(m)$ for Wigner molecules (upper two diagrams) and for the lowest available rotationally symmetric states (lower two diagrams).

almost uniformly merged to a flat distribution which extends to $z \approx 2$, and the outer ring can now be found at $z \approx 3$. For $B_0 = 3 - 4$ T I find again the so-called maximum density droplet: the electrons occupy the first twenty Fock-Darwin levels, since they are polarized. Further lowering of B_0 results in a depolarization, allowing further accumulation of electrons near the origin. Since I only take into account $n = 0$ states, I cannot claim to represent the physical situation for the smaller field strength, although I do reproduce the energies in this regime quite well, as noted above.

In Fig. 4.4 I plot the separation energy,

$$\Delta(m) = E_{m+1} - E_m, \tag{4.2}$$

and the differences in the separation energy,

$$\Delta_2(m) = \Delta(m+1) - \Delta(m), \qquad (4.3)$$

as functions of the particle number m in the crystal regime, $B_0 = 20$ T. There is a large drop in Δ_2 of ~ 0.5 meV whenever charge can be put to the outer region of the dot (see, e.g., $m = 4$ and $m = 8$), in accord with charge being distributed over a larger area, thereby reducing the Coulomb energy. In the case where one charge is placed in the center and two rings outside ($m = 14$), the gain in energy is reduced by the fact that more particles outside feel a stronger external potential. The tendency here is that the Coulomb energy plays a less and less important role, weakening the slope in the separation energy, combined with the fact that more particle can be packed in the outer region.

For comparison, I also show $\Delta(m)$ and $\Delta_2(m)$ in Fig. 4.4 for the lowest rotationally symmetric state. No clear tendency in the behaviour of $\Delta_2(m)$ is evident. The system is frustrated by the particles having to occupy Fock-Darwin levels.

In Table 4.1 I show the spatial configurations of the system in the Wigner-like structure (obtained by enumerating the number of electrons occupying the corresponding rings) and give the ground state energies. I generally confirm the configurations (spatial shell structure) of the classical calculation of reference [11] as well as the exceptional behaviour of the $m = 6, 10, 12$ and 17 clusters, although there is no peak in Δ_2 for $m = 14$ (the peaks in Fig. 4.4 correspond to the cusps of Fig. 5 of reference [11]), since ten electrons are moved outside for the $m = 16$ configuration.

In Fig 4.5 I plot the phase diagram with respect to number of particles and the ratio $\frac{\omega_c}{\omega_0}$. I omit the regime of bulk instabilities, since it is of minor importance. The phase boundary of the spin polarized regime and the partially unpolarized regime suffers again from the Hartree-Fock approximation, as it bends down with decreasing number of electrons. The boundary crosses the m-axis at too high values of m. Only for m=1 there cannot be an unpolarized region if $\frac{\omega_c}{\omega_0} \neq 0$. The boundary of the molecular regime is defined by how much the continuous rotational symmetry is
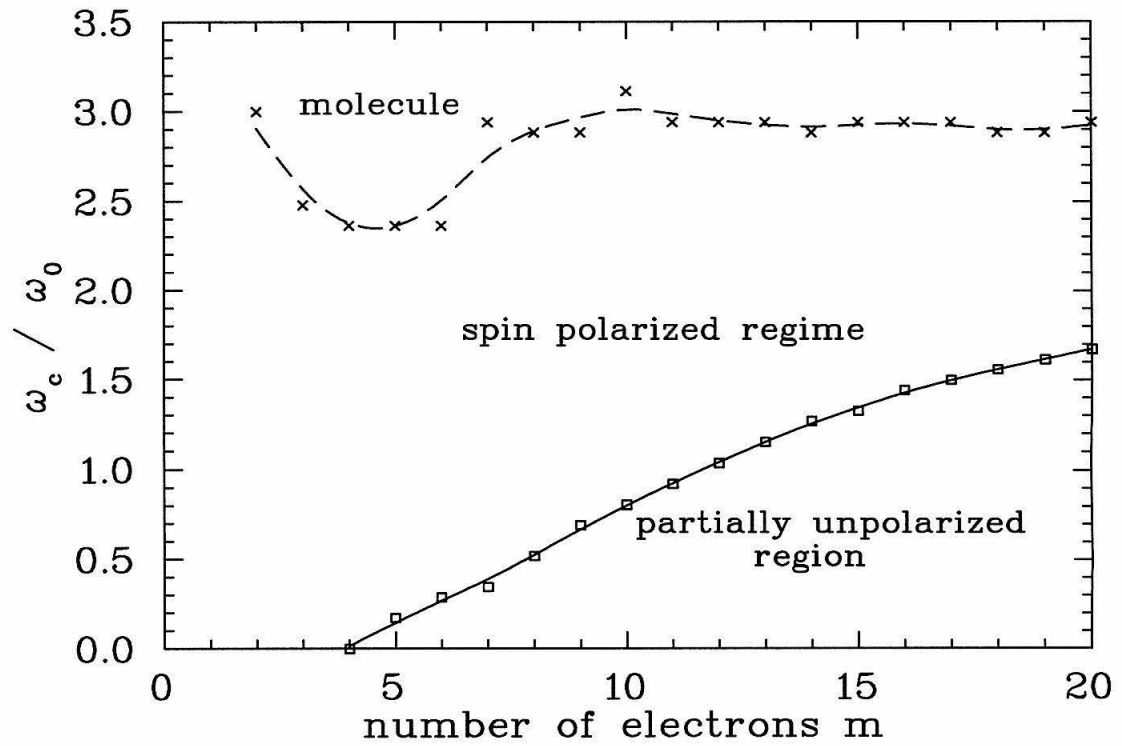
Figure 4.5: Phase diagram for quantum dots, plotting $\frac{\omega_c}{\omega_0}$ versus the number of electrons (m). The lines crudely trace the boundaries to guide the eye.

number of electrons	energy [meV]	ring occupations inner − middle − outer
1	17.247	1 − 0 − 0
2	40.085	2 − 0 − 0
3	66.439	3 − 0 − 0
4	96.463	4 − 0 − 0
5	129.986	5 − 0 − 0
6	166.346	1 − 5 − 0
7	205.448	1 − 6 − 0
8	247.636	1 − 7 − 0
9	292.621	2 − 7 − 0
10	339.934	2 − 8 − 0
11	389.489	3 − 8 − 0
12	441.634	3 − 9 − 0
13	496.008	4 − 9 − 0
14	552.825	4 − 10 − 0
15	611.879	5 − 10 − 0
16	673.004	1 − 5 − 10
17	736.135	1 − 5 − 11
18	801.162	1 − 6 − 11
19	868.558	1 − 6 − 12
20	937.973	1 − 7 − 12

Table 4.1: Ground state energies and spatial distributions of Wigner crystals in quantum dots for up to twenty electrons at $B = 20$ T.

broken: the fractional uncertainty in the total angular momentum is

$$f = \frac{\Delta J}{\langle \hat{J} \rangle} = \frac{\sqrt{\langle \hat{J}^2 \rangle - \langle \hat{J} \rangle^2}}{\langle \hat{J} \rangle}, \tag{4.4}$$

and I define a molecule by

$$f > 1\%. \tag{4.5}$$

The boundary is fairly constant for $m > 6$, but, since the transition is gradual, it has some uncertainty. For less than seven particles, I find a small drop in the boundary, due either to some non-obvious physical effect or to the approximation I use.

4.2 Variational Monte Carlo Calculation for Wigner Molecules

The Hartree-Fock calculation is based on a theory of independent particles moving in an average potential. I improved the wave functions for the Wigner regime to a many-body wave function by introducing a Jastrow-type function

$$|\Psi\rangle = \left(\mathcal{S} \prod_{i<j} f(z_i - z_j) \right) |\Phi_{HF}\rangle \qquad (4.6)$$

where $\mathcal{S}$ is the symmetrizer and $|\Phi_{HF}\rangle$ the Hartree-Fock solution to the problem. To guarantee a convenient symmetrized form of the product of this function, I made the ansatz

$$f(z_i - z_j) = |z_i - z_j|^k \qquad (4.7)$$

for the pair correlation function $f(z_i - z_j)$ with k as a variational parameter. Note that this ansatz does not take into account phases, thereby reducing the model space a bit. Also, this ansatz treats all electrons on an equal footage and does not take into account the already established spatial structure other than through the Slater determinant. So this calculation should be viewed as a benchmark of how good the Hartree-Fock solution already is. If the energy cannot be improved significantly, then some confidence in the Hartree-Fock solution can be established.

I performed a variational Monte Carlo calculation [16] to evaluate the energy

$$E[k] = \frac{\langle \Psi(k) | H | \Psi(k) \rangle}{\langle \Psi(k) | \Psi(k) \rangle}. \qquad (4.8)$$

The Monte Carlo procedure is used to evaluate the integrals in numerator and denominator. They rely on the Metropolis algorithm [17] which is described in more detail in the second part of this thesis. The difference between this, a *variational* calculation, and an auxiliary field Monte Carlo is that the variational calculation only gives an upper bound on the energy, while the auxiliary field Monte Carlo is an exact thermal description of a physical system. By searching for a minimum of $E[k]$ in the

parameter space (in this case it is the one-dimensional k-space), I obtain an estimate for the true ground state energy and wave function. The integrals are evaluated by introducing a weight function $W(\{\vec{R}\})$, $\{\vec{R}\}$ being the set of spatial coordinates of the electrons, according to which samples of the integrands are taken:

$$E\left[k\right] = \frac{\int \mathrm{d}^m \vec{R} \frac{\Psi^\dagger(\{\vec{R}\})H\Psi(\{\vec{R}\})}{W(\{\vec{R}\})} W(\{\vec{R}\})}{\int \mathrm{d}^m \vec{R} \frac{\Psi^\dagger(\{\vec{R}\})\Psi(\{\vec{R}\})}{W(\{\vec{R}\})} W(\{\vec{R}\})} \tag{4.9}$$

The weight function $W(\{\vec{R}\})$ samples the important regions of the integrand, thereby reducing the computational burden a lot, if compared to a space discretization scheme. This results in taking averages of samples of the integrands:

$$E\left[k\right] = \frac{\sum \frac{\Psi^\dagger(\{\vec{R}\})H\Psi(\{\vec{R}\})}{W(\{\vec{R}\})}}{\sum \frac{\Psi^\dagger(\{\vec{R}\})\Psi(\{\vec{R}\})}{W(\{\vec{R}\})}}. \tag{4.10}$$

Since this is a stochastic approach, there is a statistical error connected with an observable calculated, but it is of no significance for this particular application.

As it turned out, the Jastrow type wave function did not significantly improve the Hartree-Fock energy. In the case of ten electrons and $B = 20$ T, the energy could only be improved by 0.1% (0.4 meV) at $k = 0.1$. For $0.1 < k < 1$ the energy is slowly increasing, while for $k > 1$ highly excited states are simulated as more holes are introduced into the wave function. Obviously, the Hartree-Fock solution already describes the Wigner state accurately.

4.3   Rotational Spectra

In my Hartree-Fock solutions of ten or more electrons and $B_0 = 20$ T, the relative uncertainty in total angular momentum, f, is of order of 10% which is a consequence of the fact that total angular momentum is not conserved. As in atomic nuclei, these deformed solutions give rise to rotational spectra, which do not appear in the case of the unbroken symmetry. I have estimated the spectrum of rotational excitations by

projecting the Hartree-Fock Slater determinant onto eigenfunctions of good angular momentum I. Thus, this method is a projection after variation [18]. It does not enforce the variation principle exactly. However, the projected wave function

$$|\tilde{\Phi}\rangle = \hat{P}^I|\Phi\rangle \qquad (4.11)$$

introduces much more correlation than the single Slater determinant obtained by the Hartree-Fock solution alone, and is a superposition of many slater determinants. It should therefore produce a lower energy than E^{HF}. The projector has the form

$$\hat{P}^I = \frac{1}{2\pi}\int_0^{2\pi} e^{i\alpha(\hat{J}-I)}\mathrm{d}\alpha \qquad (4.12)$$

and obeys the usual relations

$$\hat{P}^2 = \hat{P} \ , \ \hat{P}^\dagger = \hat{P}. \qquad (4.13)$$

The energies which result from taking the mean value of $\hat{H}$ with the projected wave functions are given by

$$E^I_{proj} = \frac{\langle\Phi|\hat{P}^{I\dagger}\hat{H}\hat{P}^I|\Phi\rangle}{\langle\Phi|\hat{P}^{I\dagger}\hat{P}^I|\Phi\rangle} = \frac{\langle\Phi|\hat{H}\hat{P}^I|\Phi\rangle}{\langle\Phi|\hat{P}^I|\Phi\rangle} = \frac{\int \mathrm{d}\alpha h(\alpha)e^{-iI\alpha}}{\int \mathrm{d}\alpha n(\alpha)e^{-iI\alpha}}, \qquad (4.14)$$

defining the quantities

$$h(\alpha) = \langle\Phi|\hat{H}e^{i\alpha\hat{J}}|\Phi\rangle \qquad (4.15)$$

$$n(\alpha) = \langle\Phi|e^{i\alpha\hat{J}}|\Phi\rangle. \qquad (4.16)$$

Note that $\hat{H}$ and $\hat{P}^I$ commute which indicates that the symmetry the projector represents (in this case rotational invariance) is conserved, while the wave function itself is symmetry violating. $h(\alpha)$ and $n(\alpha)$ are sharply peaked around $\alpha = 0$, since $e^{i\alpha\hat{J}}$ as a rotation operator rotates the wave function out of its original position quite quickly. Since the standard deviation in $\hat{J}$ is only of few percent, these matrix elements can

be approximately calculated by writing $h(a)$ in the expansion [19]

$$h(\alpha) = \sum_{n=0}^{K} h_n \left(-\langle \hat{J} \rangle + \frac{1}{i} \frac{\partial}{\partial \alpha} \right)^n n(\alpha) \equiv \sum_{n=0}^{K} h_n \hat{\mathcal{J}}^n n(\alpha), \qquad (4.17)$$

defining

$$\hat{\mathcal{J}} = -\langle \hat{J} \rangle + \frac{1}{i} \frac{\partial}{\partial \alpha}. \qquad (4.18)$$

One justifies this ansatz with the fact that it represents a Taylor expansion of the Fourier transformed function $h(\alpha)/n(\alpha)$ because the Fourier transform of derivatives can be expressed as powers in $\hat{\mathcal{J}}$. Assuming that both quantities are sharply peaked at $\alpha = 0$, this quotient is smooth and can be approximated by a few terms of Eq. (4.17). By operating $\hat{\mathcal{J}}$ on Eq. (4.17) and setting $\alpha = 0$, an inhomogeneous system of equations can be obtained for the unknown $h_0...h_K$:

$$\langle H(\Delta \hat{J})^m \rangle = \sum_{n=0}^{K} h_n \langle (\Delta \hat{J})^{m+n} \rangle \qquad (4.19)$$

with

$$\Delta \hat{J} = \hat{J} - \langle \hat{J} \rangle. \qquad (4.20)$$

Eq. (4.14) can then be expressed as

$$E^I_{proj} = \sum_{n=0}^{K} h_n (I - \langle \hat{J} \rangle)^n. \qquad (4.21)$$

I restrict myself to $K = 2$, since higher terms involve the calculation of k-body operators with $k > 4$. This restriction should not influence the results significantly, because the Physics of rotational excitation are already captured in the first few terms. For this case, I have

$$h_2 = \frac{\langle \Delta \hat{J}^2 \rangle \langle \hat{H} \Delta \hat{J}^2 \rangle - \langle \Delta \hat{J}^3 \rangle \langle \hat{H} \Delta \hat{J} \rangle - \langle \Delta \hat{J}^2 \rangle^2 \langle \hat{H} \rangle}{\langle \Delta \hat{J}^2 \rangle \langle \Delta \hat{J}^4 \rangle - \langle \Delta \hat{J}^3 \rangle^2 - \langle \Delta \hat{J}^2 \rangle^3}$$

$$h_1 = \frac{\langle \hat{H} \Delta \hat{J} \rangle}{\langle \Delta \hat{J}^2 \rangle} - h_2 \frac{\langle \Delta \hat{J}^3 \rangle}{\langle \Delta \hat{J}^2 \rangle}$$
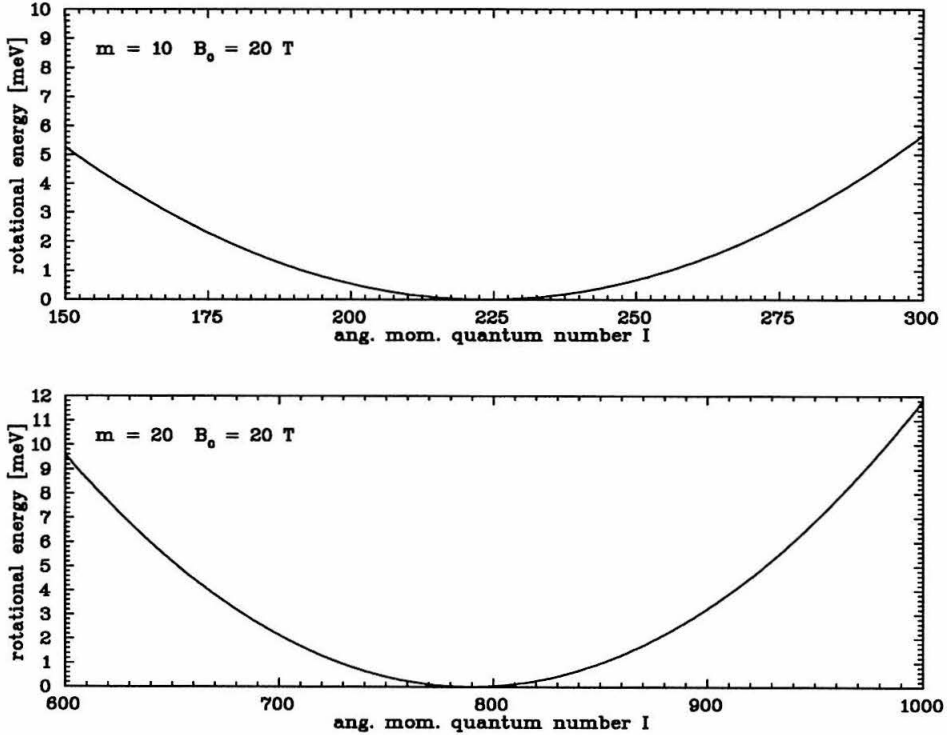
Figure 4.6: Rotational spectra for 10 electrons (upper diagram) and 20 electrons (lower diagram), when they have formed Wigner molecules at $B_0 = 20$ T, as a function of total angular momentum I.

$$h_0 = \langle \hat{H} \rangle - h_2 \langle \Delta \hat{J}^2 \rangle. \tag{4.22}$$

All expectation values in (4.22) can be calculated using Wick's theorem [12] and basic commutation relations.

Fig. 4.6 shows the rotational spectra for $m = 10$ and $m = 20$ electrons and $B = 20$ T as a function of the quantum number I, where I have subtracted the shifted ground state energy, which is obtained from the Hartree-Fock energy $\langle \hat{H} \rangle$ by subtracting the rotational energy $h_2 \langle \Delta \hat{J}^2 \rangle$, which is only of order 0.25 meV in both cases. This is the amount of energy by which the ground state energy is lowered because of the improvement of the wave function I have introduced by the projection.

The moments of inertia associated with these states are

$$J_Y = \frac{1}{2h_2} = 5.2 \times 10^5 \ \hbar^2/\text{eV} \tag{4.23}$$

for $m = 10$ and

$$J_Y = 1.9 \times 10^6 \ \hbar^2/\text{eV} \tag{4.24}$$

for $m = 20$.

In order to excite a molecule with circular polarized radiation, one has to produce photons of minimal energy of

$$\Delta E^{(10)}(I = 224) = E_{proj}^I(I = 224) - (\langle \hat{H} \rangle - h_2\langle \Delta \hat{J}^2 \rangle) = 1.12 \cdot 10^{-7} \ \text{eV} \tag{4.25}$$

for the 10 electron molecule and

$$\Delta E^{(20)}(I = 790) = 3.2 \cdot 10^{-8} \ \text{eV} \tag{4.26}$$

for 20 electrons. They are the energy differences between ground and first excited state. These energies correspond to radio frequencies of $\nu^{(10)} = 27.06$ MHz and $\nu^{(20)} = 7.73$ MHz. Note that the corresponding wavelengths are in the transparent region for GaAs. Therefore, the measurement of transmission coefficients of circular polarized radiation should give experimental evidence of Wigner molecules.

The level spacing, $\Delta E \approx \frac{\partial E_{proj}^I}{\partial I} \Delta I$, of the excited states then increases with higher states, resulting in excitations in the microwave region. The heat capacity connected with this rotational degree of freedom,

$$c = \frac{\partial <U>}{\partial T} = \frac{\partial}{\partial T} \frac{1}{Z} \left(\sum_I E_{proj}^I \exp\left(-\frac{E_{proj}^I}{k_B T}\right) \right), \tag{4.27}$$

where

$$Z = 1 + \sum_I \exp\left(-E_{proj}^I/k_B T\right) \tag{4.28}$$

is the partition function and k_B Boltzmann's constant, should therefore reach its
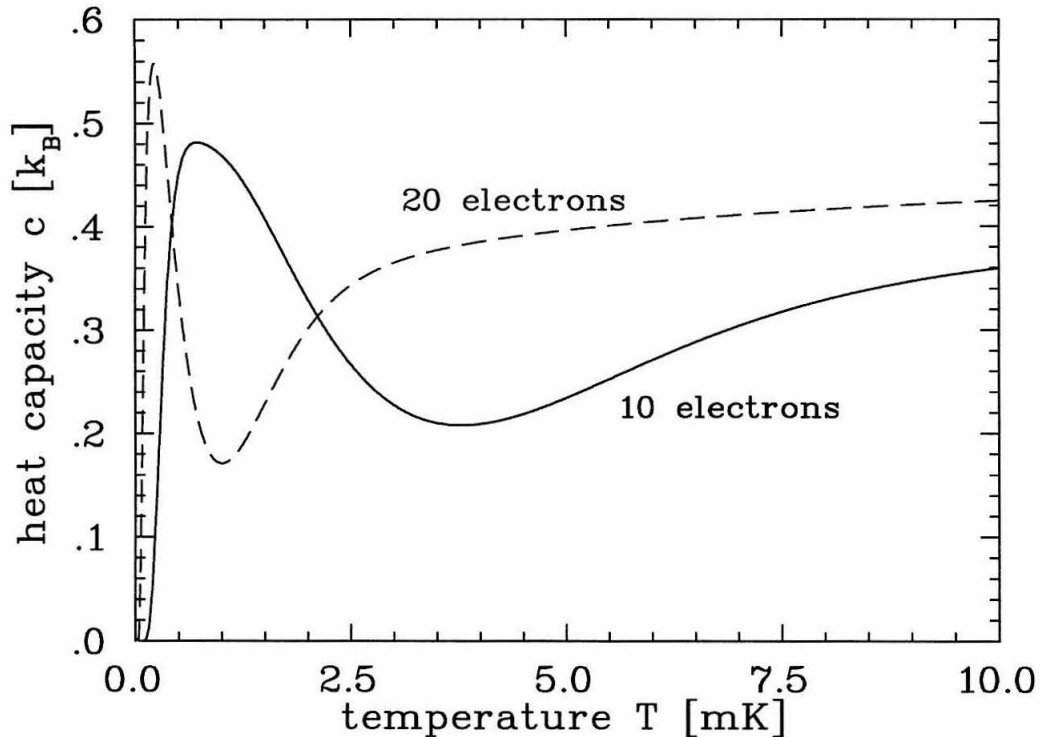
Figure 4.7: Heat capacity c arising from the rotational spectra of Fig. 4.6. The dashed line shows the 20 electron system, the solid one the 10 electron case.

classical value of $\frac{1}{2}k_B$ even for temperature as low as 1 K. Fig. 4.7 shows the well known Schottky anomaly of the heat capacity, typical for a system where only two states are of importance, at low temperatures of $\sim$ 1 mK: The heat capacity for a two-state system falls off like $\sim \frac{1}{T^2}$ for higher temperatures, while it approaches zero for $T \to 0$ [20]. Thus, there is a pronounced hump at intermediate temperature. As expected, it approaches $\frac{1}{2}k_B$ for high temperatures because the energy differences are very small. (1 K corresponds to 10^{-4} eV.) For the indicated temperature regime the heat capacity has converged within my model space, which consists of 400 rotational states, and shows the expected typical behaviour of a quantum mechanical rotor in a heatbath.

The energy levels of the vibrational modes of a single electron in the crystal can be estimated in a simplified one-dimensional model. Concerned only with the radial

degree of freedom, an outer electron (in the case of ten electrons) interacts with the external potential and the Coulomb potential of the two inner electrons, which I regard positioned at the center:

$$V(r) = \frac{1}{2} m^* \omega_0^2 r^2 + \frac{2e^2}{\epsilon r}. \tag{4.29}$$

Expanding the potential around the equilibrium position r_0 of the outer electron to second order, I obtain

$$V(r) = \frac{1}{2} m^* \left\{ \omega_0^2 + \frac{8e^2}{\epsilon m^* r_0^3} \right\} (r - r_0)^2 + \left\{ m^* \omega_0^2 r_0 - \frac{2e^2}{\epsilon r_0^2} \right\} (r - r_0) + \frac{1}{2} m^* \omega_0^2 r_0^2 + \frac{2e^2}{\epsilon r_0}. \tag{4.30}$$

The electron is confined by the parabolic part of this expansion with a corrected strength

$$\omega' = \sqrt{\omega_0^2 + \frac{8e^2}{\epsilon m^* r_0^3}}. \tag{4.31}$$

Setting $r_0 \approx 2 \times 10^{-6}$ cm, the energy levels for the vibrational modes of the electron are separated by

$$\Delta E_{vib} = \hbar \omega(B_0) = \sqrt{(\hbar \omega')^2 + \frac{1}{4}(\hbar \omega_c)^2} \approx 21 \text{ meV}, \tag{4.32}$$

much larger than the separation in the rotational energy levels

$$\Delta E_{rot} \approx 10^{-4} \text{ meV} \tag{4.33}$$

around $I = 225 \ \hbar$. Vibrational modes therefore contribute only marginally to the heat capacity and can be easily suppressed by proper excitation of the rotational modes only.

Chapter 5   Summary and Conclusion

I have shown in a full quantum mechanical treatment that there exist regimes where Wigner molecules and crystals are the ground states of quantum dots. I have also described rotational spectra of quantum dots, which arise from the existence of deformed Hartree-Fock solutions. This broken symmetry could make it possible to detect Wigner molecules experimentally by exciting the rotational excited states of the system.

Much more can be done in this area of quantum dot Physics: Hartree-Fock in general is only valid if the number of particles is not too small, because the correlation energies then should not dominate. An investigation how these two-body correlations neglected in the Hartree-Fock approximation influence the system of a few electrons would be useful. In the past there have been some direct diagonalization calculations for $m < 5$ electrons, but they were only concerned about investigations on magic numbers and shell structure (in energy, not space) arising from the occupation of Fock-Darwin levels.

In the other limit of high numbers of electrons, open questions remain too: It is not obvious a crystalline structure does prevail for any number of particles: At the outer regions the particles feel a stronger and stronger external potential exerting such a pressure that it "squeezes" the outer electrons more and more. In this way they would be forced back to occupy Fock-Darwin levels: the crystal would "liquify" under the pressure. So one could imagine that both phases, a continuously rotational symmetric phase outside and a Wigner crystal phase inside, coexist in the same dot. Unfortunately, I was not able to prove this in another Hartree-Fock calculation because I ran out of memory (I was using a DEC alpha workstation at that time). It would certainly be an interesting project.

So far no experimental effort has been made to detect Wigner crystals (to my knowledge), but it has been recognized that the appearance of the additional de-

gree of freedom described in the previous chapter is interesting [21]. It could lead to their detection. The research on the subject of quantum dots is very broad and diverse, with many interesting effects observed experimentally or theoretically predicted. The variety stems from the fact that many different experimental conditions can be achieved easily today, and technology is improving steadily. Therefore, I am confident that Wigner molecules will be detected in the not-so-far future.

In general, it would be desirable to investigate quantum dots with exact methods, because Hartree-Fock has its limitation as mentioned throughout the last sections. But a direct diagonalization scheme or Monte Carlo calculation are difficult to implement. The direct diagonalization gets out of hand (in memory and cycles) quite fast with number of particles, while a Monte Carlo procedure, in principle exact, suffers from the famous sign problem caused by the fermion nature of the problem and the repulsive feature of the Coulomb interaction. The calculation mentioned earlier fix the nodal structure of the wave function and are therefore not exact. In the second part of this thesis I will investigate another system of interacting fermions, and some of the problems connected with the sign problem will be explained in more detail.

Part II

Nuclear Matter on a Lattice

Chapter 6   Review of Nuclear Matter

One purpose of studying infinite nuclear matter is the determination of binding energies and saturation densities *ab initio* from a nuclear potential that describes the elastic scattering of free nucleons. Properties of nuclei are strongly influenced by finite size effects like the surface effect, and it is therefore difficult to calculate binding energies and saturation densities of nuclear matter from nuclei. The semi-empirical mass formula [25, 26] for nuclei of mass A,

$$E_B\left(Z, N\right) = \alpha_1 A - \alpha_2 A^{2/3} - \alpha_3 \frac{Z\left(Z-1\right)}{A^{1/3}} - \alpha_4 \frac{\left(N-Z\right)^2}{A} + \Delta, \qquad (6.1)$$

takes into account a volume term ($\alpha_1 = 16$ MeV), the surface effect ($\alpha_2 = 17$ MeV) and the Coloumb repulsion of the Z protons ($\alpha_3 = 0.6$ MeV). Furthermore, a symmetry energy contribution ($\alpha_4 = 25$ MeV) takes care of the observation that nuclei with an equal number of N neutrons and Z protons are more deeply bound, and the pairing term ($\Delta \approx \frac{12}{\sqrt{A}}$ MeV for an even-even nucleus, $\Delta \approx -\frac{12}{\sqrt{A}}$ MeV for an odd-odd nucleus and 0 MeV otherwise, where the terms "even" and "odd" refer to the number of protons and neutrons in the nucleus, respectively) accounts for the pairing force, making even-even nuclei more tightly bound. The volume term of this formula gives an estimate for the binding energy of infinite symmetric matter $E/A = 16$ MeV. The coefficient is basically obtained from a fit of binding energies of a large number of nuclei. The empirical determination of saturation densities stems from an extrapolation to the central region of finite nuclei and is therefore subject to uncertainties too.

So far, calculations of nuclear matter have had difficulties to predict saturation densities and binding energies that are compatible with those values obtained from finite nuclei. None of the existing nuclear potentials reproduces these quantities correctly. Plotting a diagram of equilibrium energies versus densities for different calculations (see, for example, Fig. 1 of reference [27]) gives the so called Coester line

which describes the fact that all calculations either predict the correct equilibrium density, but underestimates the binding energy, or, if the binding energy is correct, they overestimate the density. The location of a calculation on the Coester line turns out to mainly be determined by the strength of the tensor force. It seems unlikely that NN potentials like Paris, Bonn, Reid, Argonne or Urbana are deficient since they represent the best theoretical understanding of the interaction currently available. The only improvements of these mesonic-based two-body potentials that could be made are at short distances at which they should be replaced by models that account for the composite nature of the nucleon.

If the two-body potential cannot be held accountable for the insufficient description of nuclear matter, the deficiency could lie in the lack of three-body and higher order forces or the treatment of the many-body problem. Two major approaches have been tried in the past to address the latter one: The Bethe-Brueckner-Goldstone (BBG) [22, 23, 24] theory, and variational methods which are used in connection with the hypernetted chain approximation (HNC) [28, 29]. The Bethe-Brueckner-Goldstone theory in lowest order considers repeated scattering of pairs of particles in the nuclear medium. The effects of the nuclear medium are restricted to a dispersion relation and the Pauli principle. The latter prohibits the scattering of particles into occupied states, and the dispersion relation accounts for the fact that each nucleon is bound in the medium, thereby shifting its energy from the free space value. In a variational approach the trial wave function is a product of two-body correlation functions and a Slater determinant of plane waves of noninteracting particles. The calculation and minimization of the energy is performed by using the HNC formalism and two-body distribution functions. The variational approach, which incorporates long range correlations, can be used for the high-density regime, at which the BBG theory fails. If HNC is used, however, it does not obey a variational principle, unless Euler-Lagrange equations are applied, and therefore does not give an upper bound in energy. Another disadvantage is the fact that correlation factors for each pair are the same regardless of spin and isospin quantum numbers. Finally, a tensor force, a necessary ingredient of the nuclear potential, cannot easily be included in a variational

approach.

Despite the shortcomings of both approaches, BBG and HNC give results that agree and lie on the Coester line. Therefore, the last possibility on improving the potential is a genuine many-body force. Long-ranged three-body forces give density dependent two-body forces when integrated over one of the nucleon lines that results in terms proportional to $(\sigma_1 \cdot \sigma_2)(\tau_1 \cdot \tau_2)$ and $S_{12}(\tau_1 \cdot \tau_2)$ in the potential, S_{12} being the tensor operator. Combinations of forces, like a three-body force followed by a one-pion exchange, generate operators of the form $S_{12}^2(\tau_1 \cdot \tau_2)^2$. These kind of terms could be used as a new ingredient to accommodate a Hamiltonian that reproduces energies and densities correctly.

Wiringa et al. [28] and Akmal and Pandharipande [29] have calculated ground state properties of symmetric nuclear matter (SNM) and pure neutron matter (PNM) with the most complete interaction that is available today. Wiringa et al. use the Argonne V_{14} (AV14) and Urbana V_{14} (UV14) two-nucleon potentials which have the same structure, but they significantly differ in the strength of the short range tensor force. Both potentials are constrained by NN scattering data. They consist of a long-range one-pion exchange, an intermediate-range part that simulates two-pion exchanges and a short-range part which substitutes for the physics of a heavy meson exchange or the overlap of the composite quark system.

These two two-body potentials are then being used in connection with the Urbana VII three-nucleon potential and a three-nucleon interaction model (TNI) which turns out to be a density dependent modification of the Urbana UV14 potential. The UVII three-nucleon potential is a combination of a long-range two-pion exchange and an intermediate-range repulsive force. The first part is attractive and dominates at low densities, while the repulsive part helps ensure that saturation is reached properly at high densities. The density dependent UV14 potential is built by multiplying terms of the two-body UV14 potential by exponential factors, $\exp(\gamma\rho)$, γ being a strength factor and ρ being the particle density. Density-dependent terms are considered to be a result of a genuine three-body force where the third nucleon has been integrated out. The exponential even includes higher order interactions, and the linear term of

its expansion represents the three-body part.

Their many-body calculation is a variational approach in connection with the hypernetted chain approximation (HNC), that is used to calculate expectation values of the full Hamiltonian,

$$E_v = \frac{\langle \psi_v | H | \psi_v \rangle}{\langle \psi_v | \psi_v \rangle}, \tag{6.2}$$

$|\psi_v\rangle$ being the trial wave function containing some variational parameters. They find that the lowest order diagrams in the HNC scheme are already sufficient to calculate the energy for normal saturation densities, but they are concerned about their accuracy with respect to spin, isospin and tensor correlations because HNC, as mentioned earlier, does treat all two-body correlations equally. This also applies to spin-orbit correlations.

Their observations can be summarized as follows: While three-body correlations in the wave function matter only slightly in the case of nuclear matter, they are of significant importance for neutron matter, which they attribute to the tensor correlation introduced by the two-pion exchange of the three-body force. In the case of nuclear matter, a big contribution comes from the isospin-singlet channel of the two-body tensor potential, while the corresponding triplet channel is weak in neutron matter. Thus, the tensor force is emphasized in the three-body force. The variational results show that the two-body potential alone tends to underbind light nuclei while saturating nuclear matter at too high densities. They adjust the three-body potential to improve the nuclear matter properties as shown in Figs. 4 and 5 of their paper. (Recently, though [30], the suggestion has been made that the tensor force does not play an important role in the saturation process, but rather relativistic corrections.) The adjustment of the three-body force gives an improved saturation density, and therefore a stiffer equation of state. For lower density, the agreements with other calculations [31] are good. The calculation with the UV14 and TNI potential gives more deeply bound matter. By looking at kinks in energy curves and rapid changes in expectation values of the one- and two-pion exchange interactions, a pion condensate is identified in neutron matter at $\rho = 0.2 \ \text{fm}^{-3}$. Wiringa also calculates the equation

of state for neutron matter and the first sound velocity which violates causality at $\rho = 1$ fm^{-3}. The effects of a three-body force are twofold: The repulsive short-range part guarantees a stiffer equation of state for higher densities, and the long-range two-pion exchange introduces a neutral pion condensate for neutron matter and was considered a major improvement to previous work [31].

Akmal and Pandharipande [29] used an improved Argonne potential V_{18} (AV18) [32] that includes isospin symmetry breaking terms. They use the same methods as in Ref. [28] (with a slight improvement that addresses a momentum dependence of the interaction). The energies in the nuclear matter case are higher than in Wiringa's calculation (at higher densities), but they attribute this to a different three-body force (UIX) used. The minimum energy per particle for SNM is -12 MeV, and they estimate that deficiencies in the model of nuclear forces accounts for less than approximately 2 MeV in underbinding. They speculate that three-body correlations in the wave function could lower the variational bound on the energy by more than 1 MeV. They predict that for the potential AV18 and UIX, symmetric nuclear matter and pure neutron matter will undergo a phase transition with a pion condensate (cf. Ref. [28]) at $\rho = 0.32$ fm^{-3} and $\rho = 0.2$ fm^{-3}, respectively, which is sensitive to the $\vec{\sigma} \cdot \vec{\sigma}$ and $(\vec{\sigma} \cdot \vec{\sigma})(\vec{\tau} \cdot \vec{\tau})$ interaction part. This transition does not occur with the old UV and AV potential in SNM, but only in PNM, as mentioned above.

This concludes the summary on calculations of ground state properties of nuclear matter with accurate Hamiltonians, and I now turn to thermal calculations on lattices.

Nuclear matter exhibits a quark deconfinement phase transition at high temperatures ($T \approx 200$ MeV) and high densities ($\rho \approx \rho_0$). At low temperature ($T \approx 15 - 20$ MeV) a liquid-gas phase transition is expected to take place. For this transition, Hartree-Fock [33, 34], real time Green's function [35, 36] and ring-diagram methods have been tried [37]. Several lattice calculations have been attempted to describe the thermal properties of nuclear matter, concentrating on phase transitions.

Kuo et al. [38] studied a cubic lattice gas model for nuclear matter where each lattice site can be either occupied by one proton or one neutron, or it can remain

unoccupied. They implement nearest-neighbor interaction of the form

$$V = - \sum_{<ij>} J_{ij} \tau_{zi} \tau_{zj}, \qquad (6.3)$$

which is an isospin-1-Ising model, and argue that this is an effective interaction after terms proportional to 1, $\vec{\sigma} \cdot \vec{\sigma}$, $\vec{\tau} \cdot \vec{\tau}$ and $\vec{\sigma} \cdot \vec{\sigma} \vec{\tau} \cdot \vec{\tau}$ have been averaged over spin and spatial variables. Also, they include a kinetic term which turns out to be crucial for the existence of a phase transition (the same model without kinetic energy term does not exhibit such a behaviour), and use the Bragg-Williams mean field approximation to show the existence of a dense (liquid-like) phase and a rare (gas-like) phase. This approximation replaces the number of nearest-neighbor pairs, N_{ii}, of one kind (protons $(i = +)$, neutrons $(i = -)$ or vacancies $(i = 0)$) with their independent particle value N_i,

$$\frac{N_i^2}{N^2} = \frac{N_{ii}^2}{3N}, \; i = \{+, -, 0\}, \qquad (6.4)$$

while two Lagrangian parameters fix the density ρ and asymmetry $N_+ - N_-$.

Their ρ-T and p-V diagram show a liquid and a gas phase as well as a coexistence region of gas and liquid below a critical temperature $T_c = 18.4$ MeV, similar to those present in an atomic van der Waals theory. Since their calculation is just a mean field approximation, they speculate in the concluding remark how a Monte Carlo simulation would change the phase boundaries.

Campi and Krivine [39] investigate clustering of nucleons in a finite piece of matter at temperatures and densities that are above the liquid-gas critical point. They consider a three-dimensional cubic lattice with N sites that are either empty or occupied with one particle. Particles occupying nearest-neighbor sites interact with an energy $-\epsilon$:

$$H = \sum_i^N n_i \frac{p^2}{2m} - \epsilon \sum_{<ij>} n_i n_j, \; A = \sum_i^N n_i, \qquad (6.5)$$

where $n_i = 0, 1$ are the site occupation numbers. It is a simplification of the usual two-body Hamiltonian, $H = \sum_i^A \frac{p^2}{2m} + \sum_{<ij>} v(r_{ij})$, discretizing positions of the particles and assuming a contact interaction for $v(r_{ij})$. For this case, the grand canonical par-

tition function is proportional to the canonical partition function of the Ising model, where the spin-down electron corresponds to an occupied site, and the spin-up electron to an empty site of their model. The external magnetic field accounts for the conservation of the number of particles (on average), and the density is linked to the relative magnetization of the Ising model. The lattice gas model is then solved numerically in the grand canonical ensemble by moving particles on the lattice according to a Monte Carlo method until thermal equilibrium is reached. They too find three phases: A gas, a liquid and mixture of both. For an infinite system, thermodynamical quantities like heat capacities, isothermal compressibilities and density differences exhibit a critical behaviour that is proportional to $|T - T_c|^\mu$ (for a second order phase transition), where the exponent μ is that of the Ising model. Critical exponents are universal and do not depend on a specific interaction nor on the existence of a lattice, but only on spatial dimension. Therefore, the result should not depend on the use of a lattice. They find that a full line of points exists in the T-ρ diagram on which the mass distribution of stable droplets is a power law, $p(A) \sim A^{-\tau}$, $\tau \approx 2.2$. This is in contrast with the common belief that the power law behaviour is characteristic of a single critical point and could therefore point to a pathology of the lattice-gas model.

Pan and Das Gupta also have investigated a lattice gas model [40, 41, 42], and recently included an isospin dependent interaction [43]. Similar to Ref. [39], they put single particles on sites of a cubic lattice and let them interact with their nearest neighbor via an isospin dependent strength, ϵ_{pp}, ϵ_{pn}, ϵ_{nn}. Their calculation is classical, sampling the momentum of the particles from a Maxwell-Boltzmann distribution. First, they apply the Bragg-Williams conditions to show that for this mean field approximation the isospin-independent model ($\epsilon_{pp} = \epsilon_{pn} = \epsilon_{nn} = -5.3$ MeV) does not predict the same value for the energy as for the isospin-dependent case ($\epsilon_{pp} = \epsilon_{nn} = 0$). The mean field proves not to be capable of accounting for isospin-specific occupation configurations that would result in the same energy $E/A = -16$ MeV. Also, the determination of the critical temperature is dramatically wrong, if compared to their Monte Carlo like simulation, which shows that the isospin-dependent and independent model give quite similar values for the critical temperatures, while in the mean field

case their values differ by a factor 1/2.

Having summarized results on nuclear matter available in literature so far, I now move on to describe the aims for this project.

Chapter 7   Concepts and Motivation for a Lattice Calculation

As it became clear in Chapter 6, calculations for nuclear matter either restrict themselves to description of ground state properties and are based on a fairly good Hamiltonian, or they attempt simulations for finite temperatures to capture the liquid-gas transition that is expected to occur at $T \approx 15 - 20$ MeV. In the latter case people work with a much cruder Hamiltonian. Both approaches share the deficiency that they are not exact: BBG and the variational attempts are based on low-order ladder or cluster approximation, and the variational analysis does not even give an upper bound. Both also fail to predict observational evidence that is now known for 50 years and are summarized by the Bethe-Weizsäcker or semi-empirical mass formula.

The lattice calculations that aim at a thermal description of nuclear matter are classical, not quantum mechanical, putting in kinetic terms by hand or sampling them from a Maxwell-Boltzmann distribution. On the other hand, these types of calculations show already that the inclusion of a kinetic term is crucial to observe a phase transition. Thus, a full quantum mechanical and exact treatment with the full Hamiltonian, kinetic and potential term, should be a prerequisite for a successful description of the physical system.

Combining both features, the usage of a realistic Hamiltonian that is based on experimental data and an exact, thermal treatment of the many-body problem has been impossible so far; the advent of more computer power has only now made it possible to describe the simplest and smallest lattice systems in recent years. In condensed matter Physics, the Hubbard model (aimed at understanding superconductivity) has been studied extensively, but the model Hamiltonian used and the lattice sizes implemented are still comparatively small: two-dimensional lattices of a few tens of sites and with a simple nearest-neighbor interaction have been investigated. Nevertheless,

these simple *quantum* Monte Carlo methods were able to give important insight about magnetic properties of electrons and their particle correlations.

In the last few years the shell model Monte Carlo (SMMC) method has been successfully developed [44, 45, 46, 47, 48] to give a powerful alternative to direct diagonalization procedures which suffer from the fact that the many-body space scales so unfavorably with the number of single-body states considered. Direct diagonalization methods can only address very light nuclei or nuclei with a closed shell and only a few valence nucleons. The SMMC avoids this combinatorial scaling (in storage and computation time) and makes it possible to investigate structural properties of nuclei far beyond the few-nucleon system. The SMMC enforces the Pauli-principle exactly, but concentrates on the evaluation of thermal averages of observables only: no wave function of a specific state is obtained. This is the only drawback of the method. As a consequence, it is impossible to obtain spectroscopic information, but contrary to the SMMC this would not be the main interest of a nuclear matter investigation anyway. While in SMMC one extrapolates to lowest possible temperatures to gain information on the ground state only, the thermal formalism is most welcome for a study of nuclear matter: here, the equation of state is of main interest, which clearly depends on density and temperature. It is a further purpose to consider a large piece of infinite nuclear matter in *coordinate* space to get rid of finite size effects that appear after imposing periodic boundary conditions. A formalism written in momentum space has the disadvantage that two- or many-body correlations cannot be calculated comfortably: Clustering (and therefore a possible liquid-gas transition) is not as easily calculated and observed as in the coordinate space representation.

In summary, the following concept should be pursued for a nuclear matter calculation: In a coordinate representation nucleons shall interact with a potential that comes as close to a realistic NN interaction (like AV18) as possible. The partition function along with observables of interest shall be calculated in the grand canonical ensemble, in order to control temperature T and density ρ. The latter is to be adjusted on average via the chemical potential μ. The many-body problem shall be solved exactly using Monte Carlo methods similar to those used in the SMMC appli-

cations. At the same time, realizing that the emerging equations eventually have to be solved on a computer, one should take into account that space will be discretized, and advantage should be taken of the available technology that has been employed for the Hubbard and other models in condensed matter Physics.

Chapter 8 Theory of Nucleonic Matter on a Lattice

The general concept of the nuclear matter calculation consists of nucleons interacting via a variety of components of the nuclear two-body potential. While it should be the ultimate goal to use a potential that fits the nucleon-nucleon scattering data best [32], at the first stage I concentrate on very few parts of the interactions, namely the central, spin and isospin exchange one. The degrees of freedom of the nucleon are its spin, isospin as well as the spatial coordinate.

Subnuclear degrees of freedom are not explicitly incorporated. The lightest meson, the pion, facilitates an interaction with a range of $r = 1.4$ fm which happens to be of same order as the lattice spacing of the first applications, symmetric nuclear matter. For this case, however, the one-pion exchange force of the nuclear potential averages out, because the potential (for example for AV14) only contains terms which contain the isospin operator. The force is then mediated by mesons that have higher mass, like the ω or σ. Since the system is ultimately regularized on a lattice, the argument can be made that all subnuclear degrees of freedom are integrated out, resulting in a strong on-site and weaker next-neighbor interaction, if a lattice spacing of $a = 1.842$ fm is assumed. This particular lattice spacing sets the half-filling of the lattice at $\rho = 2\rho_0 = 0.32$ fm^{-3}.

However, at saturation density $\rho = \rho_0 \approx 0.16$ fm^{-3}, the Fermi momentum corresponds to $p_F c = \hbar k_F c \approx 260$ MeV and should be compared to the vacuum nucleon mass $m_N c^2 = 939$ MeV. The expansion of the Fermi kinetic energy,

$$m_N c^2 \left(\sqrt{1 - \frac{v_F^2}{c^2}} - 1 \right) = \frac{1}{2} m_N v_F^2 + \frac{3}{8} m_N c^2 \frac{v_F^4}{c^4} + \cdots, \tag{8.1}$$

gives a correction of $\Delta \frac{E}{A} \approx 2$ MeV, which is small, but not insignificant if compared

to the saturation binding energy $E/A \approx 16$ MeV.

In this chapter, I specify the Hamiltonian of the system and describe the nuclear matter Monte Carlo method (called NMMC hereafter), which consists of the thermal formalism to express the grand canonical partition function as an integral over single-body evolution operators. At its center stands the Hubbard-Stratonovitch transformation, and it is used to reduce the many-body problem to an effective one-body problem. The details of the Monte Carlo procedure, which is used to evaluate the resulting multi-dimensional integral, are explained. Finally, a description how to obtain potential parameters from scattering length and effective range is attempted.

8.1 Hamiltonian of the System

I consider a three-dimensional cubic lattice of spacing a and assume periodic boundary conditions, which result in a three-dimensional toroidal configuration. The coordinate $\vec{x}$ and the momentum $\vec{p}$ are discretized as

$$\vec{x} \rightarrow a\vec{m} \equiv \vec{x}_m, \; m \text{ integer}, \tag{8.2}$$

$$\vec{p} \rightarrow \left(\frac{2\pi}{Na}\right) \vec{k} \equiv \vec{p}_k, \; k \text{ integer}, \tag{8.3}$$

so that

$$\vec{x} \cdot \vec{p} = \frac{2\pi}{N} \times \text{integer}, \tag{8.4}$$

where N is the number of lattice points in each spatial direction.

The nucleons have mass m_N, spin $\sigma = \pm\frac{1}{2}$ and isospin $\tau = \pm\frac{1}{2}$. The Hamiltonian,

$$\hat{\mathcal{H}} = \hat{\mathcal{K}} + \hat{\mathcal{V}}, \tag{8.5}$$

is expressed in second quantization and contains kinetic and potential operators. The first term is written as

$$\hat{\mathcal{K}} = -\frac{\hbar^2}{2m_N} \sum_{\sigma\tau} \int \mathrm{d}\vec{x} \; \psi_{\sigma\tau}^\dagger(\vec{x}) \vec{\nabla}^2 \psi_{\sigma\tau}(\vec{x}). \tag{8.6}$$

The fermion operator $\psi_{\sigma\tau}^{\dagger}(\vec{x})$ creates a nucleon of spin and isospin (σ, τ) at location $\vec{x}$, while its adjoint $\psi_{\sigma\tau}(\vec{x})$ destroys it. This equation is discretized on the lattice by the symmetric 3-point formula for the second derivative, and the integral is replaced by a finite sum:

$$a^2 \frac{\partial^2}{\partial x^2} \psi(x) + \mathcal{O}\left(a^4\right) \ \rightarrow \ \psi(x+a) - 2\psi(x) + \psi(x-a) \tag{8.7}$$

$$\int \mathrm{d}\vec{x} \ \rightarrow \ \sum_{\vec{x}_n} a^3. \tag{8.8}$$

This results in

$$\hat{\mathcal{K}} = -t_0 \sum_{\sigma\tau} a^3 \sum_{\vec{x}_n, i=1\cdots 3} \psi_{\sigma\tau}^{\dagger}(\vec{x}_n) \left[\psi_{\sigma\tau}(\vec{x}_n + a\vec{e}_i) - 2\psi_{\sigma\tau}(\vec{x}_n) + \psi_{\sigma\tau}(\vec{x}_n - a\vec{e}_i)\right] \tag{8.9}$$

with

$$t_0 = \frac{\hbar^2}{2m_N a^2}, \tag{8.10}$$

and the orthogonal unit vectors $\{\vec{e}_i\}$ span the three-dimensional space.

The general ansatz for the potential,

$$\hat{\mathcal{V}} = \frac{1}{2} \sum_{\sigma\tau\sigma'\tau'} \int \mathrm{d}\vec{x} \int \mathrm{d}\vec{x}' \ \psi_{\sigma\tau}^{\dagger}(\vec{x})\psi_{\sigma'\tau'}^{\dagger}(\vec{x}')V(\vec{x} - \vec{x}')\psi_{\sigma'\tau'}(\vec{x}')\psi_{\sigma\tau}(\vec{x}), \tag{8.11}$$

can be written in terms of the density

$$\hat{\rho}(\vec{x}) = \sum_{\sigma\tau} \hat{\rho}_{\sigma\tau}(\vec{x}) = \sum_{\sigma\tau} \psi_{\sigma\tau}^{\dagger}(\vec{x})\psi_{\sigma\tau}(\vec{x}). \tag{8.12}$$

The purpose of doing so is to cast the potential in linear and quadratic terms, as the Hubbard-Stratonovitch transformation can only be performed on quadratic terms. Using the fermion anticommutation relation,

$$\begin{aligned}
\psi_{\sigma\tau}^{\dagger}(\vec{x})\psi_{\sigma'\tau'}^{\dagger}(\vec{x}')\psi_{\sigma'\tau'}(\vec{x}')\psi_{\sigma\tau}(\vec{x}) = \ &- \ \psi_{\sigma\tau}^{\dagger}(\vec{x}) \left\{ \delta_{(\sigma\tau),(\sigma'\tau')}\delta(\vec{x} - \vec{x}') \right. \\
&- \ \left. \psi_{\sigma\tau}(\vec{x})\psi_{\sigma'\tau'}^{\dagger}(\vec{x}') \right\} \psi_{\sigma'\tau'}(\vec{x}'),
\end{aligned} \tag{8.13}$$

the potential then becomes

$$\hat{\mathcal{V}} = \frac{1}{2} \int d\vec{x} \int d\vec{x}' \, V(\vec{x} - \vec{x}') \hat{\rho}(\vec{x}) \hat{\rho}(\vec{x}') - \frac{1}{2} \int d\vec{x} \, V(0) \hat{\rho}(\vec{x}). \qquad (8.14)$$

The last term is the self-energy and is a consequence of the Pauli principle. It could also be viewed as an additional chemical potential. The discretized version of this equation is

$$\hat{\mathcal{V}} = \frac{a^6}{2} \sum_{\vec{x}_n, \vec{x}'_n} V(\vec{x}_n - \vec{x}'_n) \hat{\rho}(\vec{x}_n) \hat{\rho}(\vec{x}'_n) - \frac{a^3}{2} \sum_{\vec{x}_n} V(0) \hat{\rho}(\vec{x}_n). \qquad (8.15)$$

The choice of the potential parts is somewhat arbitrary and partly determined by computational issues that are discussed in later sections. It is

$$\hat{\mathcal{V}} = \hat{\mathcal{V}}_c + \hat{\mathcal{V}}_\sigma + \hat{\mathcal{V}}_\tau. \qquad (8.16)$$

The first part is the central potential ($\hat{\mathcal{V}}_c$), followed by the spin-exchange ($\hat{\mathcal{V}}_\sigma$) and isospin-exchange ($\hat{\mathcal{V}}_\tau$) potential. I assume a Skyrme-like on-site and next-neighbor interaction

$$V_c \left(\vec{x}_n - \vec{x}'_n \right) = V_c^{(0)} \delta \left(\vec{x}_n - \vec{x}'_n \right) + V_c^{(2)} \left(\nabla^2_{\vec{x}_n} \delta \left(\vec{x}_n - \vec{x}'_n \right) \right), \qquad (8.17)$$

whose discretized form is

$$V_c(\vec{x}_n - \vec{x}'_n) = \frac{V_c^{(0)}}{a^3} \delta_{\vec{x}_n, \vec{x}'_n} + \frac{V_c^{(2)}}{a^5} \sum_{i=1}^{3} \left\{ \delta_{\vec{x}_n + a\vec{e}_i, \vec{x}'_n} - 2\delta_{\vec{x}_n, \vec{x}'_n} + \delta_{\vec{x}_n - a\vec{e}_i, \vec{x}'_n} \right\}. \qquad (8.18)$$

Note that in this form $\frac{V_c^{(0)}}{a^3}$ and $\frac{V_c^{(2)}}{a^5}$ have the units MeV. The parantheses in Eq. (8.17) indicate that the Laplace operator only acts on the δ-function, but not on any following parts. Inserting Eq. (8.18) into (8.15) gives

$$\hat{\mathcal{V}}_c = \frac{V_c^{(0)}}{2a^3} \sum_{\vec{x}_n} a^6 \hat{\rho}(\vec{x}_n)^2 \quad - \quad \frac{V_c^{(2)}}{2a^5} \sum_{\vec{x}_n} a^6 \sum_{i=1}^{3} \left(\hat{\rho}\left(\vec{x}_n + a\vec{e}_i\right) - \hat{\rho}\left(\vec{x}_n\right) \right)^2$$

$$- \quad \frac{1}{2} \left(\frac{V_c^{(0)}}{a^3} - 6\frac{V_c^{(2)}}{a^5} \right) \sum_{\vec{x}_n} a^3 \hat{\rho}(\vec{x}_n), \tag{8.19}$$

indicating that $(a^3 \hat{\rho})$ is a dimensionless quantity. I again applied periodic boundary conditions:

$$\sum_{\vec{x}_n, i} (\hat{\rho}(\vec{x}_n) - \hat{\rho}(\vec{x}_n - a\vec{e}_i))^2 = \sum_{\vec{x}_n, i} \hat{\rho}(\vec{x}_n)^2 + \sum_{\vec{x}_n, i} \hat{\rho}(\vec{x}_n - a\vec{e}_i)^2 - 2 \sum_{\vec{x}_n, i} \hat{\rho}(\vec{x}_n)\hat{\rho}(\vec{x}_n - a\vec{e}_i) \tag{8.20}$$

and

$$\sum_{\vec{x}_n, i} \hat{\rho}(\vec{x}_n - a\vec{e}_i)^2 = \sum_{\vec{x}_n, i} \hat{\rho}(\vec{x}_n)^2 \tag{8.21}$$

as well as

$$\sum_{\vec{x}_n, i} \hat{\rho}(\vec{x}_n)\hat{\rho}(\vec{x}_n - a\vec{e}_i) = \sum_{\vec{x}_n, i} \hat{\rho}(\vec{x}_n)\hat{\rho}(\vec{x}_n + a\vec{e}_i). \tag{8.22}$$

The spin- and isospin-exchange parts of the potential are handled in a very similar way. Starting from

$$\hat{\mathcal{V}}_\sigma = \frac{1}{2} \sum_{\substack{\sigma\tau\sigma'\tau' \\ \kappa\lambda\kappa'\lambda'}} \int d\vec{x} \int d\vec{x}' \ \psi_{\sigma\tau}^\dagger(\vec{x})\psi_{\sigma'\tau'}^\dagger(\vec{x}') V_\sigma(\vec{x} - \vec{x}') \vec{\sigma}_{\sigma\tau\kappa\lambda} \cdot \vec{\sigma}_{\sigma'\tau'\kappa'\lambda'} \psi_{\kappa'\lambda'}(\vec{x}')\psi_{\kappa\lambda}(\vec{x}),$$

$$\tag{8.23}$$

I use the identity

$$\begin{aligned} \vec{\sigma} \cdot \vec{\sigma}' &= \sigma^{(0)} \ \sigma'^{(0)} + 2 \left(\sigma^{(+)} \ \sigma'^{(-)} + \sigma^{(-)} \ \sigma'^{(+)} \right) \\ &= \sigma^{(0)} \ \sigma'^{(0)} + \left(\sigma^{(+)} + \sigma'^{(-)} \right)^2 + \left(\sigma^{(-)} + \sigma'^{(+)} \right)^2 \end{aligned} \tag{8.24}$$

to rewrite (8.23) in form of spin densities

$$\hat{\rho}_\sigma^{(\alpha)}(\vec{x}) = \sum_{\sigma\tau\kappa\lambda} \psi_{\sigma\tau}^\dagger(\vec{x})\sigma_{\sigma\tau\kappa\lambda}^{(\alpha)}\psi_{\kappa\lambda}(\vec{x}), \ \alpha = 0, +, -. \tag{8.25}$$

Eq. (8.24) holds because $(\sigma^{(+)})^2$ and $(\sigma^{(-)})^2$ are zero. $\sigma^{(\alpha)}_{\sigma\tau\kappa\lambda}$ are the elements of a generalized Pauli spin-isospin matrix:

$$\sigma^{(0)} = \begin{array}{c} \\ \text{p}\uparrow \\ \text{p}\downarrow \\ \text{n}\uparrow \\ \text{n}\downarrow \end{array} \begin{array}{cccc} \text{p}\uparrow & \text{p}\downarrow & \text{n}\uparrow & \text{n}\downarrow \\ \left(\begin{array}{cccc} 1 & 0 & 0 & 0 \\ 0 & -1 & 0 & 0 \\ 0 & 0 & 1 & 0 \\ 0 & 0 & 0 & -1 \end{array} \right) \end{array} \tag{8.26}$$

$$\sigma^{(+)} = \begin{array}{c} \\ \text{p}\uparrow \\ \text{p}\downarrow \\ \text{n}\uparrow \\ \text{n}\downarrow \end{array} \begin{array}{cccc} \text{p}\uparrow & \text{p}\downarrow & \text{n}\uparrow & \text{n}\downarrow \\ \left(\begin{array}{cccc} 0 & 1 & 0 & 0 \\ 0 & 0 & 0 & 0 \\ 0 & 0 & 0 & 1 \\ 0 & 0 & 0 & 0 \end{array} \right) \end{array} \tag{8.27}$$

$$\sigma^{(-)} = \begin{array}{c} \\ \text{p}\uparrow \\ \text{p}\downarrow \\ \text{n}\uparrow \\ \text{n}\downarrow \end{array} \begin{array}{cccc} \text{p}\uparrow & \text{p}\downarrow & \text{n}\uparrow & \text{n}\downarrow \\ \left(\begin{array}{cccc} 0 & 0 & 0 & 0 \\ 1 & 0 & 0 & 0 \\ 0 & 0 & 0 & 0 \\ 0 & 0 & 1 & 0 \end{array} \right) \end{array} . \tag{8.28}$$

Using (8.13), the discretized version then becomes

$$
\begin{aligned}
\hat{\mathcal{V}}_\sigma &= \frac{a^6}{2} \sum_{\vec{x}_n \vec{x}'_n} \sum_{\substack{\sigma\tau\sigma'\tau' \\ \kappa\lambda\kappa'\lambda'}} \psi^\dagger_{\sigma\tau}(\vec{x}_n)\vec{\sigma}_{\sigma\tau\kappa\lambda}\psi_{\kappa\lambda}(\vec{x}_n) \cdot \psi^\dagger_{\sigma'\tau'}(\vec{x}'_n)\vec{\sigma}_{\sigma'\tau'\kappa'\lambda'}\psi_{\kappa'\lambda'}(\vec{x}'_n)V_\sigma(\vec{x}_n - \vec{x}'_n) \\
&\quad - \frac{a^3}{2} \sum_{\vec{x}_n} \sum_{\substack{\sigma\tau\sigma'\tau' \\ \kappa'\lambda'}} \psi^\dagger_{\sigma\tau}(\vec{x}_n)\vec{\sigma}_{\sigma\tau\sigma'\tau'} \cdot \vec{\sigma}_{\sigma'\tau'\kappa'\lambda'}\psi_{\kappa'\lambda'}(\vec{x}_n)V_\sigma(0) \\
&= \frac{a^6}{2} \sum_{\vec{x}_n \vec{x}'_n} \left(\hat{\rho}^{(0)}_\sigma(\vec{x}_n)\hat{\rho}^{(0)}_\sigma(\vec{x}'_n) + 2\hat{\rho}^{(+)}_\sigma(\vec{x}_n)\hat{\rho}^{(-)}_\sigma(\vec{x}'_n) + 2\hat{\rho}^{(-)}_\sigma(\vec{x}_n)\hat{\rho}^{(+)}_\sigma(\vec{x}'_n) \right) V_\sigma(\vec{x}_n - \vec{x}'_n) \\
&\quad - \frac{3a^3}{2} \sum_{\vec{x}_n} \hat{\rho}(\vec{x}_n)V_\sigma(0).
\end{aligned}
\tag{8.29}
$$

Similar to Eq. (8.18), the spatial dependence of the spin-exchange potential has the

form

$$V_\sigma(\vec{x}_n - \vec{x}_n') = \frac{V_\sigma^{(0)}}{a^3} \delta_{\vec{x}_n, \vec{x}_n'} + \frac{V_\sigma^{(2)}}{a^5} \sum_{i=1}^{3} \left\{ \delta_{\vec{x}_n + a\vec{e}_i, \vec{x}_n'} - 2\delta_{\vec{x}_n, \vec{x}_n'} + \delta_{\vec{x}_n - a\vec{e}_i, \vec{x}_n'} \right\}. \tag{8.30}$$

With the same algebra as above, one finally arrives at

$$
\begin{aligned}
\hat{\mathcal{V}}_\sigma &= \frac{V_\sigma^{(0)}}{2a^3} \sum_{\vec{x}_n} a^6 \left(\hat{\rho}_\sigma^{(0)}(\vec{x}_n)^2 + 2\left(\hat{\rho}_\sigma^{(+)}(\vec{x}_n) + \hat{\rho}_\sigma^{(-)}(\vec{x}_n) \right)^2 \right) \\
&\quad - \frac{V_\sigma^{(2)}}{2a^5} \sum_{\vec{x}_n} a^6 \sum_{i=1}^{3} \left(\left(\hat{\rho}_\sigma^{(0)}(\vec{x}_n + a\vec{e}_i) - \hat{\rho}_\sigma^{(0)}(\vec{x}_n) \right)^2 \right. \\
&\quad + 2\left(\hat{\rho}_\sigma^{(+)}(\vec{x}_n + a\vec{e}_i) + \hat{\rho}_\sigma^{(-)}(\vec{x}_n + a\vec{e}_i) - \hat{\rho}_\sigma^{(+)}(\vec{x}_n) - \hat{\rho}_\sigma^{(-)}(\vec{x}_n) \right)^2 \right) \\
&\quad - \frac{3}{2} \left(\frac{V_\sigma^{(0)}}{a^3} - 6\frac{V_\sigma^{(2)}}{a^5} \right) \sum_{\vec{x}_n} a^3 \hat{\rho}(\vec{x}_n).
\end{aligned}
\tag{8.31}
$$

Finally, proceeding the same way as for the spin-exchange potential, the isospin-exchange potential has the form

$$
\begin{aligned}
\hat{\mathcal{V}}_\tau &= \frac{V_\tau^{(0)}}{2a^3} \sum_{\vec{x}_n} a^6 \left(\hat{\rho}_\tau^{(0)}(\vec{x}_n)^2 + 2\left(\hat{\rho}_\tau^{(+)}(\vec{x}_n) + \hat{\rho}_\tau^{(-)}(\vec{x}_n) \right)^2 \right) \\
&\quad - \frac{V_\tau^{(2)}}{2a^5} \sum_{\vec{x}_n} a^6 \sum_{i=1}^{3} \left(\left(\hat{\rho}_\tau^{(0)}(\vec{x}_n + a\vec{e}_i) - \hat{\rho}_\tau^{(0)}(\vec{x}_n) \right)^2 \right. \\
&\quad + 2\left(\hat{\rho}_\tau^{(+)}(\vec{x}_n + a\vec{e}_i) + \hat{\rho}_\tau^{(-)}(\vec{x}_n + a\vec{e}_i) - \hat{\rho}_\tau^{(+)}(\vec{x}_n) - \hat{\rho}_\tau^{(-)}(\vec{x}_n) \right)^2 \right) \\
&\quad - \frac{3}{2} \left(\frac{V_\tau^{(0)}}{a^3} - 6\frac{V_\tau^{(2)}}{a^5} \right) \sum_{\vec{x}_n} a^3 \hat{\rho}(\vec{x}_n)
\end{aligned}
\tag{8.32}
$$

with the isospin densities

$$\hat{\rho}_\tau^{(\alpha)}(\vec{x}) = \sum_{\sigma\tau\kappa\lambda} \psi_{\sigma\tau}^\dagger(\vec{x}) \tau_{\sigma\tau\kappa\lambda}^{(\alpha)} \psi_{\kappa\lambda}(\vec{x}), \ \alpha = 0, +, -, \tag{8.33}$$

assuming the same spatial dependence as in the other cases:

$$V_\tau(\vec{x}_n - \vec{x}_n') = \frac{V_\tau^{(0)}}{a^3} \delta_{\vec{x}_n, \vec{x}_n'} + \frac{V_\tau^{(2)}}{a^5} \sum_{i=1}^{3} \left\{ \delta_{\vec{x}_n + a\vec{e}_i, \vec{x}_n'} - 2\delta_{\vec{x}_n, \vec{x}_n'} + \delta_{\vec{x}_n - a\vec{e}_i, \vec{x}_n'} \right\}. \tag{8.34}$$

Here the spin-isospin matrices are

$$
\tau^{(0)} =
\begin{array}{c}
\begin{array}{cccc} \mathrm{p\uparrow} & \mathrm{p\downarrow} & \mathrm{n\uparrow} & \mathrm{n\downarrow} \end{array} \\
\begin{array}{c} \mathrm{p\uparrow} \\ \mathrm{p\downarrow} \\ \mathrm{n\uparrow} \\ \mathrm{n\downarrow} \end{array}
\left(
\begin{array}{cccc}
1 & 0 & 0 & 0 \\
0 & 1 & 0 & 0 \\
0 & 0 & -1 & 0 \\
0 & 0 & 0 & -1
\end{array}
\right)
\end{array}
\tag{8.35}
$$

$$
\tau^{(+)} =
\begin{array}{c}
\begin{array}{cccc} \mathrm{p\uparrow} & \mathrm{p\downarrow} & \mathrm{n\uparrow} & \mathrm{n\downarrow} \end{array} \\
\begin{array}{c} \mathrm{p\uparrow} \\ \mathrm{p\downarrow} \\ \mathrm{n\uparrow} \\ \mathrm{n\downarrow} \end{array}
\left(
\begin{array}{cccc}
0 & 0 & 1 & 0 \\
0 & 0 & 0 & 1 \\
0 & 0 & 0 & 0 \\
0 & 0 & 0 & 0
\end{array}
\right)
\end{array}
\tag{8.36}
$$

$$
\tau^{(-)} =
\begin{array}{c}
\begin{array}{cccc} \mathrm{p\uparrow} & \mathrm{p\downarrow} & \mathrm{n\uparrow} & \mathrm{n\downarrow} \end{array} \\
\begin{array}{c} \mathrm{p\uparrow} \\ \mathrm{p\downarrow} \\ \mathrm{n\uparrow} \\ \mathrm{n\downarrow} \end{array}
\left(
\begin{array}{cccc}
0 & 0 & 0 & 0 \\
0 & 0 & 0 & 0 \\
1 & 0 & 0 & 0 \\
0 & 1 & 0 & 0
\end{array}
\right)
\end{array} .
\tag{8.37}
$$

8.2 Nuclear Matter Monte Carlo Method

In order to study thermal properties of nuclear matter, the grand canonical partition function at a given temperature $T = \beta^{-1}$ needs to be determined,

$$
Z = \hat{\mathrm{Tr}} \left[\exp \left(-\beta \left(\hat{\mathcal{H}} - \sum_{\sigma,\tau} \mu_\tau \hat{\mathcal{N}}_{\sigma\tau} \right) \right) \right] \equiv \hat{\mathrm{Tr}} \left[\hat{U} \right],
\tag{8.38}
$$

with $\hat{\mathcal{N}}_{\sigma\tau} = \sum_{\vec{x}_n} \psi^\dagger_{\sigma\tau}(\vec{x}_n) \psi_{\sigma\tau}(\vec{x}_n)$. $\hat{U}$ is called the imaginary-time evolution operator (propagator) of the system and is a many-body operator. It can also be viewed as the partition operator at a given temperature. The Hamiltonian $\hat{\mathcal{H}}$ contains one- and two-body operators as described Section 8.1, and the trace is taken over all many-

body states as indicated by a caret. The partition function Z is an exponential over all one- and two-body operators (and therefore interactions) present in the system. It is impossible to deal with the partition function Z in this form, because the number of many-body correlations that have to be kept track of grows rapidly with system size. I therefore seek an expression for Z that is based on a single-particle representation, and I will replace the many-body problem with that of non-interacting nucleons that are coupled to a heat bath of auxiliary fields. This involves rewriting Z as a multi-dimensional integral.

8.2.1 Hubbard-Stratonovitch Transformation

I start by dividing the evolution operator into n_t so-called time slices:

$$\hat{U} = \exp\left(-\beta\left(\hat{\mathcal{H}} - \sum_{\sigma,\tau}\mu_\tau\hat{\mathcal{N}}_{\sigma\tau}\right)\right) = \left[\exp\left(-\Delta\beta\left(\hat{\mathcal{H}} - \sum_{\sigma,\tau}\mu_\tau\hat{\mathcal{N}}_{\sigma\tau}\right)\right)\right]^{n_t}, \quad (8.39)$$

with $\Delta\beta n_t = \beta$. The Trotter approximation [49, 50] is used to separate one-body (kinetic energy and chemical potential) and two-body terms (potential) in $\hat{\mathcal{H}}$:

$$\exp\left(-\Delta\beta\left(\hat{\mathcal{H}} - \sum_{\sigma,\tau}\mu_\tau\hat{\mathcal{N}}_{\sigma\tau}\right)\right) = \exp\left(-\Delta\beta\left(\hat{\mathcal{S}} + \hat{\mathcal{V}}\right)\right) \approx \exp\left(-\Delta\beta\hat{\mathcal{S}}\right)\exp\left(-\Delta\beta\hat{\mathcal{V}}\right),$$
$$(8.40)$$

collecting all single-body parts in $\hat{\mathcal{S}} \equiv \hat{\mathcal{K}} - \sum_{\sigma,\tau}\mu_\tau\hat{\mathcal{N}}_{\sigma\tau}$. Eq. (8.40) is valid to $\Delta\beta$, but becomes exact in the limit $\Delta\beta \to 0$.

The propagator of each time slice for the potential, $\exp(-\Delta\beta\hat{\mathcal{V}})$, is manipulated by applying the Hubbard-Stratonovitch transformation [51, 52] on each term, replacing it with a multi-dimensional integral over a set of auxiliary fields.

As an example, I describe the transformation by taking the on-site part of $\hat{\mathcal{V}}_c$ at one particular site $\vec{x}_m$. Using $\alpha \equiv \Delta\beta\frac{V_c^{(O)}}{2}$ and defining

$$S_\alpha = \begin{cases} \pm i & \text{if } \alpha > 0 \\ \pm 1 & \text{if } \alpha < 0, \end{cases} \quad (8.41)$$

the propagator for this single interaction is written as

$$
\begin{aligned}
\Delta\hat{U}\left(\vec{x}_m\right) &\equiv \exp\left(-\Delta\beta \frac{V_c^{(0)}}{2}\hat{\rho}^2\left(\vec{x}_m\right)\right) = \exp\left(-\alpha\hat{\rho}^2\left(\vec{x}_m\right)\right) \times \left(\sqrt{\frac{\pi}{|\alpha|}}\sqrt{\frac{|\alpha|}{\pi}}\right) \\
&= \sqrt{\frac{|\alpha|}{\pi}}\int_{-\infty}^{\infty}\mathrm{d}\chi\exp\left(-\alpha\hat{\rho}^2\left(\vec{x}_m\right) - |\alpha|\left(\chi + S_\alpha\hat{\rho}\left(\vec{x}_m\right)\right)^2\right) \\
&= \sqrt{\frac{|\alpha|}{\pi}}\int_{-\infty}^{\infty}\mathrm{d}\chi\exp\left(-|\alpha|\left[\chi^2 + 2S_\alpha\chi\hat{\rho}\left(\vec{x}_m\right)\right]\right).
\end{aligned} \tag{8.42}
$$

The last line of Eq. (8.42) reveals that the evolution operator is now expressed in terms of the exponential of a one-body operator and an integration over the auxiliary field χ. It has become a one-body propagator that corresponds to non-interacting nucleons coupled to this field. Since the integral is calculated with Monte Carlo methods, the field fluctuates according to a weight that is to be specified, hence the picture of a heat bath.

It has to be emphasized that $\hat{\rho}\left(\vec{x}_m\right)$ here represents a one-body operator for a subset ($\hat{\mathcal{V}}_c$ in this case) of the full interaction. Each quadratic term in (8.19), (8.31) and (8.32) has to be replaced by an integral. At a given lattice site $\vec{x}_m$, there are 20 auxiliary fields to form the full interaction, 4 for $\hat{\mathcal{V}}_c$ and 8 for $\hat{\mathcal{V}}_\sigma$ and $\hat{\mathcal{V}}_\tau$ each. Nucleons are now coupled to a big ensemble of auxiliary fields through which the interaction of the nucleons is mediated.

The $\Delta\hat{U}$'s are then multiplied together to form the evolution operator for one time slice at $\beta_m = m\Delta\beta$, which is expressed only in terms of single-body matrices,

$$
\begin{aligned}
\hat{U}\left(\beta_m\right) = \exp\left(-\Delta\beta\left(\hat{\mathcal{H}} - \sum_{\sigma,\tau}\mu_\tau\hat{\mathcal{N}}_{\sigma\tau}\right)\right) &= \Delta\hat{S}\Delta\hat{U}\left(\chi_1\right)\Delta\hat{U}\left(\chi_2\right)\cdots \\
&\cdots\Delta\hat{S}\cdots\Delta\hat{U}\left(\chi_{...}\right)\cdots\Delta\hat{U}\left(\chi_n\right)\cdots,
\end{aligned} \tag{8.43}
$$

with $\Delta S = \exp(-\Delta\beta\hat{S})$ as the one-body matrix representation of the kinetic and chemical potential evolution operator. Note that $\hat{U}\left(\beta_m\right)$ does not have an explicit dependence on β_m. All time slices have the same temperature dependence, namely $\Delta\beta$. In fact, β_m signifies the position of the particular time slice. Ultimately, all time

slices are multiplied together to form $\hat{U}$:

$$\hat{U} = \left[\exp\left(-\Delta\beta\hat{\mathcal{H}}\right)\right]^{n_t} = \int \mathcal{D}\left[\chi\right] G\left(\chi\right)\hat{U}_\chi \tag{8.44}$$

with the integration measure

$$\mathcal{D}\left[\chi\right] = \prod_{m=1}^{n_t} \prod_{\vec{x}_n} \prod_i \mathrm{d}\chi_{m,\vec{x}_n,i}\sqrt{\frac{|\alpha_i|}{\pi}}. \tag{8.45}$$

The $\alpha_i = \Delta\beta V_i/2$, $V_i \in \left[V_c^{(0)}, V_c^{(2)}, V_\sigma^{(0)}, \cdots\right]$ are the interaction-specific coupling strengths of auxiliary fields to nucleons, and the index i enumerates all fields at a particular site and time slice. The Gaussian factor G is given by

$$G\left(\chi\right) = \prod_{m=1}^{n_t} \prod_{\vec{x}_n} \prod_i \exp\left(-|\alpha_i|\chi_{m,\vec{x}_n,i}^2\right), \tag{8.46}$$

and the one-body propagator is

$$\hat{U}_\chi\left(\beta, 0\right) = \hat{U}\left(\beta_{n_t}\right)\hat{U}\left(\beta_{n_t-1}\right)\cdots\hat{U}\left(\beta_1\right). \tag{8.47}$$

Note that Eq. (8.44) only becomes exact in the limit of an infinite number of time slices, $n_t \to \infty$. For a finite n_t, the Hubbard-Stratonovitch approximation is valid only to order $\Delta\beta$.

In the practical implementation of Eq. (8.42), a discrete Hubbard-Stratonovitch transformation is used instead of the continuous form. The Monte Carlo procedure for calculating this integral involves taking samples of the integrand in a statistically independent manner as explained in Section 8.2.3. For a continuous integral, de-correlating consecutive samples takes many so-called sweeps. A typical autocorrelation length is hundred sweeps in the continuous case. The discrete Hubbard-Stratonovitch transformation only requires de-correlation of 10 to 20 sweeps and saves quite a bit of computer cycles. The ansatz for it is

$$\exp\left(-\alpha\hat{\rho}^2\left(\vec{x}_m\right)\right) \approx \int_{-\infty}^{\infty} \mathrm{d}\chi \exp\left(-2|\alpha|S_\alpha\chi\hat{\rho}\left(\vec{x}_m\right)\right)f\left(\chi\right), \tag{8.48}$$

and by comparing the Taylor expansion on both sides, one finds that

$$f(x) = \frac{2}{3}\delta(x) + \frac{1}{6}\delta(x - \chi_0) + \frac{1}{6}\delta(x + \chi_0), \quad \chi_0 = \sqrt{\frac{3}{2|\alpha|}}. \tag{8.49}$$

The auxiliary field can take on only three values, $\chi = 0, \pm\chi_0$ (as compared to an infinite number of values in the continuous case), and becomes a spin-1-like boson. Higher order expressions for f have been tested, and their Monte Carlo results have been found to be consistent with this approximation.

8.2.2 Calculation of Thermal Observables

A thermal observable $\langle\hat{O}\rangle$ is expressed as [45, 53]

$$\langle\hat{O}\rangle = \frac{1}{Z}\hat{\text{Tr}}\left[\hat{O}\exp\left(-\beta\left(\hat{\mathcal{H}} - \sum_{\sigma,\tau}\mu_\tau\hat{\mathcal{N}}_{\sigma\tau}\right)\right)\right] = \frac{\int\mathcal{D}[\chi]G(\chi)\langle\hat{O}(\chi)\rangle\xi(\chi)}{\int\mathcal{D}[\chi]G(\chi)\xi(\chi)} \tag{8.50}$$

and has the integration measure of Eq. (8.45) and Gaussian factor of Eq. (8.46). The expectation value of any operator in second quantization can be obtained with the help of Wick's theorem, and the resulting one-body densities are [45]

$$\langle\psi_{\sigma\tau}^\dagger(\vec{x}_n)\psi_{\sigma'\tau'}(\vec{x}_m)\rangle_\chi = \left\{[\mathbf{1} + \mathbf{U}_\chi(\beta,0)]^{-1}\mathbf{U}_\chi(\beta,0)\right\}_{(\sigma'\tau',\vec{x}_m),(\sigma\tau,\vec{x}_n)}. \tag{8.51}$$

The bold face $\mathbf{U}_\chi(\beta,0)$ is the single-body matrix representation of $\hat{U}_\chi(\beta,0)$.

Observables of the system are chosen to be the number of neutrons and protons, all components of the energy, and the pair correlation functions, the latter one is assumed to be BCS-like. Defining

$$\Delta_{(\sigma,\tau),(\sigma',\tau')}(\vec{x}_n,\vec{x}_m) = \psi_{\sigma\tau}(\vec{x}_n)\psi_{\sigma'\tau'}(\vec{x}_m) \tag{8.52}$$

$$P(z,(\sigma,\tau),(\sigma',\tau')) = \sum_{i=1\cdots3}\sum_{\vec{x}_n}\langle\Delta_{(\sigma,\tau),(\sigma',\tau')}^\dagger(\vec{x}_n,\vec{x}_n+z\vec{e}_i)\Delta_{(\sigma,\tau),(\sigma',\tau')}(\vec{x}_n,\vec{x}_n+z\vec{e}_i)\rangle \tag{8.53}$$

$$P_{\text{fermi}} = \frac{3\left(\sum_{\vec{x}_n}\sum_{(\sigma,\tau)}\langle\psi_{\sigma\tau}^\dagger(\vec{x}_n)\psi_{\sigma\tau}(\vec{x}_n)\rangle\right)^2}{16N}, \tag{8.54}$$

the correlation function is given by

$$C\left(z,(\sigma,\tau),(\sigma',\tau')\right) = \frac{P\left(z,(\sigma,\tau),(\sigma',\tau')\right)}{P_{\text{fermi}}}. \tag{8.55}$$

Eq. (8.55) gives the correlation of one particle with spin/isospin (σ,τ) that is separated from another particle of spin/isospin (σ',τ') by a distance z. A value of $C = 0$ indicates that the correlation is suppressed, a high value shows that two particles are correlated with each other. $C = 1$ is the independent particle value. Note that C is summed over all three spatial directions, since the system is isotropic.

8.2.3 Monte Carlo Procedure

The integrals in (8.50) are evaluated using the Metropolis algorithm [17]. The basic idea involves sampling the integrand of (8.50),

$$\langle \hat{O}(\chi) \rangle = \frac{\hat{\text{Tr}}\left[\hat{O}\hat{U}_\chi\left(\beta,0\right)\right]}{\hat{\text{Tr}}\left[\hat{U}_\chi\left(\beta,0\right)\right]}, \tag{8.56}$$

within the boundaries of the integration volume according to a positive-definite weight

$$W\left(\chi\right) = \begin{cases} |G(\chi)\xi(\chi)| & \text{for continuous HS} \\ |\xi(\chi)| & \text{for discrete HS}, \end{cases} \tag{8.57}$$

with

$$\xi(\chi) = \hat{\text{Tr}}\left[\hat{U}_\chi\left(\beta,0\right)\right] = \det\left[\mathbf{1} + \mathbf{U}_\chi\left(\beta,0\right)\right]. \tag{8.58}$$

The last equality can be proven by expanding the determinant [53]. Samples are being taken by a so-called random walker that travels through χ-space, taking a new value χ_{new} from the previous one χ_{old} if the ratio

$$r = \frac{W(\chi_{\text{new}})}{W(\chi_{\text{old}})} \tag{8.59}$$

is larger than one, or else, if $r < 1$, taking on χ_{new} with probability r. It can be shown [54] that the sequence of values the walker is taking is distributed according to the weight function $W(\chi)$, which is typically chosen to be as close to the integrand as possible to increase the efficiency of the procedure. Since the consecutive steps are correlated, the walker has to travel several steps before another sample is taken to de-correlate them. The average of an observable (8.50) is then simply

$$\langle \hat{O} \rangle = \frac{\frac{1}{N_s} \sum_i \langle \hat{O} \rangle_i \Phi_i}{\frac{1}{N_s} \sum_i \Phi_i}, \qquad (8.60)$$

where N_s is the number of samples and

$$\Phi_i = \begin{cases} \frac{G(\chi)\xi(\chi)}{W(\chi)} & \text{for continuous HS} \\ \frac{\xi(\chi)}{W(\chi)} & \text{for discrete HS.} \end{cases} \qquad (8.61)$$

Note that Φ_i, which is just the sign of the weight W, can generally be negative or even complex.

8.2.4 Sign Problem

The numerical determination of Eq. (8.60), which is the Monte Carlo equivalent of the integrals in Eq. (8.50), can be difficult in certain situations, even with Monte Carlo methods: If $S_\alpha = \pm i$ (which generally corresponds to a repulsive on-site and an attractive next-neighbor interaction, cf. Eq. (8.41)), propagators for the potential (Eq. (8.42)) contribute negative or complex elements to $\hat{U}_\chi(\beta, 0)$ (see Eq. (8.58)). The integrands in both numerator and denominator are oscillatory, and the integrals can add up to small numbers. While numerator and denominator of Eq. (8.60) cancel analytically, a numerical evaluation with Monte Carlo methods causes large uncertainties because the methods are of a stochastic nature, and the number of samples in a computation remains finite. This is a complication associated with these methods when the Hubbard-Stratonovitch transformation is used. It is referred to as the Monte Carlo sign problem. A pragmatic solution has been used for the shell model

Monte Carlo method to handle this complication [48].

This problem unfortunately forces the use of a nuclear potential that contradicts the usual physical understanding and intuition. It is generally known that the central potential has a strong repulsion for short distances and features a long-range attraction. Here, the desire to avoid the sign problem generates the opposite: on-site attraction and next-neighbor repulsion. Nevertheless, in this lattice discretization, the position of the nucleons at the same site is only determined up to a cube of size a. Therefore, the on-site potential parameter can be seen as some kind of average potential within that cube, and by tuning the lattice spacing accordingly, it could be possible that this parameter is negative. The exact definition of the parameter actually depends on a regularization scheme described in Section 8.3. If a positive on-site parameter is chosen, emulating a hard core repulsion, one has to deal with oscillatory integrands and commensurately large error bars. The same line of argumentation applies to the next-neighbor parameter. Another hint that the on-site attraction and next-neighbor repulsion is not completely unreasonable is given by the fact that there have been several mean field calculations of nuclear matter with the Skyrme forces. Skyrme forces simulate the interaction with a δ-like attraction and a $\nabla^2\delta$-like repulsion.

There is another complication connected to the spin- and isospin-exchange interaction. I chose to write the spin-exchange $\vec{\sigma}\cdot\vec{\sigma}$ in terms of the Pauli spin matrices $\sigma^{(0)}$, $\sigma^{(+)}$ and $\sigma^{(-)}$. This avoids introducing complex components in the one-body evolution operator and reduces the number of fields from three to two. It also creates an uniaxial spin/isospin anisotropy which is very similar to the studies of choices of auxiliary fields for the Hubbard model, as discussed in Ref. [59]. However, removing phases from the evolution operator leaves another sign problem that occurs as soon as more than one time slice is involved. I illustrate the problem for the spin-exchange (on-site) and restrict myself to one particular site using the discrete Hubbard-Stratonovitch transformation. It is easy to see that it also holds in the general case involving many

sites and auxiliary fields. One time slice is written as

$$
\begin{aligned}
\Delta\hat{U} &= \exp\left(-\alpha\left(\hat{\rho}_\sigma^{(0)}(\vec{x}_m)^2 + 2\left(\hat{\rho}_\sigma^{(+)}(\vec{x}_m) + \hat{\rho}_\sigma^{(-)}(\vec{x}_m)\right)^2\right)\right) \\
&= \int_{-\infty}^{\infty} d\chi_1 d\chi_2 f(\chi_1) f(\chi_2) \times \\
&\times \exp\left(-2|\alpha|\chi_1\hat{\rho}_\sigma^{(0)}(\vec{x}_m) - 4|\alpha|\chi_2\left(\hat{\rho}_\sigma^{(+)}(\vec{x}_m) + \hat{\rho}_\sigma^{(-)}(\vec{x}_m)\right)\right). \quad (8.62)
\end{aligned}
$$

Evaluating the integrals stochastically involves taking samples in χ-space at points that are distributed according to the weight function W. The sign of W

$$
\langle\text{sign}\rangle = \frac{\int_{-\infty}^{\infty} d\chi_1 d\chi_2 d\chi_3 d\chi_4 \det\left[\mathbf{1} + \mathbf{U_2}\right]}{\int_{-\infty}^{\infty} d\chi_1 d\chi_2 d\chi_3 d\chi_4 |\det\left[\mathbf{1} + \mathbf{U_2}\right]|} \quad (8.63)
$$

for two time slices, $\Delta\hat{U}_2 = \Delta\hat{U}\Delta\hat{U}$, can be less than one since the integrand of the numerator,

$$
\begin{aligned}
\det\left[\mathbf{1} + \mathbf{U_2}\right] &= 2 + 2\cosh(c_1 + c_3)\cosh(2c_2)\cosh(2c_4) \\
&\quad + 2\cosh(c_1 - c_3)\sinh(2c_2)\sinh(2c_4), \quad (8.64)
\end{aligned}
$$

can take on negative values for certain combinations of values of $c_i = 0, \pm\sqrt{6|\alpha|}$. This would not be the case for just one time slice, the so-called static path approximation (SPA). Similar observations have been made for the Heisenberg model (see Ref. [59]).

8.2.5 Sparse Matrix Technique

There has been significant effort in stabilizing [55] and optimizing [53] the Metropolis algorithm for lattice calculations, as they have been heavily used for models of interacting electrons in condensed matter Physics. Many of the techniques can be directly applied to NMMC, because the models are similar.

In a straightforward approach, the Metropolis algorithm would be applied by changing all auxiliary fields in all time slices, and then performing the ratio test (8.59). For a typical number of 10 to 20 time slices, 12800 to 25600 fields would change simultaneously (for a $4\times4\times4$ lattice), and the new position χ_{new} of the random

walker in χ-space would likely be far away from the old one. Knowing that the weight function $W(\chi)$ (according to which the subsequent positions of the walker have to be distributed) is peaked, or has at least a local structure for low temperatures, the Monte Carlo procedure is likely to be frustrated: Either a new position would never be accepted, because it is always in an unimportant region, or the more weighted regions of χ-space are never found, because the actual step size in χ-space, due to the large number of changed fields, is too big. On the other hand, changing only one auxiliary field may waste too many computer cycles, because the new position is in immediate vicinity of the old one. De-correlating samples may then take too many steps.

Furthermore, it would be helpful if the computational burden of re-calculating the trace of $\mathbf{1} + \mathbf{U}_\chi$ (cf. Eq. (8.58)), if changing a field in some intermediate time slice, would be reduced, since at first sight it involves many matrix multiplications. A type of wrapping mechanism that shuffles the time slice of interest to a convenient place in the chain of time slices would be helpful. Finally, a sparse matrix technique has to be introduced, which reduces the computation time from the order N_M^3, the usual scale of matrix multiplication, to N_M^2, N_M being the dimension of the matrix.

The checkerboard breakup is a first step using this technique. I illustrate it in one spatial dimension. It applies to the kinetic energy matrix

$$
\exp(-\Delta\beta\mathcal{K}) = \exp \begin{pmatrix}
-2t & t & \cdots & 0 & \cdots & 0 & t \\
t & -2t & t & 0 & \cdots & 0 & 0 \\
0 & t & -2t & t & 0 & \cdots & 0 \\
0 & \cdots & \ddots & \ddots & \ddots & \cdots & 0 \\
0 & 0 & \cdots & 0 & t & -2t & t \\
t & 0 & 0 & \cdots & 0 & t & -2t
\end{pmatrix}. \tag{8.65}
$$

with $t = \Delta\beta t_0$. Using the Trotter approximation, it can be broken up into

$$
\exp\begin{pmatrix} -t & t & 0 & 0 & \cdots \\ t & -t & 0 & 0 & \cdots \\ 0 & 0 & 0 & 0 & \cdots \\ 0 & 0 & 0 & \ddots & \cdots \\ 0 & 0 & 0 & 0 & \ddots \end{pmatrix}
\exp\begin{pmatrix} 0 & 0 & 0 & 0 & \cdots \\ 0 & -t & t & 0 & \cdots \\ 0 & t & -t & 0 & \cdots \\ 0 & 0 & 0 & \ddots & \cdots \\ 0 & 0 & 0 & 0 & \ddots \end{pmatrix}
\exp\begin{pmatrix} 0 & 0 & 0 & 0 & \cdots \\ 0 & 0 & 0 & 0 & \cdots \\ 0 & 0 & -t & t & \cdots \\ 0 & 0 & t & -t & \cdots \\ 0 & 0 & 0 & 0 & \ddots \end{pmatrix}\cdots.
$$
(8.66)

All matrices can now be evaluated separately, resulting in

$$
\begin{pmatrix} m_0 & m_1 & 0 & 0 & \cdots \\ m_1 & m_0 & 0 & 0 & \cdots \\ 0 & 0 & 0 & 0 & \cdots \\ 0 & 0 & 0 & \ddots & \cdots \\ 0 & 0 & 0 & 0 & \ddots \end{pmatrix}
\begin{pmatrix} 0 & 0 & 0 & 0 & \cdots \\ 0 & m_0 & m_1 & 0 & \cdots \\ 0 & m_1 & m_0 & 0 & \cdots \\ 0 & 0 & 0 & \ddots & \cdots \\ 0 & 0 & 0 & 0 & \ddots \end{pmatrix}
\begin{pmatrix} 0 & 0 & 0 & 0 & \cdots \\ 0 & 0 & 0 & 0 & \cdots \\ 0 & 0 & m_0 & m_1 & \cdots \\ 0 & 0 & m_1 & m_0 & \cdots \\ 0 & 0 & 0 & 0 & \ddots \end{pmatrix}\cdots
$$
(8.67)

with

$$
m_0 = \frac{1}{2}\left(1 + \exp(-2t)\right) \tag{8.68}
$$

$$
m_1 = \frac{1}{2}\left(1 - \exp(-2t)\right). \tag{8.69}
$$

For three dimensions the breakup works in the same manner except that the next-neighbor matrix element (and therefore the off-diagonal elements as well as the second diagonal element) may be at a different location in the matrix. A similar propagation technique is applied to the spin and isospin off-diagonal elements of the exchange potentials. One finds for spin-exchange:

$$
\exp\begin{pmatrix} 0 & s_1 & 0 & 0 \\ s_1 & 0 & 0 & 0 \\ 0 & 0 & 0 & s_1 \\ 0 & 0 & s_1 & 0 \end{pmatrix} = \begin{pmatrix} \cosh s_1 & \sinh s_1 & 0 & 0 \\ \sinh s_1 & \cosh s_1 & 0 & 0 \\ 0 & 0 & \cosh s_1 & \sinh s_1 \\ 0 & 0 & \sinh s_1 & \cosh s_1 \end{pmatrix}, \tag{8.70}
$$

and

$$\exp \begin{pmatrix} 0 & 0 & t_1 & 0 \\ 0 & 0 & 0 & t_1 \\ t_1 & 0 & 0 & 0 \\ 0 & t_1 & 0 & 0 \end{pmatrix} = \begin{pmatrix} \cosh t_1 & 0 & \sinh t_1 & 0 \\ 0 & \cosh t_1 & 0 & \sinh t_1 \\ \sinh t_1 & 0 & \cosh t_1 & 0 \\ 0 & \sinh t_1 & 0 & \cosh t_1 \end{pmatrix} \qquad (8.71)$$

for isospin-exchange.

After one (or a small set) of auxiliary fields for either the on-site interaction or the next-neighbor interaction is flipped in a time slice, the ratio of the determinants (Eq. (8.59)),

$$r = \frac{\det \left[\mathbf{1} + \mathbf{U}_{\chi_{\mathrm{new}}}(\beta, 0)\right]}{\det \left[\mathbf{1} + \mathbf{U}_{\chi_{\mathrm{old}}}(\beta, 0)\right]}, \qquad (8.72)$$

needs to be calculated in order to determine whether the new value is accepted. Instead of flipping all auxiliary fields of one time slice at a time, I now flip one or a few χ-fields and do the acceptance test immediately. Since

$$\det \left[\mathbf{1} + \mathbf{U}_{\chi_{\mathrm{new}}}\right] = \det \left[\mathbf{1} + \mathbf{U}(\beta_{n_t}) \mathbf{U}(\beta_{n_t-1}) \cdots \mathbf{U}(\beta_1)\right] \qquad (8.73)$$

is invariant against cyclic permutation of the time slices $\mathbf{U}(\beta_l)$, the time slice l that is to be altered can be put in front, and this results in

$$\mathbf{1} + \mathbf{U}_{\chi_{\mathrm{new}}} = \mathbf{1} + (\mathbf{1} + \mathbf{\Delta}(\mathbf{l})) \mathbf{U}(\beta_l) \mathbf{U}(\beta_{l-1}) \cdots \mathbf{U}(\beta_{l+1}). \qquad (8.74)$$

The time slice $\mathbf{U}(\beta_l)$ is now conveniently written as $\mathbf{U}(\beta_l) = \mathbf{Q} * \mathbf{W}$, in such a way that only $\mathbf{Q}$ contains matrix elements with the flipped χ-field. This can be done using the Trotter approximation. Note that for the central potential the matrix $\mathbf{\Delta}(\mathbf{l})$ only has one (on-site) or two (next-neighbor interaction) nonzero elements at position (i, i) or $(i-1, i-1)$ per changed auxiliary fields:

$$\begin{aligned} (\mathbf{\Delta}(\mathbf{l}))_{jk} &= \delta_{j,i}\delta_{k,i} \left(\exp\left\{\alpha(\chi_{\mathrm{old}} - \chi_{\mathrm{new}})\right\} - 1\right) & \text{at site } i \\ (\mathbf{\Delta}(\mathbf{l}))_{jk} &= \delta_{j,i-1}\delta_{k,i-1} \left(\exp\left\{-\alpha(\chi_{\mathrm{old}} - \chi_{\mathrm{new}})\right\} - 1\right) & \text{at site } i-1 \end{aligned} \qquad (8.75)$$

Here, I have summarized all remaining pre-factors like potential strength in the variable α. Introducing the Green's function at a given time slice l,

$$\mathbf{G}_{jk}(l) = \left[\mathbf{1} + \mathbf{U}\left(\beta_l\right)\mathbf{U}\left(\beta_{l-1}\right)\cdots\mathbf{U}\left(\beta_{l+1}\right)\right]^{-1}_{jk}, \tag{8.76}$$

the ratio can be determined as

$$
\begin{aligned}
r &= \det\left[\,\left(\mathbf{1} + \mathbf{U}\left(\beta_l\right)\mathbf{U}\left(\beta_{l-1}\right)\cdots\mathbf{U}\left(\beta_{l+1}\right)\right)^{-1}\right. \\
&\quad \left.\times\left(\mathbf{1} + \left(\mathbf{1} + \boldsymbol{\Delta}(\mathbf{l})\right)\mathbf{U}\left(\beta_l\right)\mathbf{U}\left(\beta_{l-1}\right)\cdots\mathbf{U}\left(\beta_{l+1}\right)\right)\,\right] \\
&= \det\left[\mathbf{1} + \mathbf{G}(l)\boldsymbol{\Delta}(l)\mathbf{U}\left(\beta_l\right)\mathbf{U}\left(\beta_{l-1}\right)\cdots\mathbf{U}\left(\beta_{l+1}\right)\right] = \det\left[\mathbf{1} + \left(\mathbf{1} - \mathbf{G}(l)\right)\boldsymbol{\Delta}(l)\right]
\end{aligned}
\tag{8.77}
$$

using once again cyclic permutation. Since $\boldsymbol{\Delta}(l)$ has only a few nonzero elements, the ratio r is quickly computed.

The price for this improvement is the fact that the Green's function needs to be updated when fields are flipped. Within a time slice, I get

$$
\begin{aligned}
\mathbf{G}'(l) &= \left(\mathbf{1} + \left(\mathbf{1} + \boldsymbol{\Delta}(l)\right)\mathbf{U}\left(\beta_l\right)\mathbf{U}\left(\beta_{l-1}\right)\cdots\mathbf{U}\left(\beta_{l+1}\right)\right)^{-1} \\
&= \mathbf{G}(l)\left(\,\mathbf{1} + \boldsymbol{\Delta}(l)\mathbf{U}\left(\beta_l\right)\mathbf{U}\left(\beta_{l-1}\right)\cdots\mathbf{U}\left(\beta_{l+1}\right)\right. \\
&\quad \left.\times\left(\mathbf{1} + \mathbf{U}\left(\beta_l\right)\mathbf{U}\left(\beta_{l+1}\right)\cdots\mathbf{U}\left(\beta_{l+1}\right)\right)^{-1}\,\right)^{-1} \\
&= \mathbf{G}(l)\left(\mathbf{1} + \mathbf{H}\right)^{-1}
\end{aligned}
\tag{8.78}
$$

with

$$\mathbf{H} = \boldsymbol{\Delta}(l)\left[\mathbf{1} - \mathbf{G}(l)\right], \tag{8.79}$$

using

$$\mathbf{G}(l+1) = \mathbf{U}\left(\beta_{l+1}\right)\mathbf{G}(l)\mathbf{U}\left(\beta_{l+1}\right)^{-1} \tag{8.80}$$

to shuffle the next time slice in front. Once again, the computation for updating $\mathbf{G}(l)$ is much less than with a straightforward approach. I have now established a fast and convenient way to update and evolve $\mathbf{U}_\chi(\beta)$ and $\mathbf{G}$.

8.3 Schrödinger Equation on a Lattice

Instead of a phenomenological approach in which the saturation curve E/A versus ρ is simply fitted, potential parameters could also be determined from scattering data. This is a lattice regularization of the NN effective field theory and puts the calculation on a firmer ground by using a more realistic potential. This would assume that the model Hamiltonian is complete enough to sufficiently describe and fit the NN scattering data. At the moment, however, the choice of the Hamiltonian is very limited: It just has three different components, and the spatial part only consists of two points in space. A full and satisfying solution should therefore not be expected. But for future application, a brief overview of the theory is presented here. More details can be found in [56].

8.3.1 NN potential from Scattering Data

Since the theory basically involves the spatial part of the potential, I concentrate on $\hat{\mathcal{V}}_c$. I start with discretizing the continuous two-body Schrödinger equation,

$$\left(\frac{\hbar^2}{m_N} \vec{\nabla}^2 + V_c^{(0)} \delta\left(\vec{x}\right) + V_c^{(2)} \left(\nabla^2 \delta\left(\vec{x}\right) \right) \right) \phi\left(\vec{x}\right) = E\phi\left(\vec{x}\right), \tag{8.81}$$

which describes the wave function ϕ of the relative coordinate $\vec{x}$, and obtain

$$-t \left(\sum_{i=1}^{3} \phi\left(\vec{x}_n + a\vec{e}_i\right) - 2\phi\left(\vec{x}_n\right) + \phi\left(\vec{x}_n - a\vec{e}_i\right) \right) + \frac{V_c^{(0)}}{a^3} \delta_{\vec{x}_n,0}$$

$$+ \frac{V_c^{(2)}}{a^5} \sum_{i=1}^{3} \left(\delta_{\vec{x}_n,-a\vec{e}_i} - 2\delta_{\vec{x}_n,0} + \delta_{\vec{x}_n,a\vec{e}_i} \right) \phi\left(\vec{x}\right) = E\phi\left(\vec{x}\right) \tag{8.82}$$

with $t = \hbar^2/m_N a^2$. Taking the Fourier transform, which is defined as

$$\tilde{F}\left(\vec{p}_k\right) = \sum_n a^3 f\left(\vec{x}_n\right) e^{-i\vec{p}_k \cdot \vec{x}_n}, \tag{8.83}$$

I get, after introducing

$$S\left(\vec{p}_k\right) = 2\left(\sum_{i=1}^{3}\cos\left(a\vec{p}_k\cdot\vec{e}_i\right)\right) - 6 \tag{8.84}$$

and

$$-\frac{E}{t} \equiv S\left(\vec{p}_E\right) = 2\left(\sum_{i=1}^{3}\cos\left(a\vec{p}_E\cdot\vec{e}_i\right)\right) - 6, \tag{8.85}$$

the following expression for the Fourier transform of ϕ:

$$\tilde{\phi}\left(\vec{p}_k\right) = \frac{\left(\frac{V_c^{(0)}}{t} - 6\frac{V_c^{(2)}}{a^2 t}\right)\phi\left(0\right) + \frac{V_c^{(2)}}{a^2 t}\phi_a\left(S\left(\vec{p}_k\right) + 6\right)}{S\left(\vec{p}_k\right) - S\left(\vec{p}_E\right)} \equiv \frac{A\phi\left(0\right) + B\phi_a\left(S\left(\vec{p}_k\right) + 6\right)}{S\left(\vec{p}_k\right) - S\left(\vec{p}_E\right)}. \tag{8.86}$$

Here, I defined A and B as new potential parameters and used the fact that for s-wave scattering, $\phi\left(\vec{x}_n\right)$ is symmetric and isotropic which manifests itself in $\phi_a \equiv \phi\left(\pm a\vec{e}_i\right)\ \forall i$ and a real $\tilde{\phi}\left(\vec{p}_k\right)$. The constants $\phi\left(0\right)$ and ϕ_a are obtained by using the inverse Fourier transform which yields

$$\phi\left(0\right) = \frac{1}{Na^3}\sum_k \tilde{\phi}\left(\vec{p}_k\right) \tag{8.87}$$

$$\phi_a = \frac{1}{Na^3}\sum_k \tilde{\phi}\left(\vec{p}_k\right)e^{i\vec{p}_k\cdot a\vec{e}_i}\ \forall i. \tag{8.88}$$

They can be expressed as functions of A, B and various sums over functions of S, defined as:

$$G_0\left(\vec{p}_E\right) = \frac{1}{Na^3}\sum_k \frac{1}{S\left(\vec{p}_k\right) - S\left(\vec{p}_E\right)}$$

$$G_1\left(\vec{p}_E\right) = \frac{1}{Na^3}\sum_k \frac{\sum_{i=1}^{3}\cos ap_{ki}}{S\left(\vec{p}_k\right) - S\left(\vec{p}_E\right)}$$

$$G_2\left(\vec{p}_E\right) = \frac{1}{Na^3}\sum_k \frac{\sum_{i=1}^{3}\cos^2 ap_{ki}}{S\left(\vec{p}_k\right) - S\left(\vec{p}_E\right)}. \tag{8.89}$$

Note that these terms need to be regularized appropriately, for example by adding a small imaginary part to the denominator and imposing some unitarity condition. Other regularization procedures are probably equivalent. Eqs. (8.87) and (8.88) be-

come

$$\phi(0)\{1 - AG_0(\vec{p}_E)\} = \frac{1}{\sqrt{Na^3}} + 2B\phi_a G_1(\vec{p}_E) \tag{8.90}$$

$$\phi_a\{1 - 2BG_2(\vec{p}_E)\} = \frac{\frac{S(\vec{p}_E)}{6} + 1}{\sqrt{Na^3}} + \frac{A\phi(0)}{3}G_1(\vec{p}_E). \tag{8.91}$$

Eqs. (8.90) and (8.91) can be solved for $\phi(0)$ and ϕ_a, which then become functions of A and B. The final form for ϕ is

$$
\begin{aligned}
\phi(\vec{x}_n) &= \frac{1}{Na^3}\sum_k \tilde{\phi}(\vec{p}_k)\, e^{i\vec{p}_k\cdot a\vec{x}_n} \\
&= \frac{1}{\sqrt{Na^3}}e^{i\vec{p}_E\cdot\vec{x}_n} + A\phi(0)\frac{1}{Na^3}\sum_k \frac{e^{i\vec{p}_k\cdot\vec{x}_n}}{S(\vec{p}_k) - S(\vec{p}_E)} \\
&\quad + 2B\phi_a\frac{1}{Na^3}\sum_k \frac{\left(\sum_{i=1}^{3}\cos ap_{ki}\right)e^{i\vec{p}_k\cdot\vec{x}_n}}{S(\vec{p}_k) - S(\vec{p}_E)}.
\end{aligned}
\tag{8.92}
$$

By taking the continuous limit, $N \to \infty$, $a \to 0$, the spherical outgoing wave and the scattering amplitude $f(\vec{p}_E)$ of the common scattering solution can be identified:

$$\frac{1}{Na^3}\sum_k \frac{e^{i\vec{p}_k\cdot\vec{x}_n}}{S(\vec{p}_k) - S(\vec{p}_E)} \longrightarrow \frac{1}{4\pi a^2}\frac{e^{ip_E x}}{x} \tag{8.93}$$

$$\frac{1}{Na^3}\sum_k \frac{\left(\sum_{i=1}^{3}\cos ap_{ki}\right)e^{i\vec{p}_k\cdot\vec{x}_n}}{S(\vec{p}_k) - S(\vec{p}_E)} \longrightarrow \frac{1}{4\pi a^2}\left(1 - \frac{1}{2}a^2\vec{p}_E^{\,2}\right)\frac{e^{ip_E x}}{x}. \tag{8.94}$$

From Eq. (8.92),(8.93) and (8.94) I obtain for the scattering amplitude:

$$f(\vec{p}_E) = \frac{\sqrt{Na^3}}{4\pi a^2}\left(A\phi(0) + 2B\phi_a\left(1 - \frac{1}{2}a^2\vec{p}_E^{\,2}\right)\right). \tag{8.95}$$

This is an expression for the scattering amplitude which is a nonlinear function of the potential coefficients, A and B. Their value can be determined by using the scattering length

$$a_s = -\lim_{\vec{p}_E\to 0} f(\vec{p}_E)\, e^{i\delta(\vec{p}_E)} \tag{8.96}$$

and effective range

$$\frac{1}{|f\left(\vec{p}_E\right)|^2} = \vec{p}_E{}^2 + \left(\frac{1}{2}r_0\vec{p}_E{}^2 - \frac{1}{a_s}\right)^2 . \tag{8.97}$$

These are highly nonlinear equations for A and B, to be solved on a computer.

8.3.2 Conclusion

The numerical search of Eqs. (8.95), (8.96) and (8.97) did not give any meaningful parameters, whether I restrict myself to the central potential or whether I use spin- and isospin-dependent scattering lengths and effective ranges. A good energy curve was not obtained, and the saturation energy and density could not be reproduced. It is known that saturation is accomplished by tensor and three-body forces, as described in Chapter 6. The latter is not present in the scattering problem or the Hamiltonian I chose. The tensor force could be implemented as soon as computer power increases. The scattering data, on the other hand, are represented in this approach by just two basic quantities, a crucial restriction of usage of available information. These two quantities could be probes of the nuclear potential that are not present in the model Hamiltonian. The information contained in nucleon-nucleon elastic phase shifts does not determine the potential uniquely: The underlying nuclear potential could be nonlocal or energy dependent which reflects the fact that the nucleon itself has a composite structure and that the elimination of inelastic channels leads to energy dependent terms. Nevertheless, a phenomenological approach is always possible because the obtained set of parameters of the Hamiltonian simulate the effects of other parts of full nuclear potential.

8.4 Technical Details of All Calculations

In the following I investigate symmetric nuclear matter (SNM) and pure neutron matter (PNM). The aim of the thermal calculation is threefold: First I want to show that it is possible to reproduce the saturation energy and density for SNM in a reasonable manner, and secondly describe a (first order) phase transition from a

Fermi gas at high temperatures to a clustered system if the temperature is lowered. The temperature range of the investigation will be

$$3.0 \, \text{MeV} \leq T \leq 100 \, \text{MeV}, \tag{8.98}$$

and the time slices will have an inverse temperature parameter of

$$\Delta\beta = 0.01 \, \text{MeV}. \tag{8.99}$$

Finally, I am addressing the same three issues for PNM. The project is considered to be a first step towards a realistic calculation. A complete project has to contain more parts of the nuclear potential and the spatial resolution has to improve.

The lattice has a spacing of

$$a = 1.842 \, \text{fm} \tag{8.100}$$

and is tuned such that quarter filling of the lattice is at saturation density $\rho_0 = 0.16 \, \text{fm}^{-3}$. Because of limited CPU time, the calculation is restricted to $4 \times 4 \times 4$ lattices for the moment. This lattice comprises 10^{38} many-body states.

The fit of the energy curve and saturation properties for SNM which will be reported in Chapter 9 yield the following potential parameters:

$$V_c^{(0)} = -181.5 \, \text{MeV} \, \text{fm}^3, \tag{8.101}$$

$$V_c^{(2)} = 37.8 \, \text{MeV} \, \text{fm}^5, \tag{8.102}$$

$$V_\sigma^{(0)} = -31.25 \, \text{MeV} \, \text{fm}^3, \tag{8.103}$$

$$V_\sigma^{(2)} = 0.0 \, \text{MeV} \, \text{fm}^5. \tag{8.104}$$

All calculations for SNM and PNM were done with this set of parameters. They are a fit to the SNM case. I do not consider the inclusion of isospin exchange terms for PNM because the calculations for this case do not turn out to have converged yet. A comparison is rather made how well this potential already captures important features of PNM. The calculations were performed on Caltech's HP Exemplar X-class

supercomputer with 256 nodes.

Chapter 9 Numerical Results and Discussion

I start my description of results by elaborating on some test cases that determine some critical parameters of the calculations: A comparison with a Hartree-Fock calculation for the simplest type of interaction is given. In the subsequent section I show that for symmetric nuclear matter (SNM) the energy per particle can be reproduced quite well over a wide range of densities. Then, several observations are presented that give evidence of a first order phase transition from a Fermi gas to a clustered system at some critical temperature T_c. The two-body correlations are examined to study what kind of clusters appear in the condensed phase. Furthermore, the symmetry energy, first sound, as well as the energy of one-dimensional SNM are discussed, before the chapter closes with a brief summary on pure neutron matter.

9.1 Test Cases

First, some more technical details of the calculations have to be clarified. As mentioned in Section 8.2.1, the Trotter (Eq. (8.40)) and Hubbard-Stratonovitch approximation (Eq. (8.44)) become exact only in the limit $\Delta\beta \to 0$. Since a simulation has to be carried out with a finite $\Delta\beta$, a test has to be made at which value the expectation values of observables are not affected by the finiteness of $\Delta\beta$ anymore. For a typical temperature (in this case $T = 4$ MeV) and chemical potential ($\mu = 0$ MeV), Fig. 9.1 shows how the energy per particle, E/A, behaves as a function of $\Delta\beta$. Clearly, at $\Delta\beta = 0.015$ MeV^{-1} and smaller values, E/A does not change significantly anymore, and it is assumed that a value of $\Delta\beta = 0.01$ MeV^{-1} should be sufficient to guarantee reliable results. The behaviour as displayed in Fig. 9.1 is typical for all observables. The energy, however, is one of the more critical observables, because the evaluation
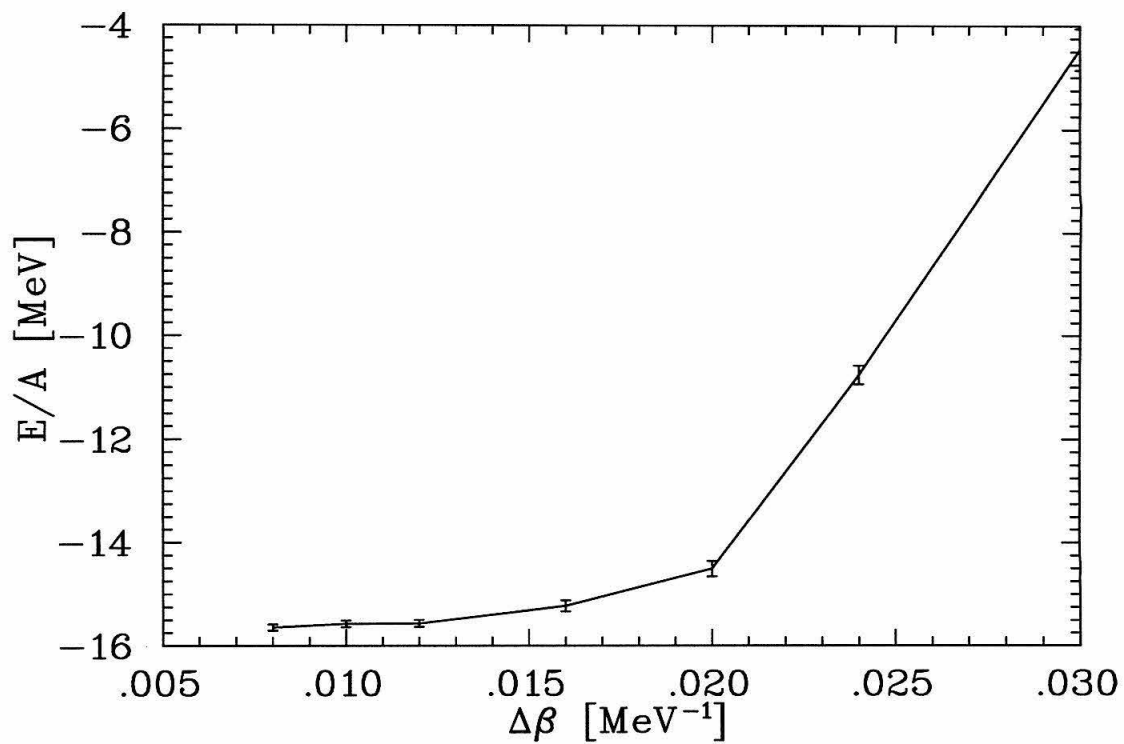
Figure 9.1: Energy per particle E/A as a function of time slice parameter $\Delta\beta$. This example of $\Delta\beta$ extrapolation is taken at $T = 4$ MeV and $\mu = 0$ MeV.
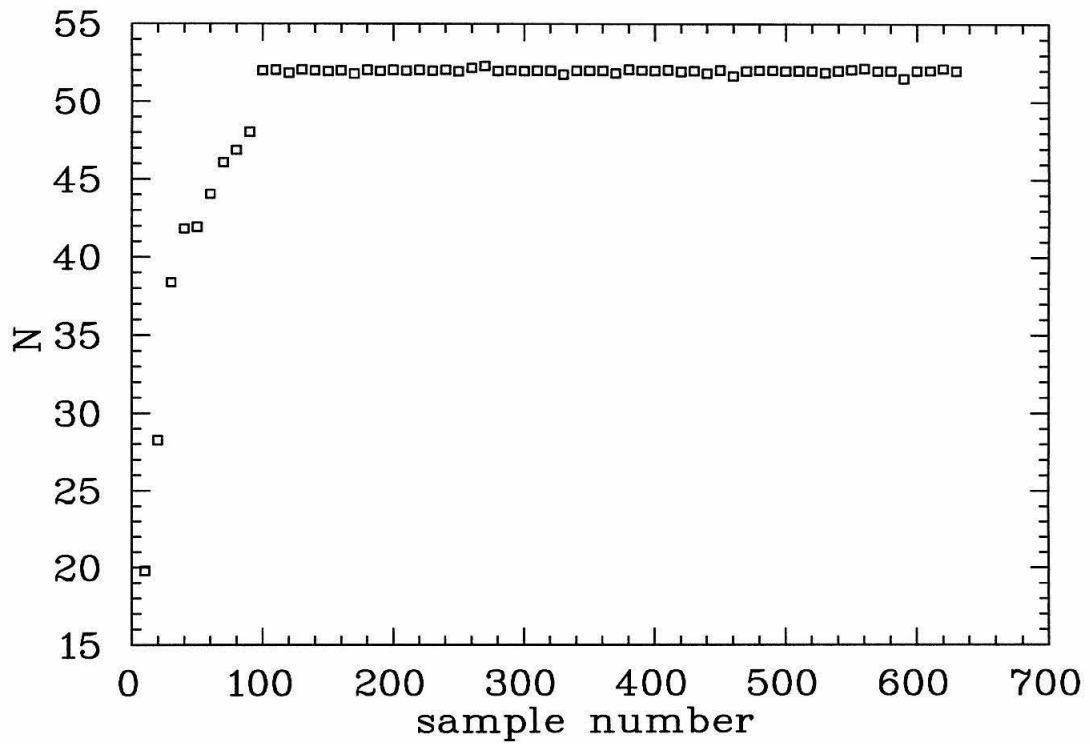
Figure 9.2: Samples of number of particles N as a function of sample number. This graph indicates that after a thermalization of approximately 100 steps the system is equilibrated and measurements can be taken.
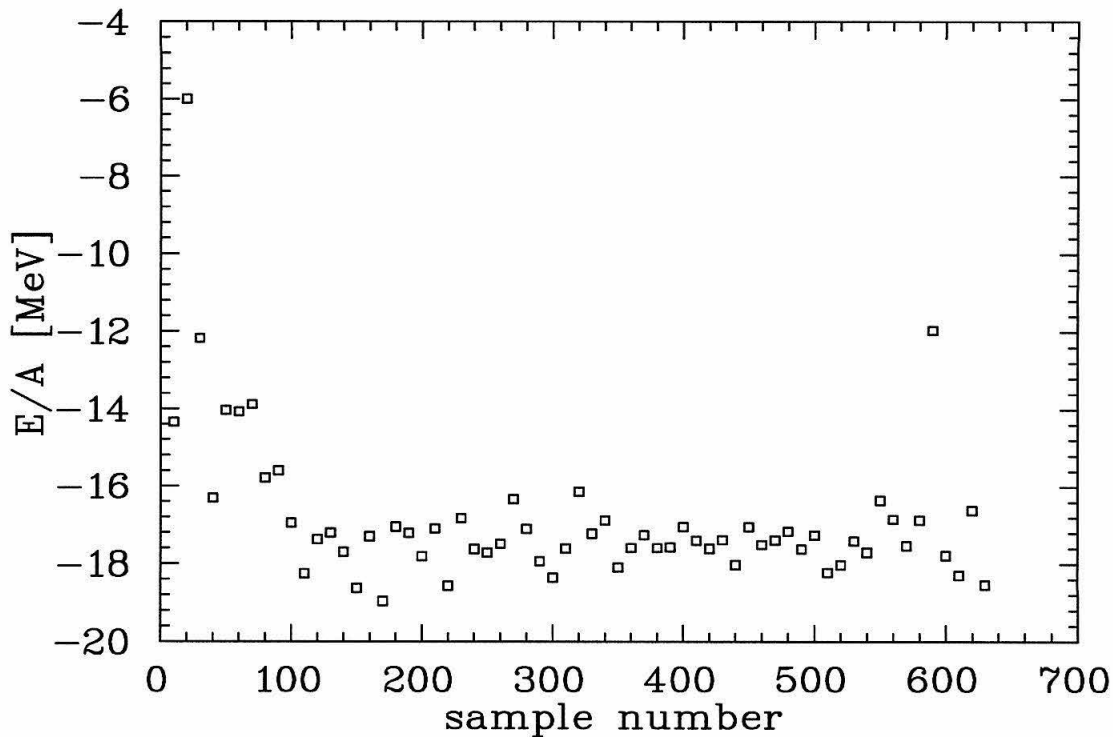
Figure 9.3: Samples of the energy per particle E/A. The scatter of values is larger than for the number of particles N (cf. Fig. 9.2).

of its samples involves many matrix elements (as compared to the particle number, which is just the trace of the density matrix, for example).

This observation can also be made when thermalization of different variables is investigated. In Figs. 9.2 and 9.3 the values of samples of the number of particles N and energy per particle E/A are plotted as a function of sample number, this time for $T = 2.5$ MeV and $\mu = 2.0$ MeV. The scatter in energy is larger than in particle number. This is due to the fact that for the same number of particles different spatial configurations may exist with a very similar energy. Thus, it shows that for a given finite temperature quite a few many-body states may contribute significantly to the partition function and therefore to the expectation value of thermal observables, as expected. Also, note that both graphs show the system to be equilibrated after approximately 100 samples. Therefore, all calculations are prepared by
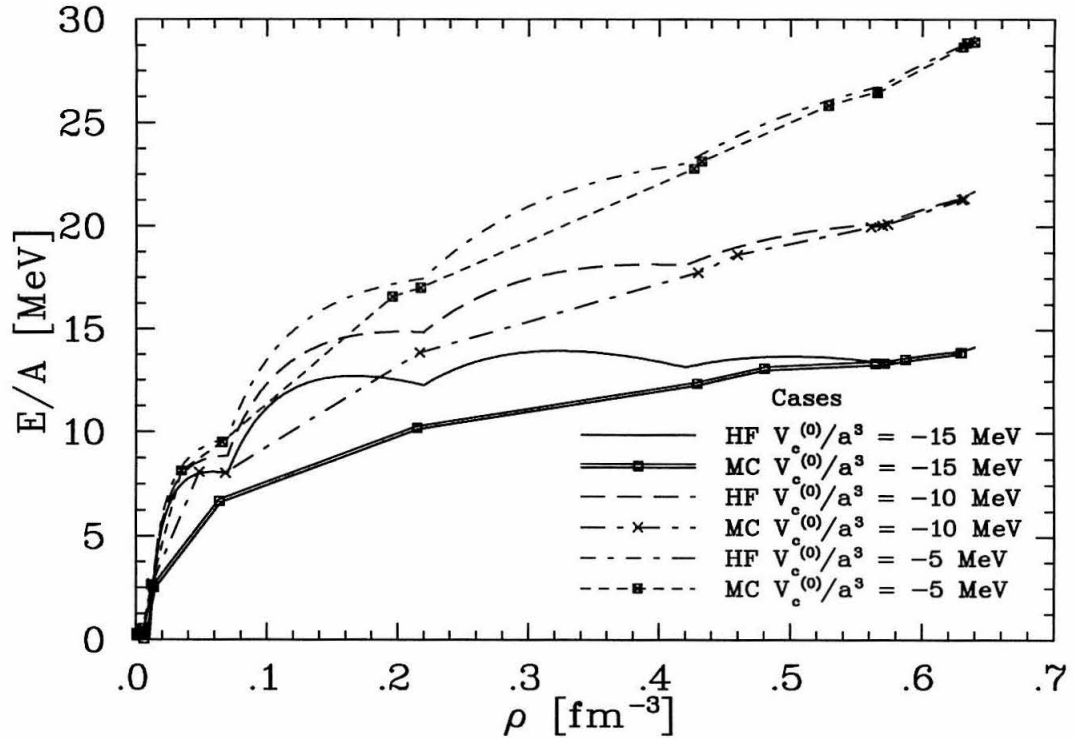
Figure 9.4: Comparison of the Monte Carlo results with the Hartree-Fock approximation for the central on-site interaction, $V_c^{(0)}$. The kinetic parameter for this calculation is $t = 6.1$ MeV.

a pre-thermalization of the system for 100 steps before I took measurement samples. Between measurement samples, 15 de-correlation steps have been taken to guarantee statistical independence of the samples. The autocorrelation of k consecutive samples [54]

$$C_{\mathcal{O}}(k) = \frac{\langle \mathcal{O}_i \mathcal{O}_{i+k} \rangle - \langle \mathcal{O}_i \rangle^2}{\langle \mathcal{O}_i^2 \rangle - \langle \mathcal{O}_i \rangle^2},$$ (9.1)

with i being the summation index over samples, has been monitored for all observables $\mathcal{O}$ and was held below 10%.

While it is easy to diagonalize the kinetic and potential parts of the Hamiltonian separately, a Hartree-Fock calculation should provide a benchmark whether the full code is working and how valid a mean field approximation is which neglects two-body

correlations. The Hartree-Fock equations that have to be solved are

$$
\begin{aligned}
- \ & t\nabla^2 \phi_\alpha\left(x\right)\chi_\alpha\left(\sigma\right) + \sum_{\sigma'}\int \mathrm{d}\vec{y}\sum_\beta \phi_\beta^\dagger\left(\vec{y}\right)\chi_\beta^\dagger\left(\sigma'\right)\phi_\beta\left(\vec{y}\right)\chi_\beta\left(\sigma'\right)\left\{V_c^{(0)}\delta\left(\vec{x}-\vec{y}\right)\right. \\
+ \ & \left.V_c^{(2)}\left(\nabla^2\delta\left(\vec{x}-\vec{y}\right)\right)\right\}\phi_\alpha\left(x\right)\chi_\alpha\left(\sigma\right) - \sum_{\sigma'}\int \mathrm{d}\vec{y}\sum_\beta \phi_\beta\left(\vec{x}\right)\chi_\beta\left(\sigma\right)\phi_\beta^\dagger\left(\vec{y}\right)\chi_\beta^\dagger\left(\sigma'\right) \\
\times \ & \left\{V_c^{(0)}\delta\left(\vec{x}-\vec{y}\right) + V_c^{(2)}\left(\nabla^2\delta\left(\vec{x}-\vec{y}\right)\right)\right\}\phi_\alpha\left(y\right)\chi_\alpha\left(\sigma'\right) = \epsilon_\alpha\phi_\alpha\left(\vec{x}\right)\chi_\alpha\left(\sigma\right) \qquad (9.2)
\end{aligned}
$$

and

$$
E_{HF} = \sum_\alpha \epsilon_\alpha - \frac{1}{2}\sum_{\alpha\beta}\langle\phi_\alpha\chi_\alpha\phi_\beta\chi_\beta|V_c^{(0)}\delta + V_c^{(2)}\left(\nabla^2\delta\right)|\phi_\alpha\chi_\alpha\phi_\beta\chi_\beta - \phi_\beta\chi_\beta\phi_\alpha\chi_\alpha\rangle, \quad (9.3)
$$

where ϕ is the spatial part of the single-particle wave function and χ its spinor. The Hartree-Fock energy E_{HF} is determined by calculating the single-particle energies ϵ_α, occupying the lowest levels and then computing the second part of Eq. (9.3) over all occupied levels $(\alpha\beta)$. The Hartree-Fock results have been calculated with plane waves, $\phi \sim \exp\left(i\vec{k}_\alpha\cdot\vec{x}\right)$ as single-particle states and taking into account the discretization of space ($4\times4\times4$ cube), while the Monte Carlo results are obtained for $T = 2.2$ MeV, which should come close to the ground state energy.

Figs. 9.4 and 9.5 give the results for on-site and next-neighbor interaction separately. They show that for small interaction strength Hartree-Fock and Monte Carlo agree quite well, while for higher strength the values only coincide for very low densities (where the dilute system is barely interacting) and very high densities (where the finite system is running out of model space; at $\rho = 0.64$ fm^{-3} the lattice is full and comprised by just one state). The discrepancy at half filling ($\rho = 0.32$ fm^{-3}) and high interaction strength (i.e. $V_c^{(0)}/\left(a^3 t\right) \approx 2.5$) is due to the fact that the real system deviates from particles occupying plane wave states quite a bit: Indeed, clusters of α-particles are formed instead.

In conclusion, the Hartree-Fock and Monte Carlo results are consistent and give confidence that the Monte Carlo code is working properly. But it also shows that for half-filling a mean field approximation with plane waves as single-particle states and
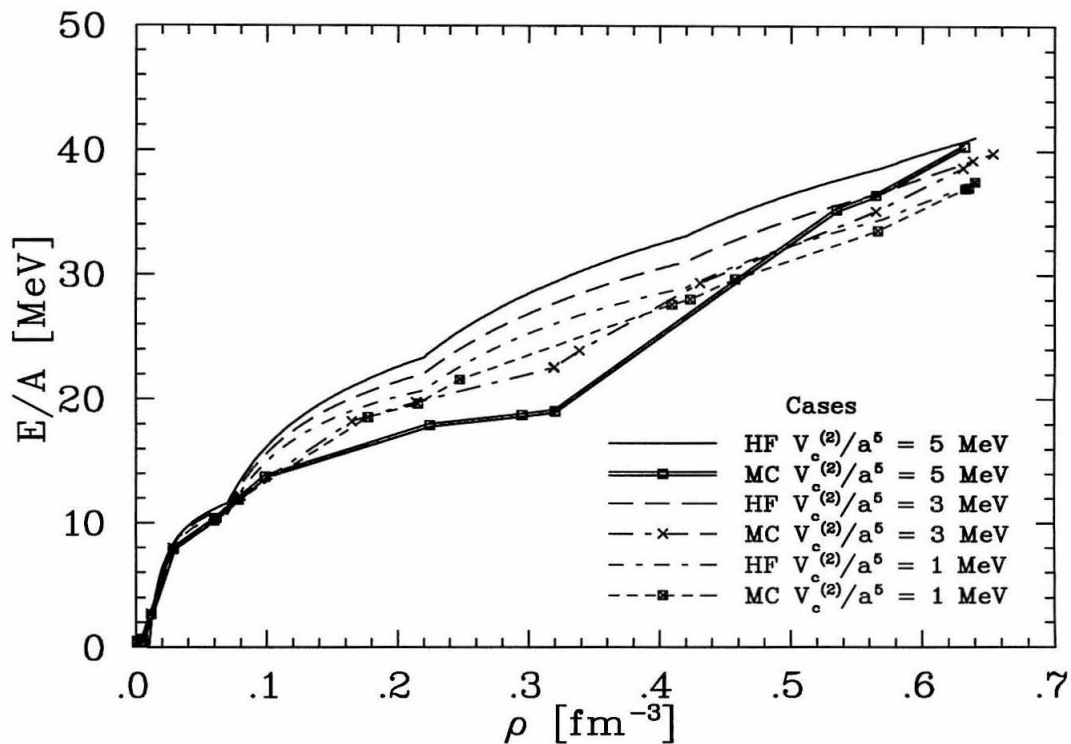
Figure 9.5: Comparison of the Monte Carlo results with the Hartree-Fock approximation for the central next-neighbor interaction, $V_c^{(2)}$. The kinetic parameter for this calculation is $t = 6.1$ MeV.

a strong interaction does not appear to be accurate enough.

9.2 Symmetric Nuclear Matter

9.2.1 Reproduction of the Saturation Curve

The rigorous search in the space of potential parameters included all components of the central part and spin-exchange. The effort focused on reproducing saturation density and energy correctly; a perfect fit over a wide range of densities should not be expected. I am also restricted by the fact that the Monte Carlo simulations cannot be extended to arbitrarily low temperatures. Even though the numerical routines are quite stable, it is not possible to add an arbitrary number of time slices, since it involves more and more matrix multiplications which become increasingly unstable. In the present case I was able to go down to a value of $\beta = 30 \times \Delta\beta = 0.3$ MeV^{-1} without running into numerical instabilities.

Fig. 9.6 shows the best fit I obtained. Several observations can be made:

- With decreasing temperature, the system develops a minimum at $\rho = 0.32$ fm^{-3} first, which is most pronounced between $10 - 14$ MeV, before it shifts to lower densities. At $T = 3.3$ MeV and $T = 5.9$ MeV the minimum is very broad, making matter softer (see also compressibility, Fig. 9.11 below).

- For high temperatures and/or high density, the simulation suffers from the fact that it runs out of model space: At $T = 50$ MeV the system behaves almost like a Fermi gas and the energy per particle should behave like $\sim \rho^{2/3}$. Yet, the curve bends down with a negative slope. Also, for all other temperatures, the curves converges to the energy of the full lattice state, $E/A = 5.96$ MeV, as density increases.

- For low densities the model overbinds if compared to other calculations (see, for example, Refs. [28] and [29]), and saturation is not as dominant at high densities.
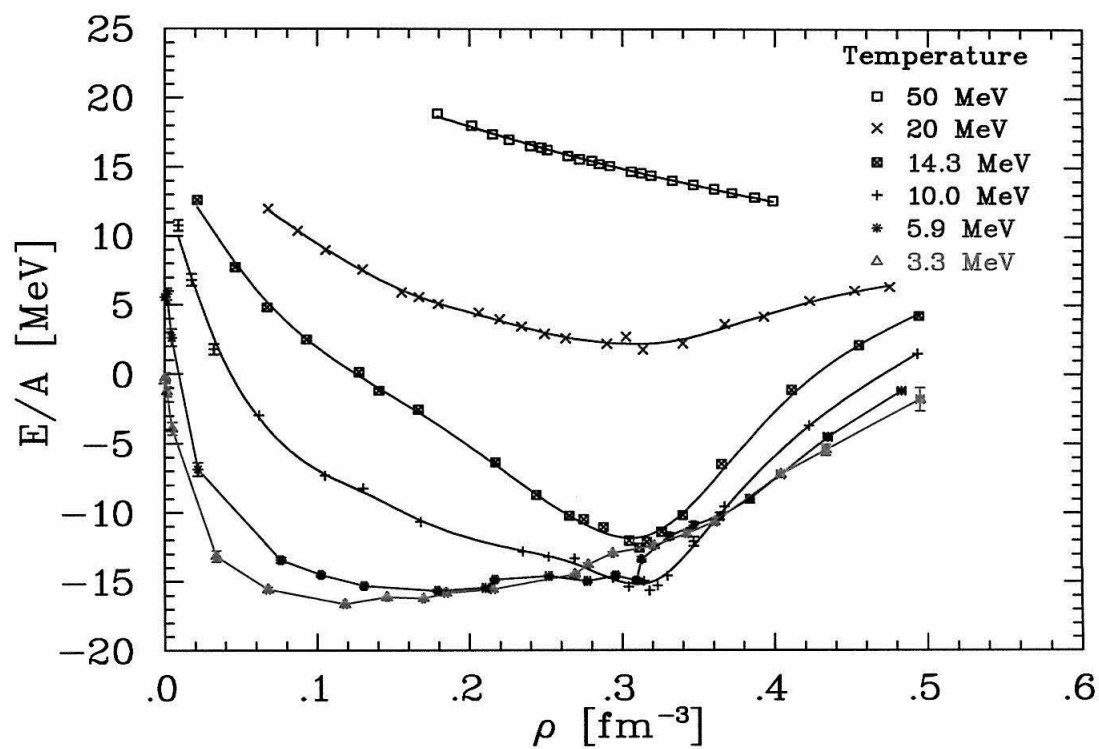
Figure 9.6: E/A for symmetric nuclear matter as a function of density ρ and for different temperatures. The purpose of the lines is to guide the eye.

- At $\rho = 0.32$ fm^{-3}, E/A as a function of temperature has a minimum at $T \approx$ 10 MeV which means that at even lower temperatures E/A increases again. This contradicts intuition because it would mean that the system is in an unphysical state.

The last issue needs further explanation. It seems that the energy per particle is not the correct quantity in order to address the question of stability. Particles fluctuate in and out of the system differently at different temperature, leaving the average number of particle unchanged, but contributing to the two-body part of the Hamiltonian. If, however, the grand potential is plotted (see Fig. 9.7),

$$\Omega\left(\beta, \mu\right) = -T \ln \mathcal{Z}\left(\beta, \mu\right), \tag{9.4}$$

with

$$\ln \mathcal{Z}\left(\beta, \mu\right) - \ln \mathcal{Z}\left(0, \mu\right) = -\int_0^\beta \mathrm{d}\beta' E\left(\beta', \mu\right), \tag{9.5}$$

it turns out to actually be a monotonic function of temperature, with a slight deviation at $\mu = 11.0$ MeV where the negative slope of Ω, the entropy

$$S = -\left(\frac{\partial \Omega}{\partial T}\right)_{\mu, V} \tag{9.6}$$

becomes zero between 10 MeV and 14 MeV and positive again for even lower temperatures. This is a slight anomaly (see also Fig. 9.13) which may have been caused by the onset of numerical instabilities at low temperatures or the fact that the lattice spacing is so big and the number of sites so small that the discretization of space is not accurate enough. The latter can also be concluded if the grand potential of the Fermi gas on the lattice is compared to its counterpart in continuous space, given by

$$\Omega_{\mathrm{Fermi}}\left(T, V, \mu\right) = -\frac{4VT}{\lambda_T^3} f_{5/2}\left(z\right) \tag{9.7}$$

with

$$\lambda_T = \sqrt{\frac{2\pi\hbar^2}{m_N T}}, \tag{9.8}$$
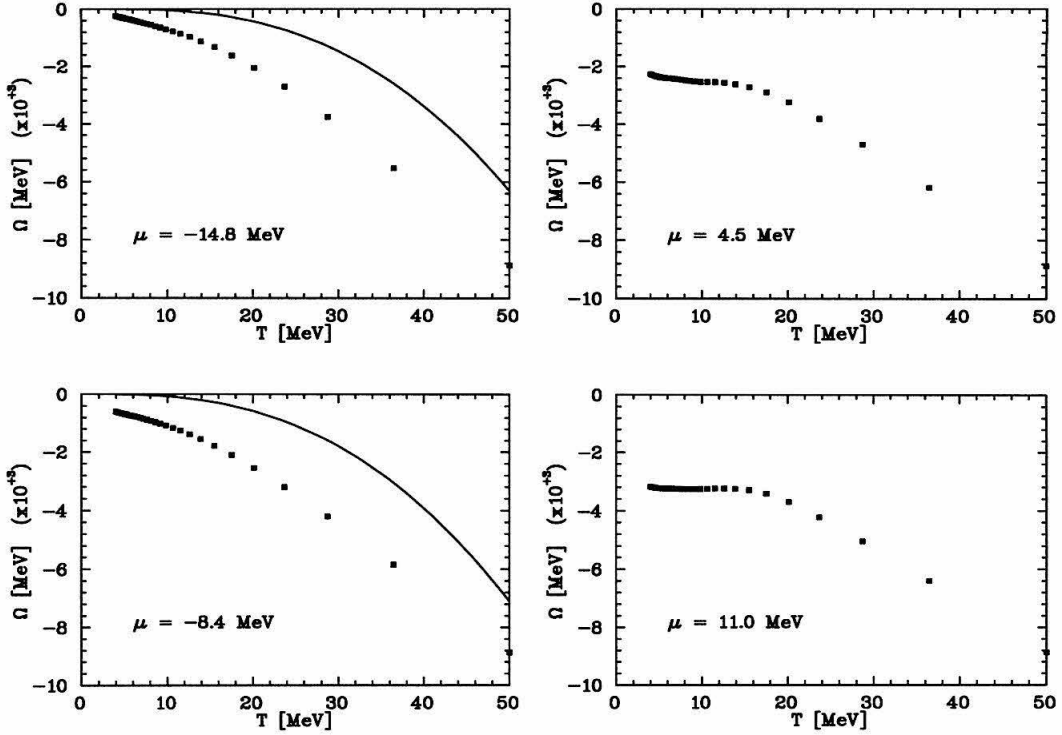
Figure 9.7: Grand canonical potential of symmetric nuclear matter for different chemical potentials μ. The solid lines represent the potential for a noninteracting Fermi gas in continuous space.

$$f_{5/2}(z) = \frac{4}{\sqrt{\pi}} \int_0^\infty \mathrm{d}x\, x^2 \ln\left(1 + ze^{-x^2}\right) \tag{9.9}$$

and

$$z = e^{\beta\mu}. \tag{9.10}$$

This is displayed in Fig. 9.8. There is a significant difference between the two potentials due to the relatively coarse discretization.

In Fig. 9.9 I have plotted the densities at a given chemical potential μ, averaged over all temperatures that measurements were taken with. It shows a monotonic function and helps identify densities with chemical potentials. The error bars are the standard deviations due to averaging. They seem to be smaller around $\rho = 0.32$ fm^{-3} than anywhere else. An independence of the temperature on the density in this region seems to be evident.
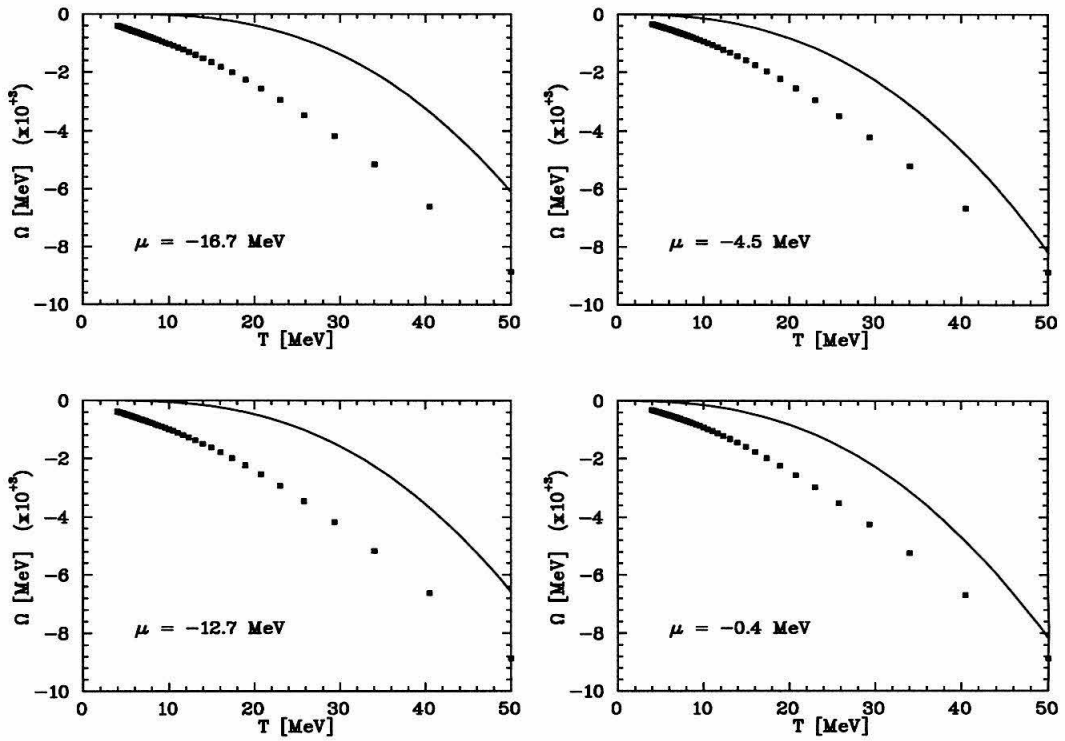
Figure 9.8: Grand canonical potential of a Fermi gas for different chemical potentials μ. The solid lines represent the potential for the continuous space while the squares display the Monte Carlo results of a $4 \times 4 \times 4$ lattice.
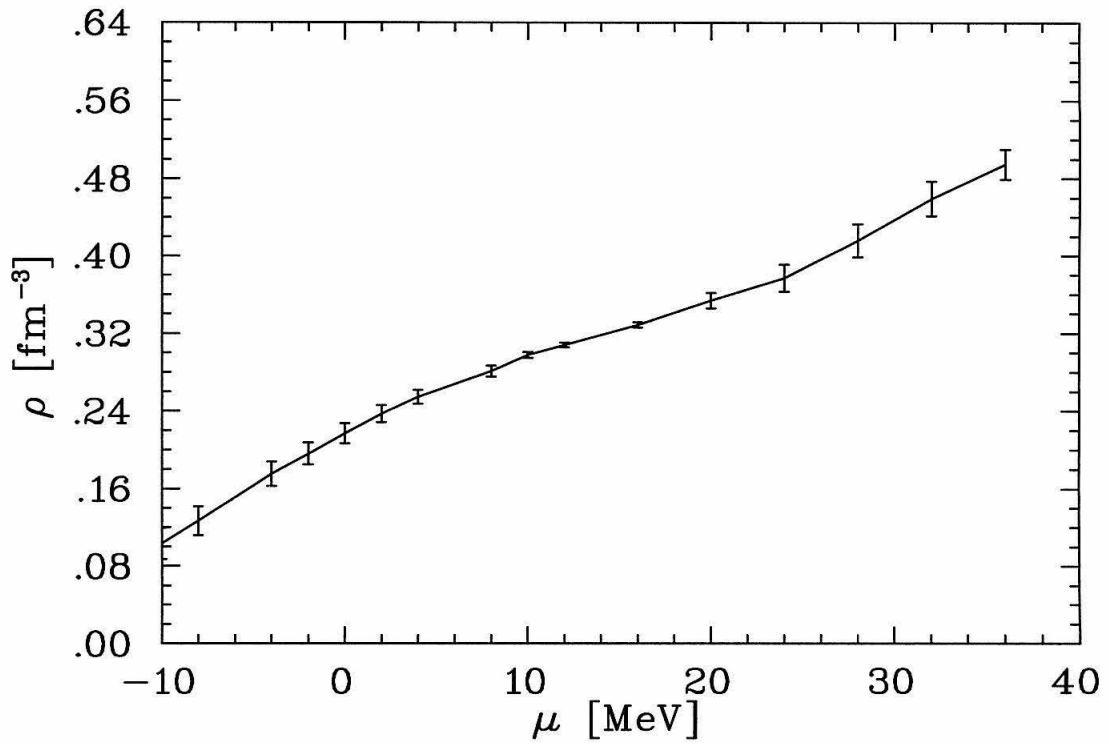
Figure 9.9: Average density for symmetric nuclear matter as a function of chemical potential μ. The average has been taken over all temperature samples and the error bars represent the standard deviation due to this averaging.

9.2.2 First Order Phase Transition

I now introduce several observations which indicate that the system may undergo a first order phase transition towards a clustered system when the temperature is lowered. First, I investigate changes in density with respect to the chemical potential μ. It is well known that they are proportional to particle fluctuations

$$\sigma_N^2 = T \left. \frac{\partial \langle N \rangle}{\partial \mu} \right|_{T,V} \sim T \left. \frac{\partial \rho}{\partial \mu} \right|_{T,V}. \tag{9.11}$$

Such fluctuations are typical for first order phase transitions and indicate that particles move between the two phases without energy cost. For an infinite system, the fluctuations should diverge, but not for a finite system. In the present case, I expect particles building clusters and breaking them up again, so one phase, -the gas phase-, would be that of independent particles, the other one that of clusters. Since I observe the single particle density, σ_N^2 describes the fluctuations in the gas phase. To simplify the graphs, I first fit the data at $T = 100$ MeV to a linear function,

$$f_{\text{fit}} = a_{\text{fit}} + b_{\text{fit}} \times \mu, \tag{9.12}$$

and then subtract this function from all data points of all temperatures in such a manner, defining a function of temperature and chemical potential,

$$f(T, \mu) = \rho(T, \mu) - f_{\text{fit}}. \tag{9.13}$$

This procedure is valid because at $T = 100$ MeV the particles behave like a Fermi gas. The upper panel of Fig. 9.10 shows the outcome of this procedure. I then take the derivative of $f(T, \mu)$ with respect to μ and multiply with T, and this is shown in the lower panel of Fig. 9.10. The fluctuations show a pronounced maximum for $T = 14.3$ MeV and $\mu \approx -8$ MeV, while they are low for $T = 3.3$ MeV and $T = 100$ MeV. The phase transition seems to occur somewhere between $T = 8$ MeV and $T = 20$ MeV.
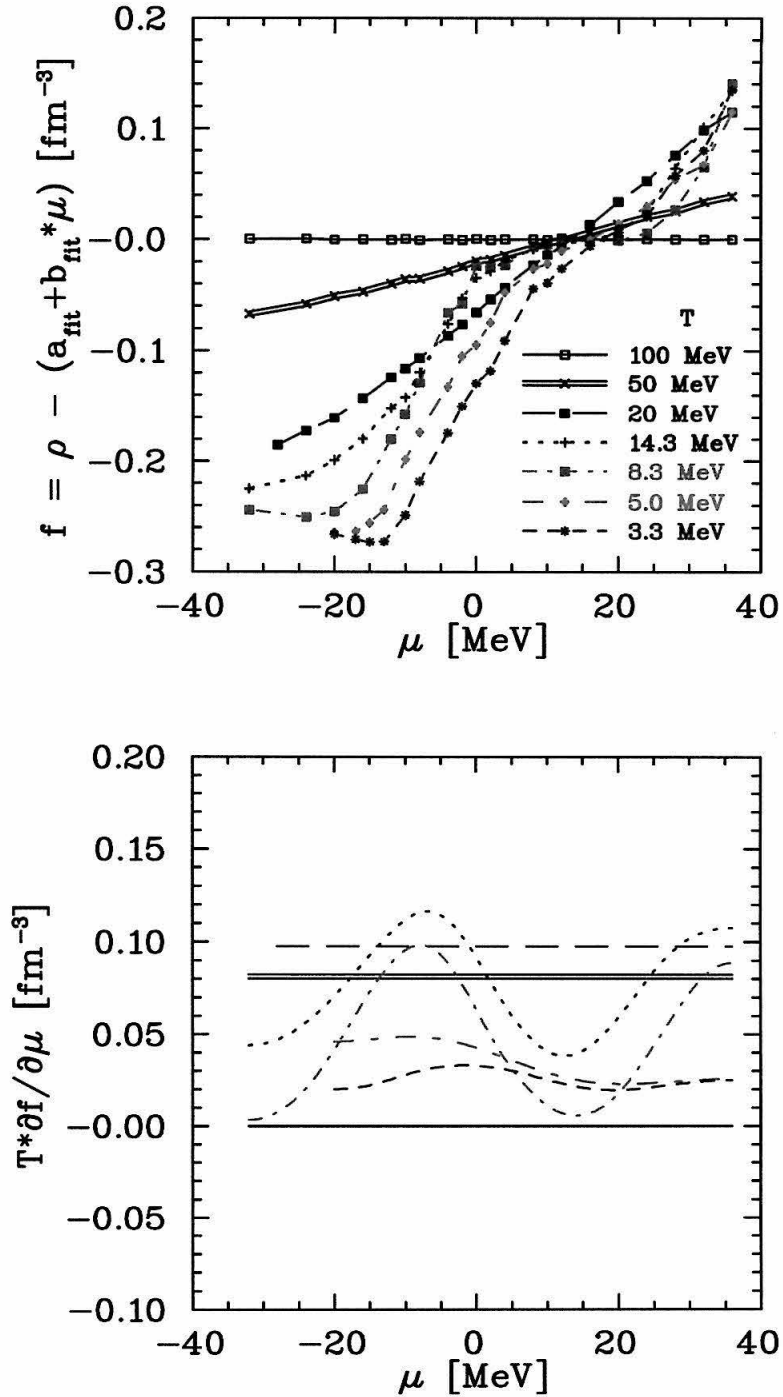
Figure 9.10: Density fluctuations in symmetric nuclear matter. The upper panel displays the modified density f while the lower panel shows the derivatives of f with respect to chemical potential μ which are proportional to the fluctuations.
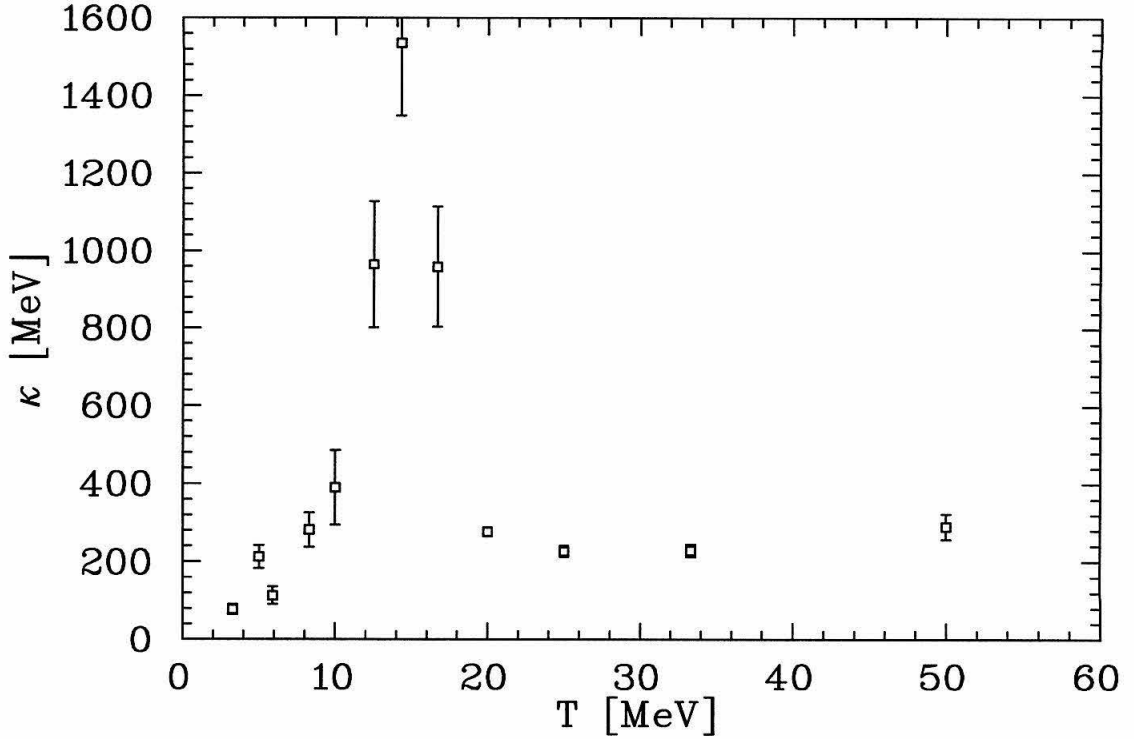
Figure 9.11: Compressibility of symmetric nuclear matter. The minima of the energy curves have been fit to a parabola with a $\chi^2 \leq 1.5$ per degree of freedom.

Another quantity that shows the existence of a transition is the compressibility which is given by

$$\kappa = 9\rho^2 \left. \frac{\partial^2 E/A}{\partial \rho^2} \right|_{\rho=\rho_{\mathrm{sat}}} \tag{9.14}$$

where ρ_{sat} is the saturation density. I have fitted the minima of each energy curve to a quadratic function

$$g\left(\rho\right) = a + b \times \left(\rho - \rho_{\mathrm{sat}}\right)^2 \tag{9.15}$$

and then determined the compressibility as $\kappa = 18\rho_{\mathrm{sat}}^2 \times b$. All data points in Fig. 9.11 were obtained with a χ^2 per degree of freedom of less than 1.5. Again, a maximum in compressibility (which is in fact an incompressibility) is observed at $T \approx 14$ MeV: The clusters that form repel each other through the next-neighbor interaction which is repulsive. At an even lower temperature, matter becomes softer again due to a

broadening of the minima in E/A (cf. Section 9.2.1). As discussed in Section 9.2.3, this is due to the fact that the system becomes more dilute. Note that the values of ρ_{sat} change with temperature.

Finally, I present the heat capacity and entropy of the system. A continuous and infinite system shows a divergence in the heat capacity

$$c_V = \left.\frac{\partial E}{\partial T}\right|_V \qquad (9.16)$$

and a discontinuity for the entropy (with an infinite derivative at T_c),

$$
\begin{aligned}
S\left(\beta, \mu\right) &= \ln \mathcal{Z} + \beta \langle H\left(\beta, \mu\right)\rangle \\
&- \beta\mu \langle N\left(\beta, \mu\right)\rangle, \qquad (9.17)
\end{aligned}
$$

as displayed in Fig. 9.12. For a finite system only a maximum in the heat capacity is expected, and a relatively sharp drop in entropy with decreasing temperature. Both facts can be verified in Fig. 9.13: The heat capacity suggests a critical temperature of $T_c = 15$ MeV, as does the entropy. For the graphs of entropy one has to keep in mind that the system investigated is quite small (it is a $4 \times 4 \times 4$ lattice only), but two lev-

Figure 9.12: Schematic graphs of a first order phase transitions. The upper panel shows the heat capacity, the lower one the entropy of an infinite and continuous system.

els, $S \approx 75$ from $T = 5$ MeV to $T = 12$ MeV and $S \approx 175$ from $T = 20$ MeV to $T = 30$ MeV with a steep decrease in between, can definitely be identified. To show that this is indeed a first order phase transition, the calculation has to
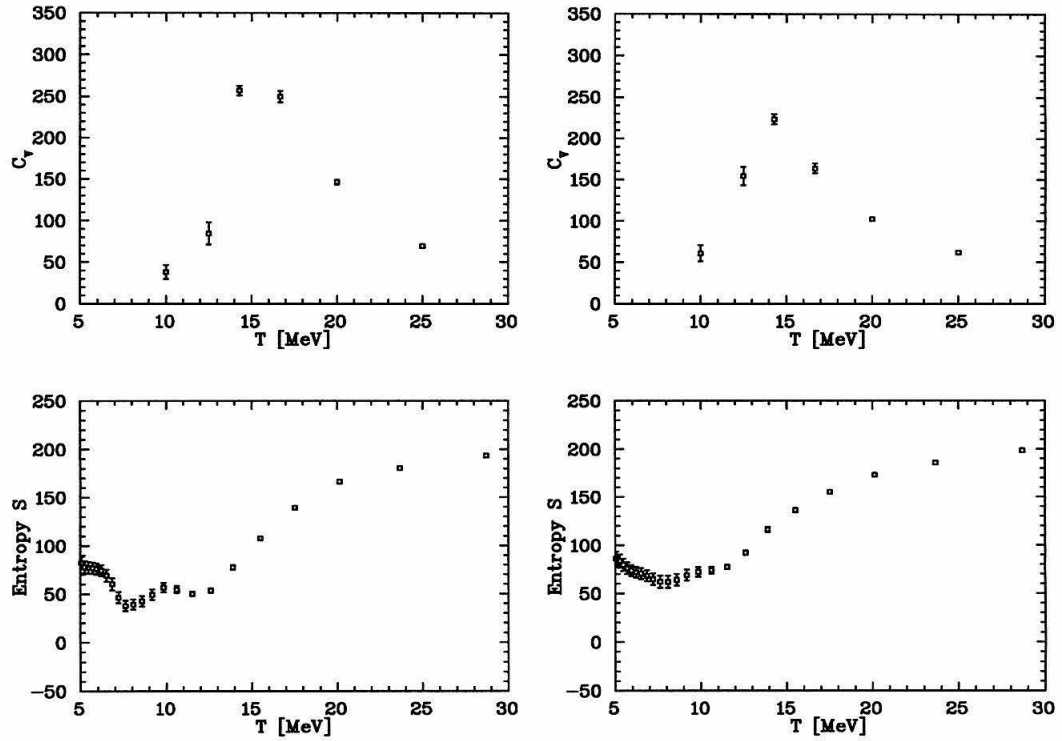
Figure 9.13: Heat capacity and entropy for a finite piece of matter. The two graphs on the left show the case $\mu = 0.0$ MeV, the right ones for $\mu = 4.0$ MeV. The heat capacity (upper panels) shows a distinct maximum, the entropy (lower panels) a relatively sharp drop with decreasing temperatures.

be repeated for a larger number of lattice sites, and then it has to be demonstrated that the drop between the two levels becomes steeper and steeper, finally resulting in a step-like function. This will have to be left for a future project. The anomaly below $T = 10$ MeV has been addressed in Section 9.2.1, when I discussed the grand potential. However, this quantity shows a qualitative behaviour at $\mu = 11$ MeV that is expected for a phase transition (cf. Fig. 9.7). The infinite system has a kink (the derivative is not continuous) in the grand potential at the critical temperature as illustrated in Fig. 9.14. Consequently, all quantities consistently suggest a phase transition at a critical temperature of $T_c \approx 15$ MeV.

9.2.3 Two-Body Correlations in Symmetric Nuclear Matter

The correlation function (Eq. (8.55)) should now give insight into the question what kinds of clusters are formed. Since there is no isospin dependence in SNM, I only refer to spin-up ($\sigma = +\frac{1}{2}$, $\uparrow$) or spin-down ($\sigma = -\frac{1}{2}$, $\downarrow$), and the spatial distance is just abbreviated in terms of lattice points, $z = 0, 1, 2, 3$. Note that $C_{\uparrow\uparrow}(z) = C_{\downarrow\downarrow}(z)$ as well as $C_{\uparrow\downarrow}(z = 1) = C_{\uparrow\downarrow}(z = 3)$.

Figure 9.14: Schematic graph of the grand potential for a first order phase transition. The infinite system exhibits a kink at the critical temperature.

The following scenario seems to emerge from the correlation graphs, which are shown in Figs. 9.15 to 9.19 as a function of density for different temperature: At $\rho = 0.32$ fm^{-3} (half-filling) α-clusters are being formed as the temperature is decreased ($20 \rightarrow 8$ MeV), and every other site is unoccupied. In this range of temperature, $C_{\uparrow\downarrow}(2)$ and $C_{\downarrow\downarrow}(2)$ are at a maximum, while the next-neighbor corre-
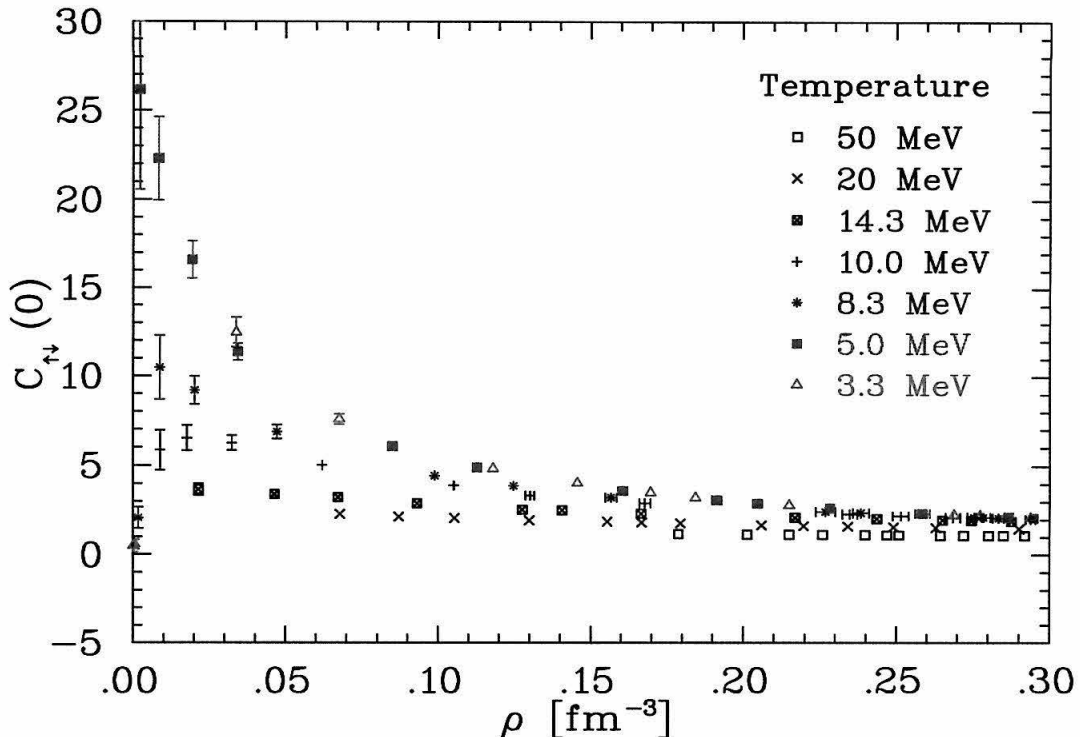
Figure 9.15: Two-body correlation function $C_{\uparrow\downarrow}(0)$ as defined in Eq. (8.55).

lation, $C_{\uparrow\downarrow}(1)$ and $C_{\downarrow\downarrow}(1)$, are suppressed. For lower temperatures, $C_{\uparrow\uparrow}(2)$ seems to become a little smaller, while $C_{\uparrow\uparrow}(1)$ is less suppressed. At $\rho = 0.16\,\mathrm{fm}^{-3}$, there is no next-neighbor suppression at high temperature, but again, at low temperature there seem to be no nucleon at the next-neighbor site. Since the lattice is quarter-filled, two nucleons have to occupy one site. Note that $C_{\uparrow\downarrow}(2)$ and $C_{\downarrow\downarrow}(2)$ deviate only slightly from the Fermi-gas value ($C(2) = 1$) at $\rho = 0.16\,\mathrm{fm}^{-3}$, indicating an absence of α-clusters in a more dilute system. The fact that the correlation is only slightly suppressed (see $T = 3.3$ MeV) may be a sign that there is a majority of di-nucleons with a small admixture of α-particles. Possibly, the spin-exchange contribution of the potential could be responsible for this behaviour. Since the lattice is so small the nucleons are forced to be packed as α-particles at half-filling, in order to avoid the repulsive next-neighbor interaction and taking the penalty of a repulsive on-site spin-exchange (the nucleons are coupled to total spin $S = 0$). At quarter-filling,
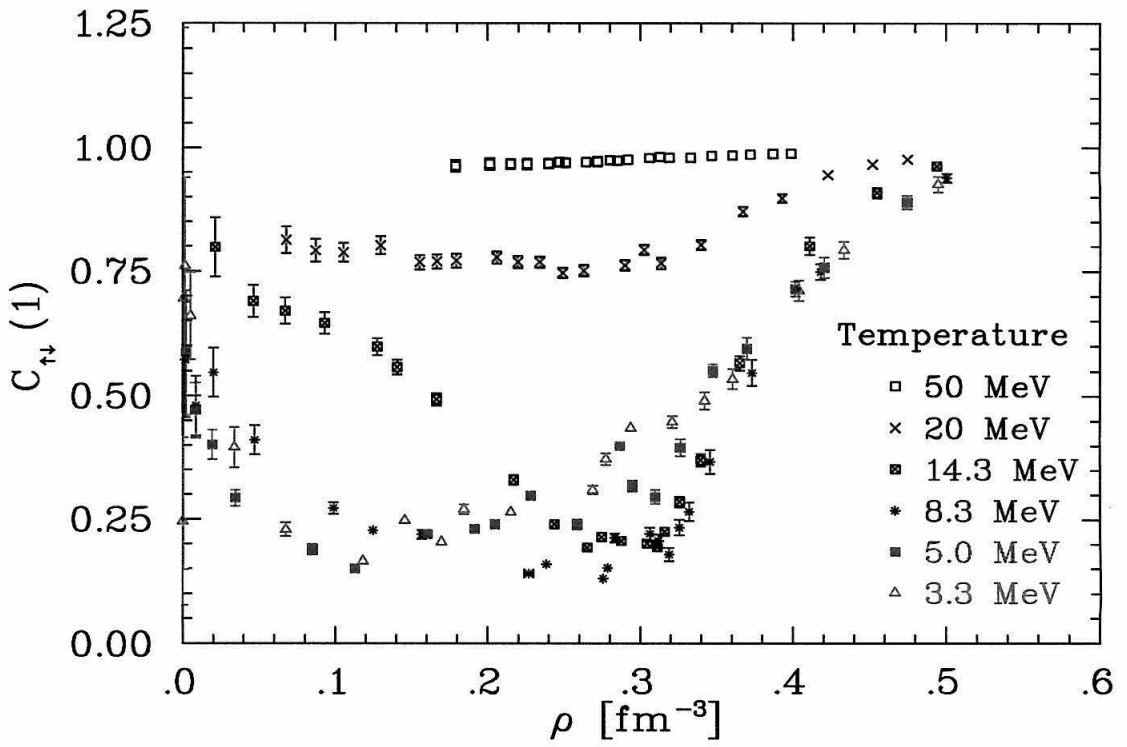
Figure 9.16: Two-body correlation function $C_{\uparrow\downarrow}(1)$ as defined in Eq. (8.55).
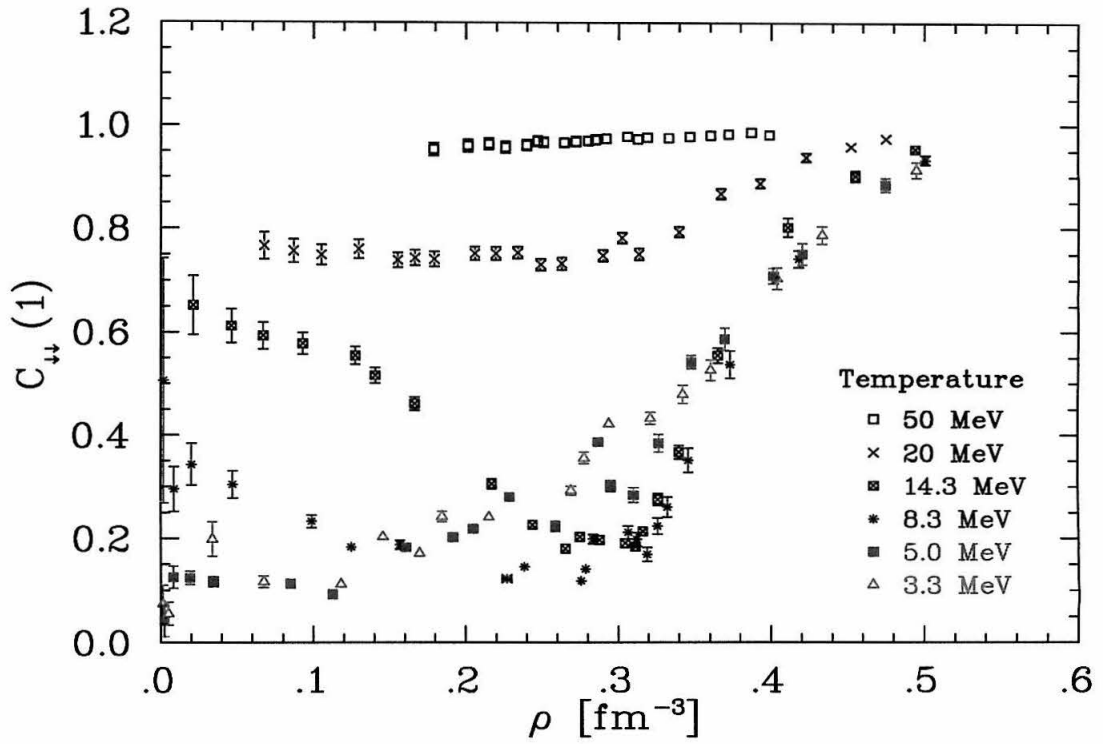
Figure 9.17: Two-body correlation function $C_{\downarrow\downarrow}(1)$ as defined in Eq. (8.55).
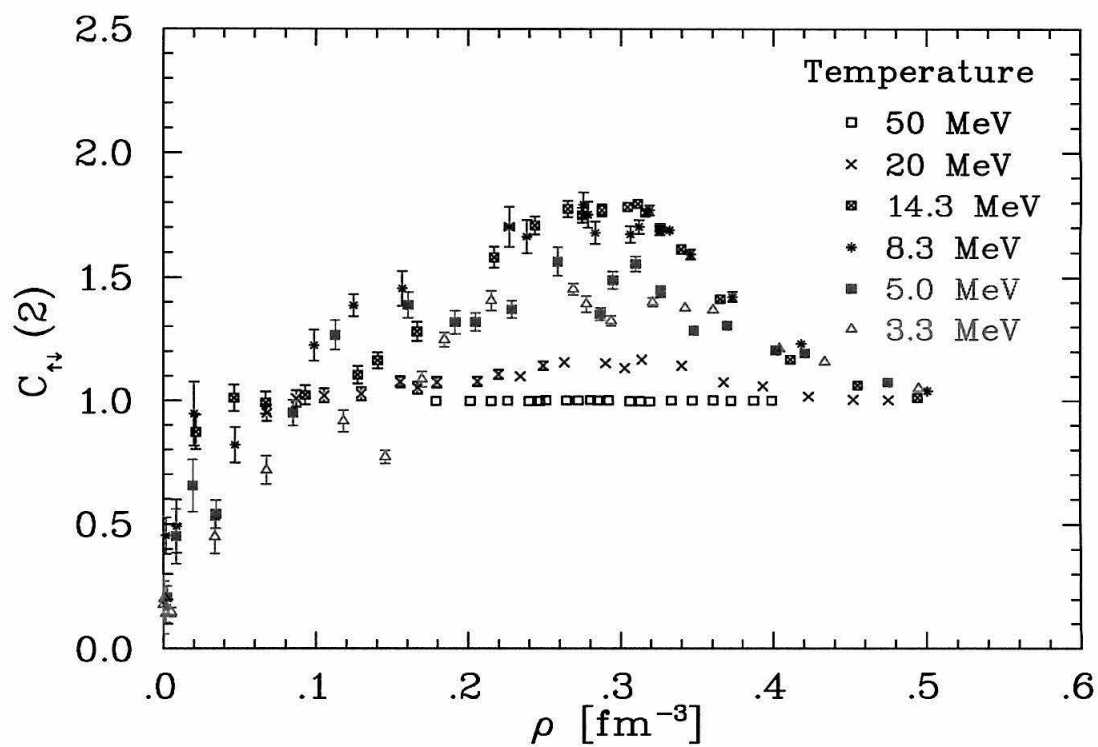
Figure 9.18: Two-body correlation function $C_{\uparrow\downarrow}(2)$ as defined in Eq. (8.55).
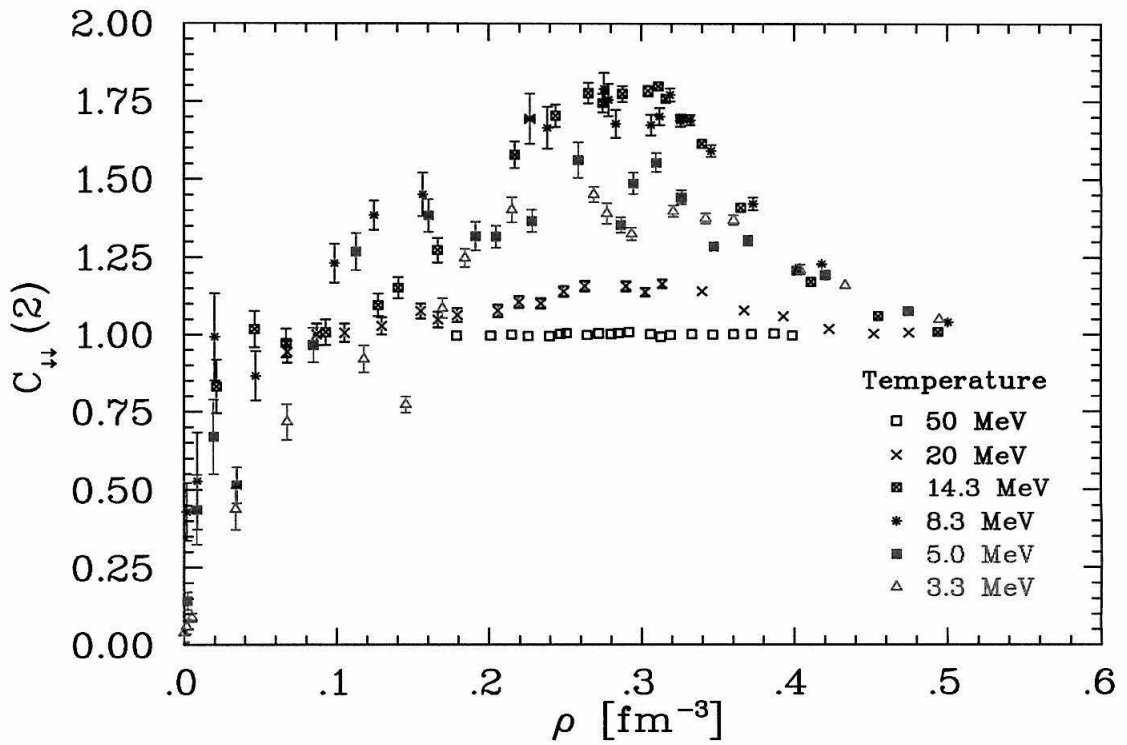
Figure 9.19: Two-body correlation function $C_{\downarrow\downarrow}(2)$ as defined in Eq. (8.55).

the next-neighbor and the spin-exchange repulsion can be avoided which leads to di-nucleons at every other site.

In general, the caution has to be made that the small number of lattice sites in each spatial direction in connection with the periodic boundary conditions may influence the interpretation of correlation functions quite a bit.

9.2.4 Other Observations

In this section, I calculate a number of additional observables and compare them with other calculations found in the literature. The symmetry energy, which appears as a coefficient a_{sym} in the semi-empirical mass formula

$$\frac{E_{sym}}{A} = a_{sym}\frac{(N - Z)^2}{A^2},\tag{9.18}$$

is plotted in Fig. 9.20. I used the energy per particle of pure neutron matter (PNM) and SNM, subtracted them and interpolated the result on a mesh. Since the error bars for pure neutron matter are larger for low temperatures (see Section 9.3), the graphs should be viewed with caution. Nevertheless it appears that the symmetry energy is increasing with density and decreasing with temperature, as one would expect. Indeed, at high temperature SNM and PNM both are more like a Fermi gas, and only at low temperatures do they become different. The observed dependence on density can be explained by the fact that a dilute system is barely interacting while the probability of clustering increases with density. At saturation density and low temperature, I obtain a coefficient of

$$a_{sym} \approx 38 \pm 3 \text{ MeV},\tag{9.19}$$

which is not too different from the generally accepted value [60] of $a_{sym} = 28.1$ MeV. This discrepancy is in part due to the fact that the calculations for pure neutron matter have not converged completely (see Section 9.3).

The first sound velocity has been calculated using the formalism of relativistic
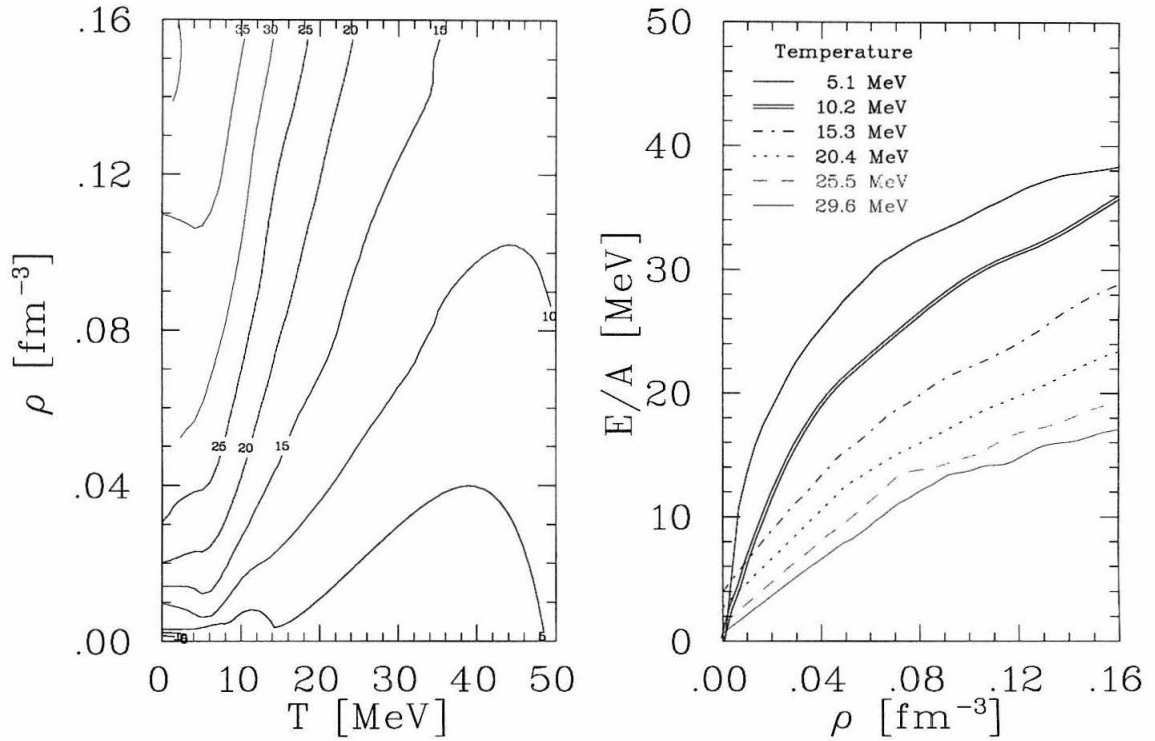
Figure 9.20: Symmetry energy for symmetric nuclear matter as a function of density and temperature. Shown is the coefficient a_{sym} of the semi-empirical mass formula. The left panel shows a contour plot, the right one shows one-dimensional cross sections of it at different temperatures. a_{sym} is increasing with density and decreasing with temperature.
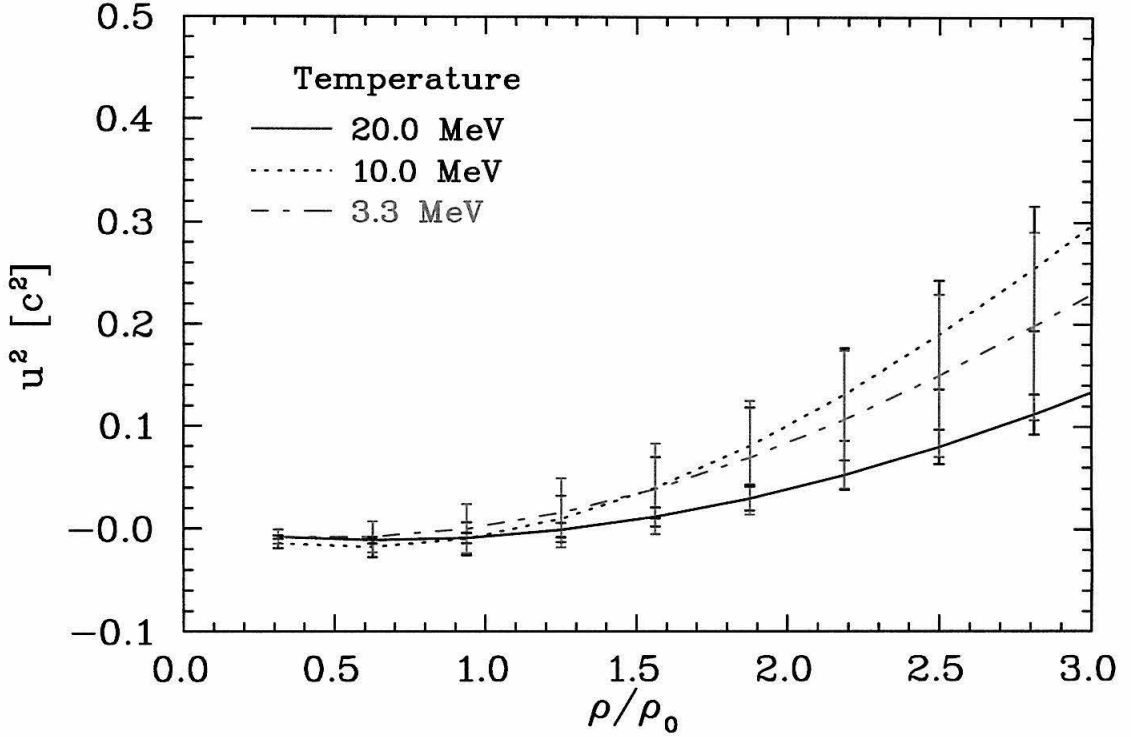
Figure 9.21: First sound velocity for symmetric nuclear matter. The temperature dependence of the speed corresponds to the compressibilities as shown in Fig. 9.11.

fluid dynamics:

$$u/c = \sqrt{\left.\frac{\partial p}{\partial e}\right|_S} \qquad (9.20)$$

$$e = \rho \times \left(m_N c^2 + \frac{E}{A}\right) \qquad (9.21)$$

$$p = \rho^2 \left.\frac{\partial E/A}{\partial \rho}\right|_S . \qquad (9.22)$$

Several calculations [28, 57] show a violation of causality at a few multiples of the saturation density. My result (Fig. 9.21) shows the correct temperature dependence in the sense that it conforms with the compressibility: higher sound speed for intermediate temperatures (high incompressibility) and lower speeds for both low and high T. In general, the first sound I obtain is too low compared to Ref. [28, 57], but the velocities are of the same order of magnitude.
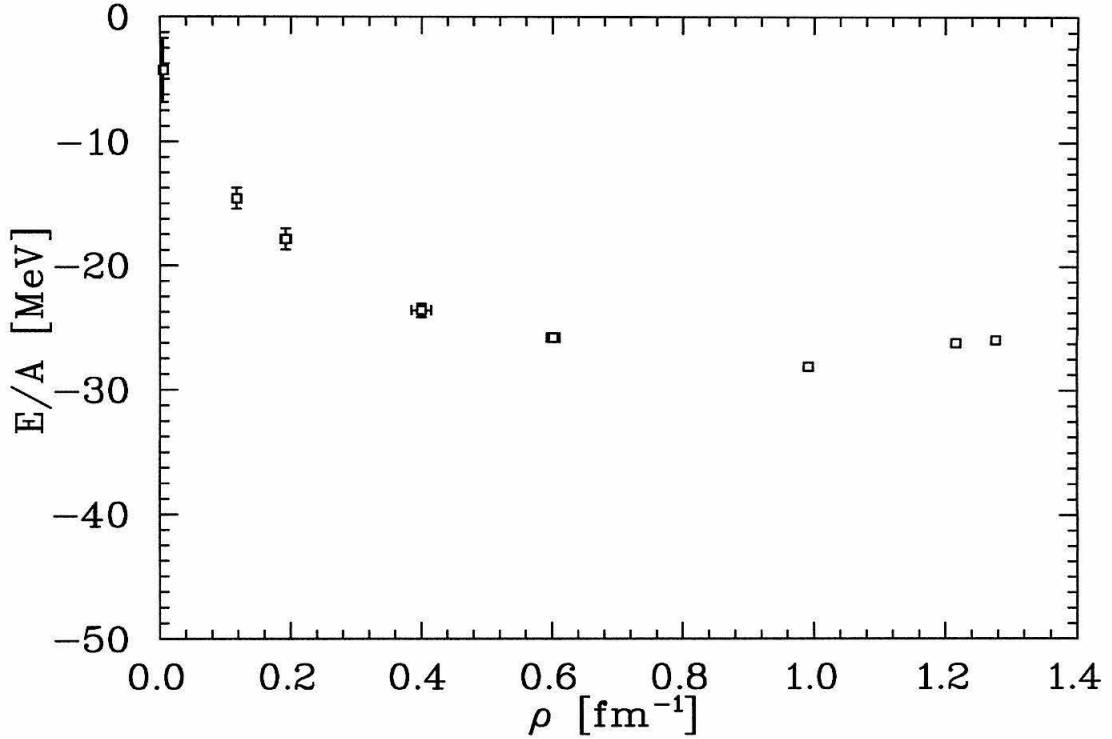
Figure 9.22: Energy per particle for one-dimensional symmetric nuclear matter.

Finally, I calculated the energy curves for one-dimensional symmetric matter using the same potential parameters obtained from the fit of three-dimensional matter. Serot et al. [58] performed a Monte Carlo calculation which included dynamical degrees of freedom like scalar and vector mesons. My result (Fig. 9.22) of $E/A \approx -28$ MeV yields the correct saturation density of $\rho \approx 0.9$ fm^{-1} and a better energy than the Hartree calculation of Ref. [58] (by 13 MeV), but it is worse than the Hartree-Fock or the dynamical calculation (by $12 - 14$ MeV) of that reference.

9.3 Pure Neutron Matter

As mentioned in Section 8.2.4, the sign problem makes it quite difficult to obtain numerical results for PNM. In the case of SNM the evolution operator decomposes into two submatrices **M** that are identical, such that the weight is always the square
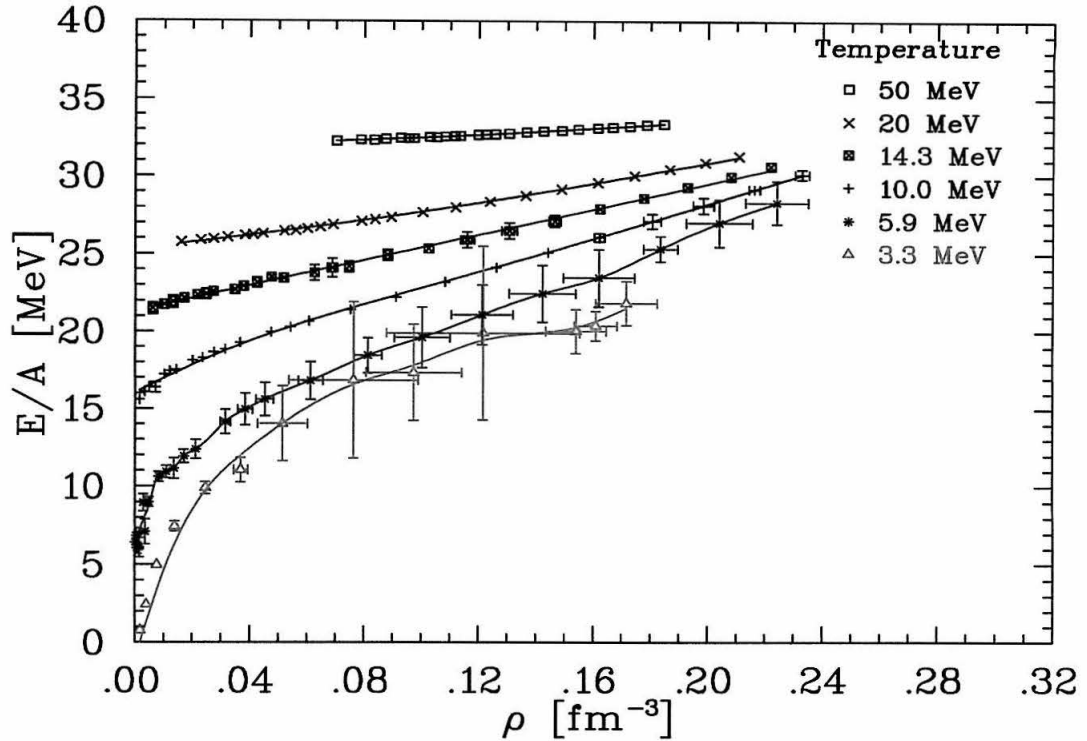
Figure 9.23: Energy per particle for pure neutron matter.

of the trace of $1 + \mathbf{M}$ and therefore positive definite. For PNM, the weight in the Monte Carlo calculation is just the trace of $1 + \mathbf{M}$, and the sign problem appears.

As a potential, I used the parameters obtained from the fit to symmetric nuclear matter, as described in Section 9.2.1. Fig. 9.23 shows the energy per particle for this case. Note that the slopes of the curves at high temperatures are not negative as it has been for SNM. Clearly, I cannot conclude that the energies at $T = 3.3$ MeV have converged to that of the ground state because the curve differs quite a bit from that of $T = 5.9$ MeV. At the lowest temperature they are $4 - 5$ MeV higher than those of the ground state as calculated in Ref. [28], but the general shape of the curve is very similar. This is no surprise, since PNM is like a Fermi gas, with more attractive forces interacting between the neutrons, lowering the energies with respect to the non-interacting system. The error bars at $\rho = 0.16$ fm^{-3} (half-filling) are smaller than at other densities, and there seems to be a local minimum, suggesting some kind of an

ordered or clustered system. Nevertheless, the search for any kind of phase transition in the range of $5 - 50$ MeV was to no avail. It is likely that a phase transition occurs at lower temperature.

Chapter 10 Summary and Conclusion

This project has produced some promising results which should be viewed as a starting point to a successful description of infinite nuclear matter on the lattice. In a model with a relatively simple Hamiltonian, and further limited by a very small lattice, I was able to reproduce saturation properties of symmetric nuclear matter. Deviations in the general density-energy curve still exist. Furthermore, I presented evidence in the form of mechanical and thermodynamical observables which support the existence of a phase transition from an uncorrelated Fermi gas to a clustered system; particle fluctuations of the gas phase seem to reach a maximum at $T \approx 14$ MeV. The heat capacity and compressibility also have a maximum at around this temperature. Entropy and grand potential show a behaviour as it is expected for a first order phase transition. While it looks more like a solid-gas than a liquid-gas transition, the small lattice prohibits an accurate analysis of this question. Other quantities like symmetry energy and first sound velocity show reasonable agreement with other calculations. Lastly, a survey of pure neutron matter (PNM) shows that the current status of the project has not proceeded far enough to describe it accurately, and the search of a phase transition in PNM failed: The energy calculations at finite temperature (spoiled by increased statistical errors) cannot be brought down to temperatures low enough that a ground state can be confirmed.

Even though the model, because it is an exact treatment taking first steps towards a more realistic Hamiltonian, is an improvement compared to previous calculations, it can be extended to include more Physics, and details in the algorithm can be improved. First of all, more computer power is necessary to get rid of finite size effects. A lattice of $10 \times 10 \times 10$ points would be desirable, and also the imaginary time dimension could be pushed further. This requires stable matrix techniques. The present code can handle 30 time slices comfortably using commonly *known sparse* matrix techniques. But, as the lattice spacing decreases, one needs to go to larger

imaginary time to separate the ground state from excited states. At the same time it is not possible to increase $\Delta\beta$ as it would induce finite time effects. Therefore, an improved effective matrix algorithm would be needed to allow for more matrices to be multiplied. Along with a bigger lattice, the number of points the potential is represented with should increase, resulting in next-to-nearest-neighbor and further interactions. This extension of the spatial dependence of the potential can easily be accomplished and is only restricted by computational power. Such an extension would also put a regularization scheme as described in Section 8.3 on firmer ground.

Another big hurdle is the sign problem. The solution to this obstacle will result in a huge advancement in many areas of computational Physics and Chemistry. Rom et. al. [61] have made some progress which could prove beneficial for the model described here too: it basically consists of shifting the contour of the auxiliary field integrals which is equivalent to subtracting a mean field from the problem. Unfortunately, the present project had advanced too much already that a more rigorous investigation of this method and its application to nuclear matter could have been attempted.

The Physics of nuclear matter itself is certainly more involved than the current model can account for. Mesons are not included as explicit degree of freedom, and the various exchanges are only simulated indirectly through the choice of potential and its parameters, very much like in AV18 or other potentials. Realizing that the auxiliary fields behave like massless bosons, one could ponder how a Monte Carlo procedure would look like that includes one- or two-meson exchange directly. Such a procedure could be quite similar to already established auxiliary field Monte Carlo procedures. There may be a way to connect two auxiliary fields that couple to different nucleons without returning to a plain two-body operator, simulating a meson exchange.

It has been stated that three-body and higher-order many-body forces are important to describe saturation properties of nuclear matter correctly. However, incorporating these forces in a Monte Carlo calculation is currently impossible, basically because there is no scheme to reduce higher-order forces to the single particle formalism. As long as such a scheme is not available, an approximation could be established on top of this two-body calculation that incorporates higher-order effects. A first at-

tempt would be to calculate the three-body contribution to the energy obtained from the one-body densities of this Monte Carlo calculation and a given three-body Hamiltonian.

Bibliography

[1] R.E. Prange, in *The Quantum Hall Effect*, edited by R.E. Prange and S.M. Girvin, Springer-Verlag, New York, 1987.

[2] A. Kumar, S.E. Laux, and F. Stern, Phys. Rev. B **42**, 5166 (1990).

[3] P.L. McEuen, E.B. Foxman, U. Meirav, M.A. Kastner, Y. Meir, and N.S. Wingreen, Phys. Rev. Lett. **66**, 1926 (1991).

[4] V. Fock, Z. Phys. **47**, 446 (1928).

[5] C.G. Darwin, Proc. Cambridge Philos. Soc. **27**, 86 (1931).

[6] B.L. Johnson and G. Kirczenow, Phys. Rev. B **47**, 10563 (1993).

[7] P.A. Maksym, Physica B **184**, 385 (1993).

[8] A.H. MacDonald, S.R. Eric Yang, and M.D. Johnson, Aust. J. Phys. **46**, 345 (1993).

[9] C. de C. Chamon and X.G. Wen, Phys. Rev. B **49**, 8227 (1994).

[10] S. Tarucha, D.G. Austing, T. Honda, R.J. van der Hage, and L.P. Kouwenhoven, Phys. Rev. Lett. **77**, 3613 (1996).

[11] F. Bolton and U. Rössler, Superlatt. Microstruct. **13**, 139 (1992).

[12] G.C. Wick, Phys. Rev. **80**, 268 (1950).

[13] D. Pfannkuche, V. Gudmundsson, and P. A. Maksym, Phys. Rev. B **47**, 2244 (1993).

[14] F. Bolton, Sol. St. Elec. **37**, 1159 (1994).

[15] H.-M. Müller and S.E. Koonin, Phys. Rev B **54**, 14532 (1996).

[16] J.A. Carlson and R.B. Wiringa in *Computational Nuclear Physics 1*, edited by K. Langanke, J.A. Maruhn and S.E. Koonin, Springer-Verlag, Berlin, 1991.

[17] N. Metropolis, A.W. Rosenbluth, M.N. Rosenbluth, A.H. Teller, and E. Teller, J. Chem. Phys. **21**, 1087 (1953).

[18] P. Ring and P. Schuck, *The Nuclear Many-Body Problem*, Springer-Verlag, Heidelberg, 1980, p 466ff.

[19] A. Kamlah, Z. Phys. **216**, 52 (1968).

[20] C. Kittel and H. Kroemer, *Thermal Physics*, W. H. Freeman and Company, New York, 1980, p 63.

[21] N. Qureshi, J.S. Scott, S.J. Allen, Jr., M. Reddy, M.J.W. Rodwell, Y. Nakamura, I. Tanaka, T. Noda, I. Kamiya, and H. Sakaki, Physica E **2**, 701 (1998).

[22] K.A. Brueckner, Phys. Rev. **97**, 1353 (1955).

[23] H.A Bethe and J. Goldstone, Proc. Roy. Soc. (London) **A238**, 551 (1957).

[24] J. Goldstone, Proc. Roy. Soc. (London) **A239**, 267 (1957).

[25] C.F. von Weizsäcker, Z. Phys. **96**, 431 (1935).

[26] H.A. Bethe and R.F. Bacher, Rev. Mod. Phys. **8**, 82 (1936).

[27] A.D. Jackson, Ann. Rev. Nucl. Part. Sci. **33**, 105 (1983).

[28] R.B. Wiringa, V. Fiks and A. Fabrocini, Phys. Rev. C **38**, 1010 (1988).

[29] A. Akmal and V.R. Pandharipande, Phys. Rev. C **56**, 2261 (1997).

[30] M.K. Banerjee and John A. Tjon, Phys. Rev. C **58**, 2120 (1998).

[31] B. Friedman and V.R. Pandharipande, Nucl. Phys. A **361**, 502 (1981).

[32] R.B. Wiringa, V.G.J. Stoks, and R. Schiavilla, Phys. Rev. C **51**, 38 (1995).

[33] D. Vautherin and N. Vinh, Nucl. Phys. A **422**, 144 (1984).

[34] H. Jaqaman, A.Z. Mekjian, and L. Zamick, Phys. Rev. C **27**, 2782 (1983).

[35] R.K. Su, S.D. Yang, and T.T.S. Kuo, Phys. Rev. C **35**, 1539 (1987).

[36] R.K. Su and F.M. Lin, Phys. Rev. C **39**, 2438 (1989).

[37] S.D. Yang and T.T.S. Kuo, Nucl. Phys. A **467**, 461 (1987).

[38] T.T.S. Kuo, S. Ray, J. Shamanna, and R.K. Su, Int. J. Mod. Phys. E **5**, 303 (1996).

[39] X. Campi and H. Krivine, Nucl. Phys. A **620**, 46 (1997).

[40] J. Pan and S. Das Gupta, Phys. Lett. B **344**, 29 (1995).

[41] J. Pan and S. Das Gupta, Phys. Rev. C **51**, 1384 (1995).

[42] J. Pan and S. Das Gupta, Phys. Rev. C **53**, 1319 (1996).

[43] J. Pan and S. Das Gupta, Phys. Rev. C **57**, 1839 (1998).

[44] C.W. Johnson, S.E. Koonin, G.H. Lang, and W.E. Ormand, Phys. Rev. Lett. **69**, 3157 (1992).

[45] G.H. Lang, C.W. Johnson, S.E. Koonin, and W.E. Ormand, Phys. Rev. C **48**, 1518 (1993).

[46] W.E. Ormand, D.J. Dean, C.W. Johnson, and S.E. Koonin, Phys. Rev. C **49**, 1422 (1994).

[47] Y. Alhassid, D.J. Dean, S.E. Koonin, G.H. Lang, and W.E. Ormand, Phys. Rev. Lett. **72**, 613 (1994).

[48] S.E. Koonin, D.J. Dean, and K. Langanke, Phys. Rep. **278**, 1 (1997).

[49] H.F. Trotter, Proc. Am. Math. Soc **10**, 545 (1959).

[50] M. Suzuki, Commun. Math. Phys. **51**, 183 (1976).

[51] J. Hubbard, Phys. Lett. **3**, 77 (1959).

[52] R.D. Stratonovitch, Dokl. Akad. Nauk. SSSR **115**, 1907 (1957).

[53] E.Y Loh, Jr. and J.E. Gubernatis, in *Electronic Phase Transitions*, edited by W. Hanke and Yu.V. Kopaev, Elsevier Science Publishers B.V., New York, 1992.

[54] S.E. Koonin and D.C. Meredith, *Computational Physics*, Addison-Wesley Publishing Company, Reading, 1990.

[55] S.R. White, D.J. Scalapino, R.L. Sugar, E.Y. Loh, J.E. Gubernatis, and R.T. Scalettar, Phys. Rev. B **40**, 506 (1989).

[56] H.-M. Müller and R. Seki, in *Nuclear Physics with Effective Field Theory*, edited by R. Seki, U. van Kolck, and M.J. Savage, World Scientific Publishing Co. Pte. Ltd., Singapore, 1998.

[57] E. Osnes and D. Strottman, Phys. Lett. **166B**, 5 (1986).

[58] B.D. Serot, S.E. Koonin, and J.W. Negele, Phys. Rev. C **28**, 1679 (1983).

[59] J.H. Samson, Int. J. Mod. Phys. C **6**, 427 (1995).

[60] P. Ring and P. Schuck, *The Nuclear Many-Body Problem*, Springer-Verlag, Heidelberg, 1980, p 4.

[61] N. Rom, D.M. Charutz, and D. Neuhauser, Chem. Phys. Lett. **270**, 382 (1997).